Small punch test for the assessment of hydrogen-damaged and thermally-aged steels for pressurized equipment.

Di Persio, Franco

How to cite:

Di Persio, Franco (2004) *Small punch test for the assessment of hydrogen-damaged and thermally-aged steels for pressurized equipment..* thesis, Swansea University.
http://cronfa.swan.ac.uk/Record/cronfa42630

“Small Punch Test for the Assessment of Hydrogen-damaged and Thermally-aged Steels for Pressurized Equipment”

PhD, 2004, University of Wales Swansea

F. Di Persio

ProQuest LLC.
789 East Eisenhower Parkway
P.O. Box 1346
Ann Arbor, MI 48106 – 1346

Summary

The purpose of this project was to assess the reliability of the SP (Small Punch) testing method as an alternative mechanical test technique for evaluation of the residual life and integrity assessment of components in ageing plants.

The SP testing technique was applied to the low alloy - 2¼Cr 1Mo V modified ferritic steel widely selected for construction of high temperature components in petrochemical plants. The main two test facilities employed during this project were a SP creep testing rig and a SP tensile rig. These equipments assured good accuracy and repeatability of results.

As a key component of the development of the test methodology, a new analytical stress-strain model was based on measurements taken on SP specimens from interrupted tests looking at the different phases of the sample deformation. Its implementation offered an important tool for converting the load normally employed in a SP test to the equivalent state of stress and strain, which defines the material behaviour.

This proposed stress-strain model was successfully validated, comparing the SP creep results with the conventional uniaxial creep outcome for the as-received material. Thereafter, such a model was used to assess the potential and the sensitivity of the SP technique for evaluating the degree of damage in the aged material, with special emphasis on hydrogen-aged material.

The results illustrate that when combined with an appropriate model the SP creep testing technique was shown to be an appropriate tool for integrity assessment of in-service plant components.

Declaration

This work has not previously been accepted in substance for any degree and is not being concurrently submitted in candidature for any degree.

Signed ..

Date 24/05/04..............................

Statement 1

This thesis is the result of my own investigations, except where otherwise stated.

Other sources are acknowledged by footnotes giving explicit references. A Bibliography is appended.

Signed ....

Date 24/05/04..............................

Statement 2

I hereby give consent for my thesis, if accepted, to be available for photocopying and for inter-library loan, and for the title and summary to be made available to outside organisations.

Signed ...

Date 24/05/04..............................

A mia Mamma.

Acknowledgements

The author would like to thank Prof. R. Hurst for his decisive, concise supervision throughout the work programme and Prof. B. Wilshire for help in the final stages of preparing the thesis. He would like also to thank Dr. G. Stratford for his support, guidance and enthusiasm. A thank you also goes to H. Rantala and C. Filiou for their support at the early stages of the thesis.

The experimental work in this thesis required much technical excellence and innovation. For that, the author wishes to thank Freek Harskamp, for his various technical skills, enthusiasm and contagious laughing. Many thanks also to Rene van der Aat for help with conventional creep testing and Rob Smit for welding and lifting anything too heavy for a mere mortal. A big thank you also to Antonio Saturnio for his continuous help.

A big thank you should also be offered to the metallographic team who were always helpful and prompt to their work; namely, Peter Frampton for the good quality of his patient job in the preparation of "impossible" small discs, Elsa Conceiçao for the SEM and Pietro Moretto for his support.

Finally, for making the stay in Holland more enjoyable, the author wishes to thank Maite for her lovely presence, Paolo Castello, Giustino Manna, Cecile Wojnecki, Wilko Verbakel, Lois Brett, Ioannis Vougiouklakis, and everyone else within the social circle.

Nomenclature

t_0: initial thickness of the SP disc.

t_ϕ: minimum thickness of the SP disc through the test

Boundary contact: point where the puncher touches the SP disc.

ϕ: angle to the point of the minimum thickness.

ϕ_c : angle to the point of the boundary contact.

R : radius of the puncher.

L : applied load on the SP disc.

σ: component of the equibiaxial tension stress.

f: friction coefficient due to the contact between the puncher and the SP disc.

critical area: portion of the SP disc which is failing at the end of the test

cup volume : volume of material contained within the two position of the minimum thickness.

r, θ, z : orthogonal coordinates system for the bending model.

ϕ *(meridian)*, q *(circumferential)*, *r(radial)* : spherical coordinates system for the membrane-stretching model.

CONTENTS 1

1. Introduction

The purpose of this project is to assess the suitability of the Small Punch (SP) technique as a low intrusive method for residual life assessment of in service industrial components. The project framework and the project background are here presented.

1.1. Project framework.

The present project is linked with the European Network EPERC (European Pressure Equipment Research Council, Project Leader Prof. R.C. Hurst), and in particular with the section most directly concerned with Integrity Assessment during Operation. This is related with Technical Task Force 5 (TTF5: Technical Task Force 5: Integrity Assessment during Operation). Part of the task is a Round Robin exercise for "Miniaturized Test Techniques by the Small Punch (SP) Method". JRC/IE (Joint Research Centre - Institute for Energy, Netherlands) is both the Operating Agent of the EPERC Network and a partner in R&D activities in the field of pressure equipment. The project is entirely developed with the technical support of the Clean Energies Unit of JRC/IE. The present project falls under the scientific supervision of Prof. R.C. Hurst, and it is also performed in collaboration with the TTF7 (Technical Task Force 7: Hydrogen damage) of EPERC.

1.2. Project Background

The life time assessment and potential for possible failure of in service components is a critical issue in the safety and reliability analysis of industrial plant. At the present time, many operating power stations and petrochemical plants are approaching the end of their design life. Over thirty years since those plants were built, several degradation processes have potentially reduced the mechanical properties of their structural components. At the time of construction, the design life was firstly based on empirical assumptions and on experience, and finally corrected by a suitable safety factor. Most likely, especially in the light of the major advancement in materials knowledge and available technologies, today it would be possible to reduce the safety factor and thus extend this design life. In addition, the new policies for environmental protection and the safety regulations for industrial plants make it more practical and economically convenient to extend the lifetime of existing components beyond their original design life rather than to build new plants. However, major investment to modernise existing plants is only profitable if the plant under consideration has sufficient residual life. Hence, reducing the uncertainty in the estimation and monitoring of remaining life of plant components is of fundamental importance to industry.

Due to the lack of knowledge about the residual mechanical properties in the component, the use of nominal properties are also not very accurate. In addition component integrity is rarely evaluated with traditional and well standardised mechanical test techniques, because there is not enough material to sample non-invasively from the component. Also, the most typical NDE (non-destructive evaluation) methodologies, in spite of their substantial success, rarely give a direct correlation between the level of damage and the residual life of the component. For this reason, the need to evaluate the residual mechanical properties of structural components by direct testing methods has led to the development of innovative testing methods as alternatives to the conventional ones. Several of those methods are based on miniaturized specimens, amongst which a special version, called the Small Punch (SP) technique, has emerged as a promising candidate. First introduced in the USA and Japan, in recent years, it has become known also in Europe. The SP testing can be considered as essentially a non-destructive technique because of the very limited amount of material to be sampled. Specimens are usually discs 0.3-1 mm thick and 5-10 mm diameter. It is a fast and cheap technique and has the potential to enable measurement of the realistic material properties for the specific component, identifying the present state of damage and focusing on the more critical (more stressed, more damaged) locations in the component. The method is not yet standardized and is currently under study in a number of laboratories and common Codes of Practice are under development. However, in spite of the promising perspective, technical limitations still exist for the SP technology.

The aim of this project is to design the SP technique in view of its application for integrity assessment of in-service plant components. The major applications will be evaluating the residual life in massive steel components of plants normally operating at high temperature. These include pressure vessels and pipes typical of the petrochemical industry and bodies of rotors in both aero- and land-based gas turbines. Eventually, a very small area of the component can be evaluated, such as the HAZ (heat affected zone) of a weld. The SP technique can also be useful for residual life assessment of thin parts of superalloy components, such as gas turbine blades or for analysing the strength of coatings with enough resolution to distinguish between the bonding layer and the interdiffusion region.

In this project, a material currently employed in the petrochemical industry for high temperature applications was deliberately aged, in a hydrogen environment, and subsequently tested in SP testing equipment both under creep conditions and in tensile mode at room temperature. The viability of the SP technique for determining the degree of damage of materials is then assessed with the help of an analytical stress-strain model, which is proposed by the author and validated comparing the SP results with those from conventional tests.

2. Literature review

The literature review presented in this chapter has been written to provide a broad background into the subject relevant to the work in this thesis, namely the exploitation of the SP testing technique for the assessment of the integrity of plant components. First, the industrial need will be analysed, especially considering plants operating at high temperature. Then, the SP technique will be presented as a promising candidate tool among several NDE methodologies. Next will follow a basic overview of the mechanical properties usually involved in the SP method, which will give the basis for outlining the current state of art about the SP technique.

2.1. Industrial needs for integrity assessment methods.

Fracture in engineering structures has been estimated to account for a 4% loss to the European GDP (FITNET proposal, 2001). Prevention of such failures therefore equates to a potential saving of money but as well reduces the threat to human life and to the environment. The European Commission together with industries, SMES, research centres and universities are involved in European projects such as SINTAP (Structural Integrity Assessment Procedure) and FITNET (European Fitness for Service Networks) in order to develop a unified European code for component design and plant integrity assessment. Integrating those tools for plant integrity and life extension assessment within maintenance management has the potential to optimise the industrial performance. The improved monitoring and inspection regime, will indeed allow utilities to predict with more reliability the life for components, equipments and structures. Therefore, the costs will decrease and the safety will increase, eliminating eventual production interruptions and reducing the risk of fatal accidents as a consequence of component failure. Furthermore, the design life of a component can be safely extended, avoiding premature component removal and replacement. This project focuses on the need of plants operating at high temperature.

The industry sectors most directly involved in high temperature processes are the aeronautical industries, power stations and petrochemical plants. Components often have to face several different problems which lead to different modes of material properties degradation, sometimes conjointly. This can include degradation processes such as creep, fatigue, corrosion, thermal embrittlement and hydrogen attack. In the current project, in order to simulate a hypothetical in service component, the material chosen for the experimental testing has been laboratory aged by exposing it both to hydrogen and air at high temperature, thus inducing in the material hydrogen damage and thermal-ageing. These two aspects of the material degradation are discussed in the following section followed by some details about the material selected.

2.1.1. H_2 damage

Hydrogen attack is distinctly different from the more commonly studied hydrogen embrittlement process. Actually, hydrogen embrittlement occurs at much lower hydrogen pressures and temperatures and it is normally induced by corrosion reactions in presence of water. Instead, hydrogen attack is a high temperature kinetic process that leads to severe degradation of carbon-steel mechanical properties. As hydrogen is produced during a wide range of existing high temperature processes, such as ammonia and methanol synthesis, petroleum refining, liquefaction and gasification of coal, the phenomenon is of significant industrial concern.

The hydrogen gas at certain temperatures and pressures can easily diffuse into steel. Then, the dissolved hydrogen reacts with the carbon, mainly carbides, to form methane (CH_4) that diffuses much more slowly than the hydrogen molecule because of its much larger size. The methane bubbles are mainly located at the grain boundaries where the chemical reactions take place more easily. They tend then to coalesce and cause a measurable change in volume of the material. The process results in the presence of microscopic bubbles along grain boundaries, surface decarburisation, and internal decarburisation of the single grain. (Figure 2-1, p. 43) The kinetics of the damage process is characterised by a logarithmic growth, which can lead to a sudden increase of damage after an incubation period. [Shewmon (1985), Bocquet (2000), Schlögl (1999)]. The extent of such hydrogen attack is strictly dependent on the temperature, pressure of hydrogen and time of exposure and, of course, on the composition and structure of the exposed steel. Moreover, the hydrogen attack can have different consequences on different material mechanical properties. The most severely affected are the creep properties, especially if the material is crept during the exposure to hydrogen. Generally, a clear reduction in creep life is observed and also a reduction in creep ductility. Actually, the microscopic bubbles of methane situated at the grain boundaries are characterized by a very large pressure, which are dependent on the various phases present in the steel and on the external hydrogen pressure. The methane pressure enhances the creep process, favouring the link-up and growth of cavities and thus reduces the creep properties of the material. The tensile strength properties at room temperature (ultimate tensile strength and yield stress) are less affected unless very heavy hydrogen attack is encountered. In fact, these mechanical properties are more related to the characteristics of the bulk of grain, which are less affected by hydrogen attack unless the damaging process is so heavy as to lead at evident microstructural change inside the grain.

2.1.2. Thermal-ageing

When a material is just exposed, stress free, at a relatively high temperature for a certain time, its mechanical properties can suffer certain degradation. The effect of the thermal-ageing is of course strictly dependent on the type of material which is exposed. For the typical material normally employed in the petrochemical industry, such as low alloy steel, the deterioration in mechanical properties is due to the precipitation and coarsening of some secondary phases. The strength required for these low alloy steels is normally obtained by adding some relatively small amount of elements such as Cr, Mo, V, Nb and so on, which are then forced by a proper manufacturing process to be combined as fine and well distributed carbides. When such steel is thermally-aged, there is a precipitation and coarsening of secondary phases (Laves phase) mainly at the grain boundaries, which is unfortunately the most favourable location for such processes (Byeon [2003], Okomura [1999], Singh [1997]). Several mechanical properties are consequently affected. At room temperature, the ultimate tensile strength is normally decreasing and also there is a softening of the material. Under creep conditions, the thermally-aged material generally shows a reduction of creep life and also a reduction of the creep ductility. In fact, because most of the precipitates are at the boundaries of grains, the high temperature and the applied stresses enhance the nucleation and the growth of voids and then of cracks at such locations. As a consequence, the aged material under creep conditions tends to fail before the as-received material and also the ductility is reduced with such carbides at the grain boundaries reducing the capacity of the material to deform.

2.1.3. The low alloy steel: 2¼ Cr 1 Mo, V modified.

This low alloy steel was developed specifically for the petroleum industry for high temperature, high-pressure hydrogen service with resistance to hydrogen attack. The alloy is referred to as 22V or F22V, in ASTM Standards A182, A336, A541, A542, and A 832. Probably the most high-energy equipment in a petroleum refinery are the hydrodesulfurizing units [Landau (1997)]. In their pressure vessels, the hydrogen may approach 200 atmosphere (21 MPa) at temperatures, which are at the threshold of the creep range for the ordinary chromium-molybdenum steels (454°C). The new vanadium modified steels answered to the need of advanced processes, which may push the operating temperature up to 482°C. In fact, the presence of vanadium forms more stable carbides that are more resistant to reaction with hydrogen. A detailed description of this alloy, its resistance to hydrogen attack and its characteristics are reported in the following references: [Chen (1994); Lundin (1994); Cocke (1993); Prager (1992); Bocquet (2000)].

2.2. *Options for life extension assessment techniques*

Although there are several non-destructive test techniques which are capable of giving rough, indirect information about the level of degradation of the material properties (Baldev 1997), the actual standards for integrity and remanent life analysis are limited because of the lack of realistic mechanical properties of the components in their current state of damage. In the last two decades, the need to evaluate the residual mechanical properties of structural material components by direct testing methods has led towards three types of techniques. The first technique consists of mechanical tests on specimens of standard size (i.e. not miniaturised), in which however only a small region of such a specimen is prepared with the actual material under study, while the rest, non-important parts (out of gauge lengths, threaded connections etc...) are made of another, unessential material. This is the so-called "reconstructed specimen technique" [Walle (2001)], using laser, electron beam, normal TIG welding, etc. The second method is based on the micro-indentation technique [Giannakopoulos (1999)], where the main mechanical properties are extrapolated with the help of some models that link the deformation of the metal with its elastic and plastic behaviour. The third technique considers direct measurement of the material mechanical properties by miniaturized specimen. In recent years, the approaches based on "reconstructed specimen technique" were progressively abandoned, due to a variety of problems such as difficult joining for some materials, weakness of joining, residual stresses after welding, impossibility of applying post weld treatments, cost of the electron beam process and others. The micro-indentation techniques are limited to the properties of the surface of the material. On the other hand, the technology of miniaturized specimen has gained credibility because of the potential advantage of directly measuring the material properties. Several miniaturized test techniques were proposed. Some of them were just an attempt to reduce as much as possible the dimension of the conventional specimen, such as the mini-tensile or mini-Charpy specimens. Some others also try to introduce some change in the testpiece shape, e.g. the tensile test using very thin sheet laminae. However, the required amount of material was still too much, usually making it impossible to machine the samples directly from the component in a non-destructive way. The need for further miniaturization led some researchers to develop a special technique, called the Small Punch test. The specimen this time is a small disc 5 to 10 mm in diameter and 0.3 to 1 mm thick punched on one side, being supported by a ring on the other side. This technique was introduced firstly in USA and Japan (Manaham, 1981; Mao, 1987), aiming at integrity assessment of irradiated materials by looking at toughness properties at low temperatures. In recent years, it arrived in Europe and the research was extended to include evaluation of residual creep life.

The small punch testing has the advantage to be an easy and cheap technique, and the results obtained so far are encouraging. The very limited amounts of material to be sampled make the small punch technique an almost non-destructive test. Hence, it has the potential to exploit directly the realistic mechanical properties for the specific component, identifying the present state of damage and focusing on the more critical, more stressed and more damaged locations in the component. The method is not yet standardized and it is currently under study in a number of laboratories, with common Codes of Practice under development.

However, in spite of the promising perspective, technical limitations still exist for the SP technology. For instance, it is still unclear how the state of stress evolves within the SP specimen during the test and especially which value and state of stress finally brings the specimen to failure. Actually, the stress which could lead to failure of the material is the more important parameter required for the integrity assessment of in service plant components. Furthermore, the small sizes of the specimens could exaggerate the local effects of inclusions or the effects of surface phenomena or of the grain size. This gives rise to a lack of understanding as to how the results could depend on the test variables. Within this project, it is the intention of the author to remove such uncertainties and to develop the SP technique using both the creep and the tensile toughness SP testing, which have been the two most used applications of the SP technique. Therefore, before reviewing the state of art for the SP it is useful at this stage to introduce some general concepts about creep and tensile properties of metals.

2.3. An introduction to general creep

When metals operate at temperature in excess of 0.3 T_m, where T_m is the melting temperature (in degrees Kelvin), the application of stress may cause time dependent plastic deformation, referred to as creep. It is also found that the time during which the material can sustain the stress is finite and that failure comes at a given rupture time. In general, this failure happens as consequence both of thinning induced by large strain and as the result of growth of damage in the metal. In order to evaluate creep properties of metals, several standard creep test procedures have been developed. These techniques, for the most part, concentrate on the uniaxial stress condition in which the loading is applied parallel to the longitudinal axis of a cylindrical or plate specimen. Although uniaxial creep tests have led to a good understanding of the physical processes involved, they often do not provide sufficient information to predict the behaviour of high temperature industrial components. Load bearings parts at elevated temperature are often subjected to multiaxial loading conditions that drive the deformation and rupture mechanisms in a manner that is different from simple uniaxial loading.

2.3.1. Steady state creep

The basic record of a generic creep test is a plot of creep strain, ε, versus time as illustrated schematically in Figure 2-2 [p. 44]. No general agreement has been reached on the form of the equation, which should be used to describe the creep curve shapes observed at high temperature. For this reason, in the high temperature regime, the creep curves are commonly described by references to the creep rate. Thus, after the initial strain on loading, the creep rate usually decays during the "primary stage" until it reaches a constant value, characterizing the "secondary stage". This is generally followed by a "tertiary stage" where the creep rate increases again up to the failure.

Thus, we can express the creep rate as:

Eq. 2-1

$$\dot{\varepsilon} = f(\sigma, T, t) \quad \text{or,} \qquad \dot{\varepsilon} = f(\sigma, T, \varepsilon)$$

where $\dot{\varepsilon}$ is the creep rate dε/dt, σ is the stress, T the temperature, t the time and ε the strain. During the "secondary stage", the creep rate is only a function of temperature and stress. This value, $\dot{\varepsilon}_s = f(\sigma, T)$, called "secondary" or "Steady-State" creep rate, then assumes great significance because it allows the creep properties of a material to be described by a relatively simple equation which can be verified by experimental data.

2.3.1.1. Temperature dependence of the secondary creep rate

Creep tests carried out at the same level of stress but at different relatively high temperatures show a significant characteristic. The secondary creep rate $\dot{\varepsilon}_s$ increases rapidly with increasing test temperature, suggesting that some process involving thermal activation controls the creep rate. Thus, obeying the Arrhenius Law, it is possible to write:

Eq. 2-2
$$\dot{\varepsilon}_s\Big|_{\sigma=\mathrm{const}} = f\left(e^{-\frac{Q_c}{RT}}\right)$$

where Q_c is the activation energy for the thermal activated process, and R the Gas constant (8.314 $\mathrm{Jmol^{-1}K^{-1}}$). The value of Q_c can be calculated from the experimental data. It is also possible to observe that increasing the value of stress causes an increase in the initial strain and the subsequent strain rate. But the calculated value of Q_c does not change. So the activation energy for the creep process appears to be insensitive to differences in stress. Thus

Eq. 2-3
$$\dot{\varepsilon}_s(\sigma, T) = f(\sigma) \cdot e^{-\frac{Q_c}{RT}}$$

The analysis described above is invalid when applied to thermally unstable systems, such as precipitation-hardened alloys [Dorn (1954)] where two or more thermally activated phenomenon may occur. Within these limits of validity, however, Q_c appears to be a structure sensitive property and, especially for pure metals at temperature well above 0.4 T_f, it is frequently observed that $Q_c \approx Q_{sd}$ (activation energy for self-diffusion) [Sherby (1967)]. At lower temperatures, the value of Q_c drops around a transition point and decreases to approximately $Qc \approx 0.5\ Q_{sd}$ [Feltham (1959)].

2.3.1.2. Stress dependence of the secondary creep rate

Carrying out creep tests at different stresses at the same temperature often leads to a good straight-line relationship when $\log(\dot{\varepsilon}_s)$ is plotted versus log σ. This suggests the existence of the relationship, normally called Norton's Law,

Eq. 2-4

$$\dot{\varepsilon}_s \propto \sigma^n$$

The stress exponent, n, is normally found for a wide variety of pure metals to be around 4 – 6 for relatively high values of stress. However, at lower stresses, the coefficient n decreases towards a value of around 1.

2.3.1.3. Power Law representation and creep deformation

Thus, the equation Eq. 2-3 can be now be coupled with Eq. 2-4, which give:

Eq. 2-5

$$\dot{\varepsilon}_s = A\sigma^n \cdot e^{-\frac{Q_c}{RT}}$$

This so-called power law relationship describes very well the steady state creep behaviour and specific values of n and Q_c are associated with specific creep mechanisms. The creep deformation can be explained as the result of combination of two distinct mechanisms, which are acting sequentially and independently from each other. The first is the diffusion-controlled generation and movement of dislocations [Weertman (1957), Mc-Lean (1966)], which is typical of high stress and low temperature creep test [$n = 4 - 6$, $Q_c \approx 0.5 \cdot Q_{sd}$]. The second is the stress directed vacancy flow without dislocation movements [Nabarro (1948), Herring (1950), Coble (1963)], which is instead typical of high temperature and low stress creep test [$n = 1$, $Q_c \approx Q_{sd}$]. Thus, in every creep test, the temperature and the stress acting on the sample and indeed the test material are the factors, which determine the creep deformation process.

2.3.2. Internal stress

Another interesting phenomenon happens when the stress changes during the creep test. The creep rate then changes as well but sometimes in an unexpected way. For instance, depending on the amount of the stress reduction, the creep rate can be inverted. The cause is an internal stress σ_i, which is opposing continued dislocation movement. Thus, the creep deformation does not take place under the full applied stress σ, but under an effective stress σ_{eff} such that

Eq. 2-6

$$\sigma_{eff} = \sigma - \sigma_i$$

Any creep theory based on the generation and movement of dislocation must then be able to account for this often observed mechanism.

2.3.3. Creep fracture

When the creep test enters into the tertiary creep stage, the failure of the testpiece is often imminent. The rupture lives commonly obtained from uniaxial creep tests are then recorded and, by extrapolation, can be used for high temperature industrial component design to give the required rupture life under service condition. The information described above represents a minimum requirement because, in most operational plant, the material is subject to multiaxial states of stress. Actually, the creep damage develops depending on the material and on the stress state acting on the component. Monkman and Grant (1956) found a linear relationship between the minimum strain rate and the time of failure, which shows that the rate of damage development must be related to the deformation rate.

Cane (1981) considered creep failure as a consequence of three sequential processes. The first stage is the production of cavity nuclei, which is followed by the formation and growth of stable cavities that produces discrete cracks. Finally, comes the third stage with linkage between cracks leading to the final fracture propagation. He was accounting each of these processes in the context of a multiaxial state of stress. He conducted uniaxial creep test in cylindrical bars, tension creep test thin walled tubular specimen to simulate the biaxial state of stress and finally creep tests on notched cylindrical bars in order to get a triaxial state of stress. He considered as key stress values the principal axial stress σ_1, the average stress also known as the octahedral normal stress

Eq. 2-7
$$\sigma_H = \sigma_{oct} = (\sigma_1 + \sigma_2 + \sigma_3)/3$$

and the von Mises stress defined as the effective stress $\bar{\sigma}$,:

Eq. 2-8
$$\bar{\sigma} = \frac{3}{\sqrt{2}} \cdot \tau_{oct} = \frac{1}{\sqrt{2}} \cdot \left[(\sigma_1 - \sigma_2)^2 + (\sigma_2 - \sigma_3)^2 + (\sigma_3 - \sigma_1)^2\right]^{1/2}$$

Where τ_{oct} is the octahedral shear stress on the 8 planes, which have an inclination of 54°45' with the principal axis. The materials chosen for the analysis were 2¼Cr1Mo and ½CrMoV. After a detailed fractography investigation, he concluded that the slowest stage, therefore the one that is controlling the whole failure process, is the formation and growth of stable cavities that produces discrete cracks. He claimed that this key process depends on both the effective stress $\bar{\sigma}$ and on the principal stress σ_1, with σ_1 predominating at low $\bar{\sigma}$.

Hayhurst (1983) extended this work. He considered a biaxial state of stress in relation to data taken from the work of Johnson (1962). He introduced the isochronous loci plot for showing the rupture data within different biaxial states of stress. The rupture lifetime he used was that of a uniaxial test carried out at the normalising stress σ_0.

Hayhurst worked on aluminium and copper and the results showed that the criterion of rupture depends on the material and that it is linked to a certain proportion of the effective stress and of the principal tension stress. For instance, in copper, the criterion for the rupture time is based mainly on the maximum tension stress, (the straight line on the plot in Figure 2-3 [p.44]) while, for the aluminium, the criterion is more linked with the maximum effective stress (the elliptic curve on the same plot). This assertion was supported by a detailed metallography investigation, which showed how the creep damage in the single material followed the same trend whatever state of stress was applied. The copper and aluminium behaviour define two extreme ways of fracture, with others materials performing in-between them. For instance, stainless steel 316 was also tested under multiaxial conditions and the rupture criterion was found approximately to be based on the maximum tension stress law in the second quadrant, which refers to a positive biaxial state of stress while, in the other quadrants, the behaviour followed the maximum effective stress law.(Figure 2-4, p. 45).

2.4. A general introduction on tensile properties of metals.

The tensile test is a testing technique for determining yield strength, tensile strength and ductility of a material. The conventional tensile test is the uniaxial test, where the most classical output is the stress/strain diagram. This plot can be referred to the "true" values of stress or as the defined "engineering" stress depending whether a constant cross section of the cylindrical specimen all along the test, or the real one (based on a reducing cross section area) is used in the calculation. The two curves start to differ only in the plastic field. Consider the "true" diagram, on such a plot can be detailed the elastic properties of the material by its elastic modulus (Young Modulus: slope of the linear part), the yield strength as the stress-strain at the point where the stress/strain plot departs from linearity, and the ultimate tensile strength which defines the point where the material reaches plastic instability, and necking occurs somewhere along the cylindrical specimen. The shape of such a curve can be then related to the constitutive or hardening law of the material $\sigma=f(\varepsilon)$ which describe its plastic behaviour. However, much greater difficulties are encountered when all this information has to be translated for a multiaxial state of stress. Then, different criteria for describing the behaviour of the material during the test can be outlined in general. Thus, a yield criterion is defined for describing the plastic deformation and the hardening law, while later the plastic instability, with the emergence of the necking and finally the failure of the material, is described by a ductile fracture criterion. The most famous yield criteria are the von Mises, and the Hill criteria (Hill, 1948), but several others were proposed later (Gotoh, 1977; Hill, 1979; Logan, 1980), while Brozzo, (1972) undertaken an exhaustive description of the most important ductile fracture criteria. The most typical application of such a criteria is mainly related to the sheet metal forming processes. For this purpose, the conclusion of some works (Lin, 1985; Toshihiko, 1998;) shows that the proposed yield criteria can estimate quite well the behaviour of the metal sheet, at least under a biaxial stress state. However, the application of the ductile fracture criteria presents much more difficulties (Heung, 2003). In fact, the accumulation of damage in the material, which introduce the plastic instability and later leads to the failure, is not only dependent on the magnitude and direction of deformation, but also on the whole history of the stress state throughout the multiaxial test. In particular, an important role seems to be played by the hydrostatic component of the stress state (Bridgman, 1952).

2.5. The Small Punch test technique

2.5.1. Historical background of the SP technique

The Small Punch test technique was developed in the early '80s, starting from USA and Japan, in order to study the degradation of the mechanical properties of metals and alloys due to neutron irradiation. The limited space available for testing in nuclear reactors and the narrow damage zone produced by charged particle accelerators pushed the researchers to find a miniaturized test capable of extracting post-irradiation mechanical behaviour information. Their first thought was TEM (Transmission Electron Microscopy) disc samples (usually ∅ 3mm and thickness = 0.25 mm), which historically were employed to track the changes in microstructure due to neutron irradiation. Samples were centrally loaded and deflection curves were recorded in order to generate the stress/strain response. Results have been compared with data coming from classical test methods, leading to empirical relations. Also, some efforts have been made to evaluate the data by analytical expressions derived from the theory of bending of large plates [Timoshenko (1957), Chakrabarty (1970)] and adapting knowledge coming from the metal forming industry [Herbert (1910), Stelson (1981)]. Since then, the miniaturized disc bend test has been developed much further, extended in Europe, and not only for nuclear applications. Several small specimen techniques have been investigated, changing the geometry of the specimen and holders, as well as the shape of the puncher. Specimen discs with square or circular shape, with a range of thickness between 0.25 and 0.5 mm, have been tested. Ball and shear [Lucas (1984)] punch have been compared, concluding that only the ball punch method can provide a wide array of mechanical properties, such as strength, ductility, elastic modulus, ductile-to-brittle transition temperature and fracture toughness. Monotonic load-displacement records are used to derive tensile properties of materials [Huangh (1982), Manaham (1981), Manaham (1986), Dooley (1981), Okada (1988), Cheon (1996), Byun (2001)]. Furthermore, from tests at several temperatures, Fracture Appearance Transition Temperatures (FATT) and fracture toughness parameters are achieved [Baik (1987), Mao (1987), Eck (1997), Cheon (2000), Jia (2003)]. An attempt to measure Young Modulus using miniaturised disc bend tests has been also made [Hoffmann (1995)]. A more detailed investigation of the miniaturized disc bend test, using FEM analysis and new images interferometry techniques, has been carried out within a European Commission project involving the Universities of Limerick (Eire) and Liverpool (UK) [Brookfield et al. (1999)]. Since the late '90s, the SP technique started to be implemented in creep lifetime assessment. The SP tests at elevated temperature, in inert environments, enable creep rates and rupture strengths to be measured. Earliest results on this subject have been achieved by [Parker (1995), Parker (1998)] in Swansea University (Wales-UK). This pioneer work has been taken as a base for further research in Europe [Tettamenti (1998), Dobes (2001), Maile et al. (1998)], and in Japan and China.[Komazay (2000), Yang (2003)]. However, technical limitations still exist for the SP technology. The small sizes of the specimens, especially at low temperature, could exaggerate the local effects of inclusions or the effects of surface phenomena or grain size.

2.5.2. Interpretation of the SP results

The interpretation of the SP results followed two routes. One, which was more analytical, tried to model the strain and the stress state within the SP specimen, taking as a basis the works from Chackrabarty (1970) and Timoshenko (1957). The other way attempts to define some empirical and phenomenological rules that, in the view of the authors, would correlate the response of SP tests directly with the results from conventional tests. This second method greatly simplified the interpretation of the SP results, but unfortunately it does not give any exhaustive answer to the real condition of the material because it does not consider the way the SP sample is deforming. Here follows a table (Table 2-1), which summarizes the main published works so far on the SP technique, listing the approach employed for analysing the results on the given material.

AUTHOR	SUBJECT	MODEL	MATERIAL	AGEING
Manaham (1986)	Tensile properties; Deformation analysis; Sampling technique.	No model.	SS 316 with 20 % cold work	No ageing
Baik (1986)	Fracture mechanics; Deformation analysis.	No model.	Ni-Cr steels	doped with P and Sn and thermal-ageing
Mao (1987)	Fracture mechanics; Interrupted tests.	Strain model; Relation fracture toughness-fracture strain.	Several steels: PCA, 316, HT-60, HT-9, 9CR, A533B, A508, SUS304	No ageing
Hoffman (1995)	Elastic deformation analysis.	Elastic model.	Al_2O_3, and hot pressed NiAl	No ageing
Cheon (1996)	Yield stress estimation.	Elastic model.	ASME SA 508, and 12 Cr rotor steel	No ageing
Cheon (2000)	Fracture mechanics.	No model.	CF8 Duplex stainless steel	Low temperature thermal-ageing
Byun (2001)	Tensile properties; Deformation analysis; Sampling technique.	Stress-Strain model	Stainless steel AISI 316 LN; Ferritic/martensitic 9Cr-2WVTa	No ageing
Jia (2003)	Fracture mechanics.	No model.	Martensitic/ferritic steels: F82H, T91, Optimax A	Irradiation ageing

AUTHOR	SUBJECT	MODEL	MATERIAL	AGEING
Parker (1998)	High temperature creep.	Empirical stress relationship.	1CrMoV rotor steel	Creep ageing
Tettamenti (1998)	High temperature creep.	Empirical stress relationship.	In service steel ASTM A355 P12	No ageing
Maile et al. (1998) COPERNICUS	High temperature creep.	Empirical stress relationship.	German type steels 14 MoV 6 3 X 20 CoMoV 12 1	No ageing
Komazai (2000)	High temperature creep; Interrupted tests.	Strain model. Empirical stress relationship.	Tungsten-alloyed 9% Cr ferritic steels	Thermal-ageing
Dobes (2001)	High temperature creep.	Stress-Strain model	14MoV63	In service component (creep ageing)
Yang (2003)	High temperature creep.	Stress-Strain model	12Cr1MoV	No ageing
Di Persio (2004)	High temperature creep.	Stress-Strain model	2¼Cr 1Mo V modif.	Hydrogen induced damage

Table 2-1: Record of the main references on SP testing technique.

2.5.2.1. *The origin of the stress-strain models*

The works of Chakrabarty (1970) and Timoshenko (1957) were developed in the context of the theory of large plate bending. They form a good starting point for modelling the strain and the stress state within the SP specimen. Originally made to contribute to the metal forming industry, these models can be adapted to the SP case, although there are some weak points. For instance, the sizes of the elements involved are substantially different. In the metal forming industry, the metal plates are usually so thin and broad that they can be considered as 2-dimensional while, in the SP specimen, the thickness cannot be neglected. Thus, in these models, the necking process is not very well considered and only a general thickness reduction rule linked with the invariability of volume during plastic deformation is presented. Despite their limitations, these models have the advantage of introducing the important concept of the membrane-stretching deformation mode. Defining the three principal directions within the SP specimen as the meridian, circumferential and radial directions, the models define a state of balanced biaxial tension where the two stresses, meridian (σ_ϕ) and circumferential (σ_θ), are the same ($\sigma_\theta = \sigma_\phi$) and are indicated as responsible for the membrane-stretching and designated as the stress σ. (Figure 2-5, p. 45) Developing this concept, the model produces an important relationship linking the punch load L with this stress σ. This relationship is a function of the puncher radius R, the angle defining the contact region ϕ_c and the actual thickness t.

Eq. 2-9

$$\frac{L}{\sigma} = 2\pi R \cdot t \cdot \sin^2 \phi_c$$

The strain model is also built on the three main directions within the SP specimen. The meridian and the circumferential strain have to be the same ($\varepsilon_\phi = \varepsilon_\theta$) in membrane-stretching deformation mode, and their addition gives the radial strain, because of the incompressible plastic deformation.

Eq. 2-10
$$\varepsilon_\phi + \varepsilon_\theta = -\varepsilon_r = -\varepsilon$$

The radial strain is then directly linked with the thickness reduction and is given in the general form of:

Eq. 2-11
$$\varepsilon_r = \ln\left(\frac{t_0}{t}\right)$$

where t_o is the initial thickness.

The deformed plate can be separated into two regions: the supported surface or contact region that assume the hemispherical shape of the puncher, and the unsupported region defined by a catenoid surface. By simply geometrical consideration, it is possible to define then a relationship linking the vertical displacement d with the extension of the contact region defined by the contact angle ϕ_c:

Eq. 2-12
$$\frac{d}{R} = 1 - \cos\phi_c + \sin^2\phi_c \cdot \ln\frac{\tan(\phi_c/2)}{\tan(\theta/2)}$$

where:

Eq. 2-13
$$\sin\theta = \frac{R}{a} \cdot \sin^2\phi_c$$

Where (a) is the radius of the receiving aperture.

2.5.2.2. Development of the strain model

Mao (1987) applied successfully the strain model in order to analyse the fracture toughness of metals. He worked on the elastic-plastic properties of metals at room temperature, and demonstrated the suitability of the SP technique for assessing the fracture properties of metals. Based on the Bayoumi (1983) theory, he linked the strain at fracture of SP specimen directly with the fracture toughness J_{IC}. The thickness reduction was evaluated and directly measured on interrupted tests and directly linked with the strain. The author defined an equivalent strain, considering Eq. 2-10 and Eq. 2-11 [p.32] where:

Eq. 2-14 $$\bar{\varepsilon}_q = \sqrt{2/3} \cdot \left(\varepsilon_\phi^2 + \varepsilon_\theta^2 + \varepsilon_r^2\right)^{1/2} = \ln\left(\frac{t_0}{t}\right)$$

Furthermore, in these interrupted tests, the extension of the contact area was also measured via its radius *c*. ($c = R \sin \phi_c$)

These values were plotted versus the central deflection, showing the two different mode of plastic deformation acting during the SP test (Figure 2-6, p. 46). First is active the bending mode, where the contact radius is controlled by bending deformation. Then, when the curve reduces its gradient the membrane-stretching mode is starting and the contact radius is controlled by the thickness reduction. Byun (2001) followed the same course in considering the strain evolution in the SP specimen. However, he entered more into analysing the deformation process, and he considered very important the contribution of the puncher indentation at the equivalent strain, especially in the first bending phase. The same conclusion was reached in a more recent Japanese paper

[Komazai (2000)] working under the high temperature creep conditions. They interrupted some SP creep test on which the extension of the contact area and the thickness reduction were measured. Here, it was evident that the SP specimen was mainly deforming by the membrane-stretching deformation mode both at room temperature and at high temperature, with the deformation controlled by the thickness reduction. For this purpose, several authors tried to demonstrate that the central deflection in the SP specimen can be directly linked to the strain whatever test temperature, load, time and material were chosen. Then, the vertical deflection in the SP technique will be just like the elongation is in the standard uniaxial specimen. Mao (1987) plotted the calculated strain versus the central deflection and he found that all the points follow the same trend along different steels tested on SP samples of different size (Figure 2-7, p. 46).

This trend can be then described by the following equation:

Eq. 2-15

$$t/t_o = \exp\left[-\beta\left(d/t_o\right)^2\right]$$

Where the constant β was determined by experiment.

A more recent work from Yang (2003) goes in the same direction. Yang was running high temperature creep tests. In this case, the value of strain came from a finite element analysis, but the relation between the modelled strain and the thickness reduction was not clear. The results showed that the relationship between the central deflection and the creep strain for the SP specimen was approximately independent of test temperature, load, time and material.

2.5.2.3. Development of the stress model

The definition of the stress model is the more complex problem, although the membrane-stretching mode has been accepted as the basis for a valid model. Yang (2003) used the Chakrabarty (1970) model presented above, while Dobes (2001) developed a complex stress model introducing the Robinson life fraction rule (Robinson 1938). Baik (1986) adopted the biaxial state of stress typical of the membrane-stretching in order to explain the fracture behaviour in the SP specimen. The aim was to assess the availability of the SP technique for evaluating the intergranular embrittlement by ductile-brittle transition temperature measurements. For this purpose, several SP tests were run at different deflection rates and at different temperatures, from room temperature down to –195° C and the fracture energies were calculated. These values were then compared with the fracture energies coming from uniaxial tensile tests and Charpy tests. The divergences observed in the fracture behaviour among the three different techniques were explained in terms of the different stress states active in the respective specimens. Baik found that the brittle fracture in the SP specimen was controlled by the propagation stage of cracks, because of the high stress gradient observed within the SP specimen. He demonstrated also that the earlier stages of crack evolution, such as the nucleation and initiation of cracks, were much easier in the SP specimen because of the biaxial state of stress.

Manahan (1986) worked with a finite element model in order to get the equivalent power law relationship for the SP toughness tests, such as that in the uniaxial tensile test. He analysed the SP toughness curve, establishing different regions depending on which deformation mode was active. Byun (2001) was also focusing on the deformation process in SP tensile test. Assuming the power law relationship for the material (from the uniaxial tensile tests), he reported the stress evolution at both side of the SP specimen. He compared then the SP state of multiaxiality with the typical stress state present in the necking of a conventional cylindrical uniaxial specimen during a tensile test and concluded that they were similar.

2.5.2.4. Phenomenological approach

In some work, the SP results are treated without the aid of any stress or strain model. These authors looked at the phenomenological aspect of the SP test and tried to translate the SP results in a form that would be directly comparable with the results coming from the conventional tests. Parker (1998) concentrated his attention on the time of failure for high temperature SP creep tests. He observed that the overall shape of the creep curves obtained from the SP tests was qualitatively similar to those obtained from conventional uniaxial creep tests, which clearly delineate a secondary and tertiary creep stages. In addition, also a minimum deflection rate could be identified and correlated by a Monkman-Grant relationship [Monkman (1956)] with the creep life. Thus, as with the uniaxial creep test, the life t_f was then directly correlated with the experimental load (instead of stress) and temperature using an equation of the Dorn (Arrhenius) type [Dorn (1954)].

Eq. 2-16

$$\frac{1}{t_f} = B \cdot (\mathrm{Load})^m \cdot \exp\left(-\frac{Q_c}{RT}\right)$$

Where B is a constant and m is the load exponent of failure life. Parker observed that the values of m and Q_c were similar to the stress exponent and the activation energy for self-diffusion calculated for the equivalent (similar time of failure) uniaxial creep tests. This was a demonstration that the mechanism of creep and the rate determining creep damage process were the same in both techniques. Thus, the same materials tested at the same temperature that behave microstructurally in the same way are expected to fail at the same value of stress. Then, his conclusive statement is that the SP technique exhibits similar stress characteristics to results produced by standard uniaxial methods. Comparing the two Dorn type equations for the SP creep test and the uniaxial creep test, at the same temperature and with the same time of failure, the result is a load/stress ratio. It was then suggested that this ratio would give the value of the critical stress needed for the evaluation of damage and the residual life of in-service components. However, this approach shows a weak point because the load/stress ratio is empirically obtained from the original batch of material. Actually, the SP specimen taken from the in-service components represent a very local situation and its mechanical properties are probably significantly different from the original batch. Thus, although this approach makes the analysis of SP creep results simple and practical,unfortunately this load/stress ratio is capable of giving only a rough estimation of the critical stress. The same approach was adopted by K. Maile et al. (1998) in the COPERNICUS project.

2.5.2.5. Fracture analysis

Some authors tried to give an explanation for the typical annular fracture observed in the SP tests. In the range of temperatures from above the DBTT (Ductile Brittle Transition Temperature) of the SP toughness test, up to the highest temperatures in SP creep tests, the fracture occurs always on an annular region at the bottom of the SP specimen. [Bulloch (1994)].

2.5.3. The experimental set-up of the SP test

As an additional element of uncertainty, the SP technique is still missing a real Code of Practice. Consequently, there is no agreement on the size and shape of specimen, puncher, and receiving hole. Furthermore, in some works, the specimen is clamped while in others it is not (Figure 2-8, p. 47). To demonstrate these differences, it is useful to compare the different SP technique configuration employed so far in other works in the table below. Table 2-2

TITLE	SPECIMEN SHAPE AND SIZE (mm)	PUNCHER RADIUS: R (mm)	Ø RECEIVING HOLE: a (mm)	SP TECH.	NOTE
Baik (1986)	Square: 10x10; t =0,5	1,2	4	Tensile	Clamped spec.
Manaham (1986)	Disc: Ø =3; t =0,25	0,508 – 0,762	No defined	Tensile	No clamping
Mao (1987)	Square: 10x10; t =0,5	1,2	4	Tensile	Clamped spec.
Hoffman (1995)	Disc: Ø =3; t =0,2 – 0,6	Loading ring (Ø =0,453 mm)	2,132	Tensile	No camping
Cheon (1996)	Square: 10x10; t =0,5-0,25	1,2	4	Tensile	Clamped spec.
Cheon (2000)	Square: 10x10; t =0,5	1,2	4	Tensile	Clamped spec.
Byun (2001)	Square: 1,5x7,5; t =0,25	0,5	1,6	Tensile	Clamped spec.
Jia (2003)	Disc: Ø =3; t =0,25	1	1,5	Tensile	Clamped spec.
Tettamenti (1998)	Disc: Ø =8; t =0,5	1,25	4	Creep	With argon; Clamped spec.
Maile et al. (1998)	Disc: Ø =8; t =0,5	1,25	4	Creep	With argon; Clamped spec.
Parker (1998)	Disc: Ø =9; t =0,5	1,00	4	Creep	With argon; Clamped spec.
Komazai (2000)	Square: 10x10; t =0,5	1,2	4	Creep	With argon; Clamped spec.
Dobes (2001)	Disc: Ø =8; t =0,5	1,25	4	Creep	With argon; Clamped spec.
Yang (2003)	Disc: Ø =10; t =0,5	1,2	5	Creep	With argon; Clamped spec.
Di Persio (2004)	Disc: Ø =8; t =0,5	1,0	4	Creep	With argon; Clamped spec.

Table 2-2: Different SP experimental set up in literature.

2.6. Conclusions of Literature Review

Many power and petrochemical plants are currently approaching, or are already operating beyond, their design life. These industries are then strongly interested in developing and using a reliable method for residual lifetime assessment in order to justify their maintenance costs. The SP technique seems to be the best option in the range of the proposed methods, because it can be considered an almost non-destructive technique, requiring a small amount of material, and is easy and inexpensive.

The SP technique has been investigated by several authors around the world and, beyond the promising results, there is no doubt that much work remains to be done. The main objective of this research is to assess the suitability of the SP technique as a tool for residual life assessment, capable of measuring the mechanical properties of materials in comparison with the conventional test methods, such as the uniaxial tensile test and uniaxial creep test. The very small size of the SP specimen is the main advantage compared with the conventional tests but, unfortunately, understanding of results is more difficult. The early works were mostly concerned with determination of the toughness material properties in a range of low temperatures. For this purpose, several different kinds of material degradation were considered, such as irradiation ageing, thermal embrittlement and doping. Later on, the creep properties started to be the object of investigation, looking mainly at the potential of the SP technique for revealing the effects of creep and thermal-ageing. However, none of these works considered hydrogen damaged material, which is an original contribution of this current project.

Some papers proposed empirical relationships in an attempt to correlate the response of SP tests directly with the results from conventional tests, including the works of Komazai (2000), Parker (1998), and Tettamenti (1998) for high temperature creep and the work of Baik (1986) for fracture mechanics properties. For instance, Parker (1998) analysed the SP creep test without any complex stress and strain models. He directly correlated the life with the experimental load and temperature by virtue of an equation of the Dorn (Arrhenius) type. This makes the analysis of SP creep results simple and practical, but unsuitable for seriously quantifying the remaining creep life fraction of in-service components. Actually, the failure time in SP creep tests, especially for damaged material, is not the only important parameter. The way in which the SP specimen is deforming and the thickness is reducing in the necking area is more critical and meaningful. Other papers introduced models that help the interpretation of the SP results in terms of stress and strain. The definition of the stress state within the SP specimen appears to be the more complex problem, although the membrane-stretching mode has been accepted as a basis for a valid model. Yang (2003) and Dobes (2001) present a simplified solution taken from the works of Chakrabarty (1970) and Timoshenko (1957) and adapted for the SP creep testing technique. However, in both cases, the SP-load/Uniaxial-stress ratio found by the authors was lacked of physical meaning. Komazai (2000) and Mao (1987) present the more complete strain model for the high temperature SP creep and for the SP tensile test. Also in this case, the models come from the work of Chakrabarty. The thickness reduction was evaluated and directly measured on interrupted tests and directly linked with the strain. Furthermore, Mao

(1987) together with Yang (2003), introduced a simplified finite element model for the strain, finding an unequivocal relationship between the calculated strain and the measured central deflection. Finally, a detailed stress-strain analysis of the SP tensile test was made by Byun (2001), which tried to correlate the deformation regime with the stress and strain state within the SP specimen.

As an additional cause of uncertainty, the SP technique is still missing an accepted Code of Practice. Although the general features for the SP test equipment are generally accepted, such as the hemispherical shape of the puncher and the need of a clamping system, authors uses their own specimen and apparatus designs.

2.7. Figures – literature review

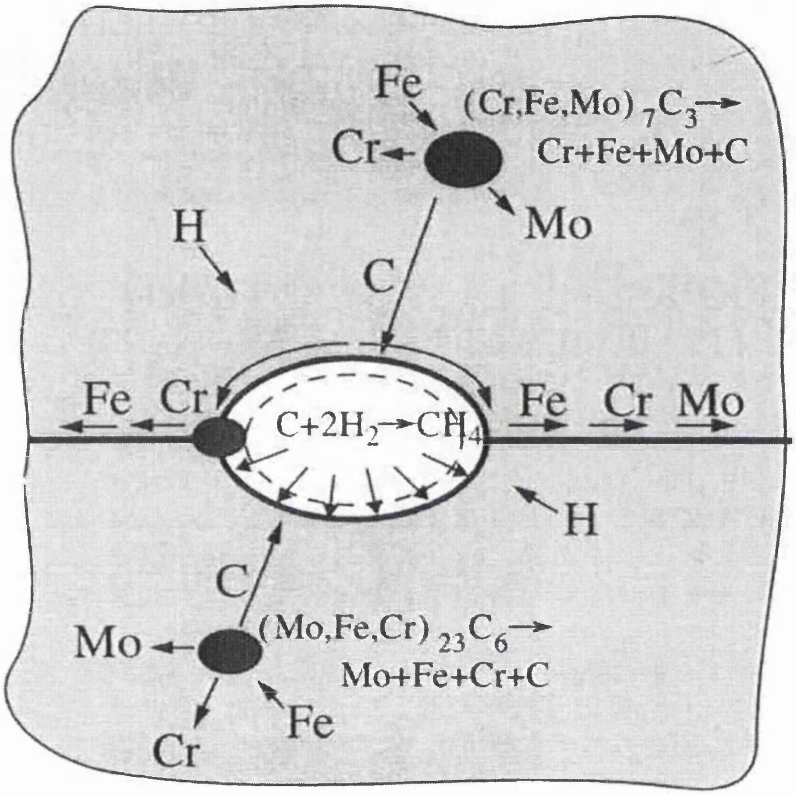

Figure 2-1: Sketch of the processes involved in the hydrogen attack of a low alloy steel. [Schlögl (1999)]

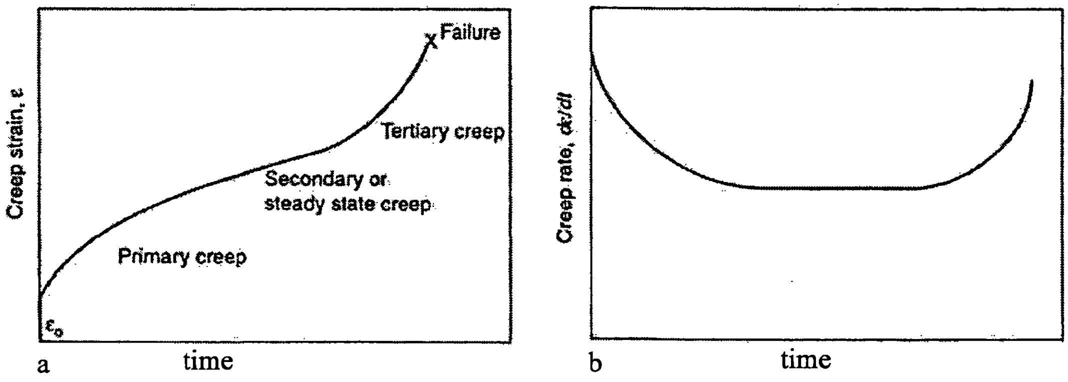

Figure 2-2: Schematic illustration of the dependence of a) creep strain and b) creep rate on time [Gibeling (2000)].

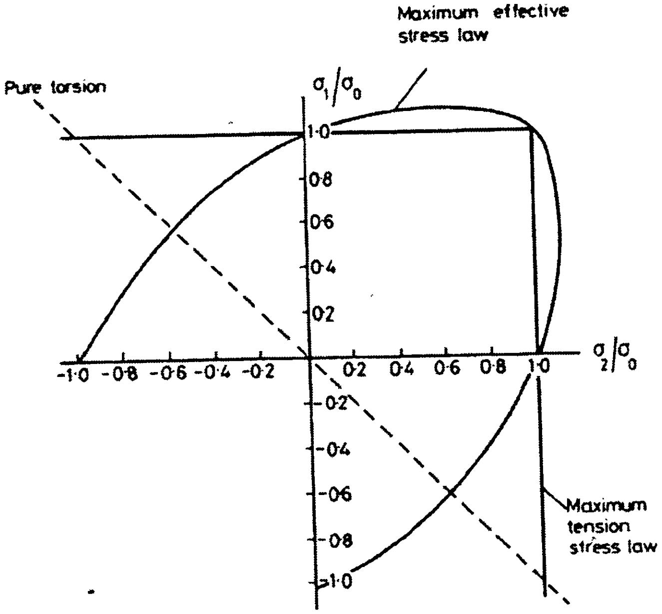

Figure 2-3: Isochronous loci plot. [Hayhurst (1983)]

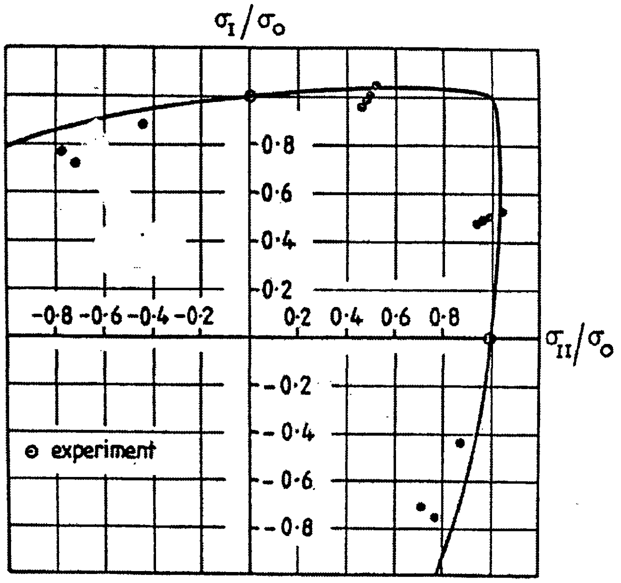

Figure 2-4: Isochronous loci plot for stainless steel 316. [Hayhurst (1983)]

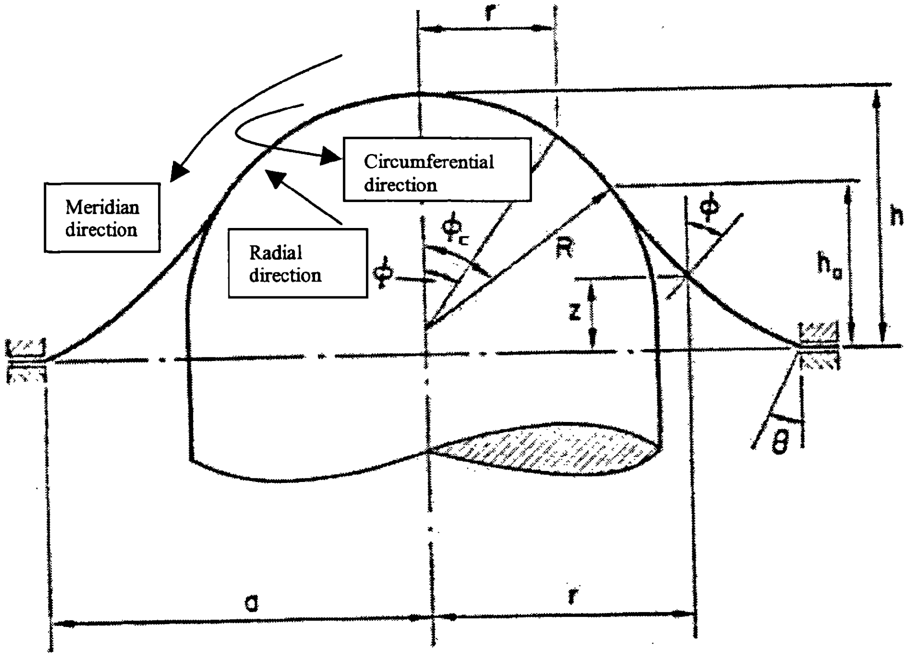

Figure 2-5: Sketch adopted by Chakrabarty (1970) for his analysis.

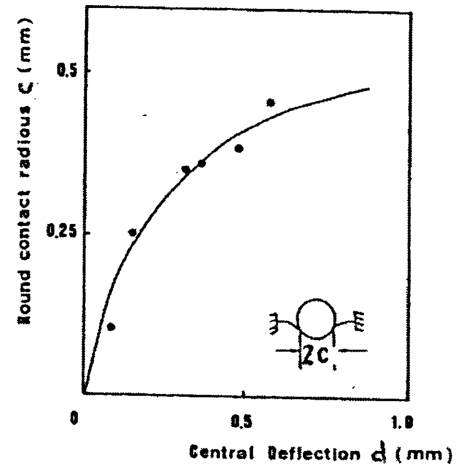

Figure 2-6: Mao (1987) – Contact Radius Vs. Central deflection. (HT-60 specimen)

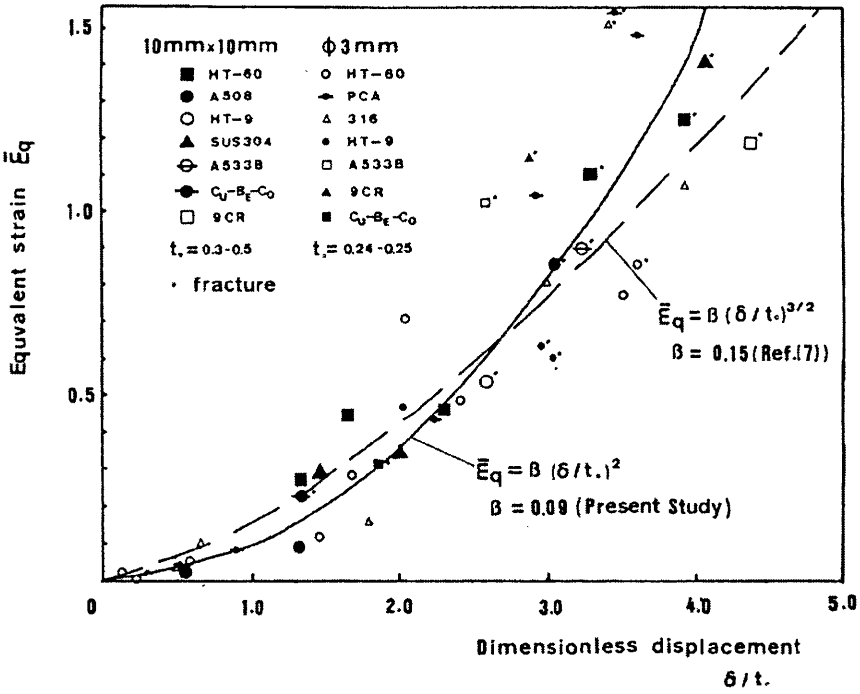

Figure 2-7: Mao (1987) – Strain Vs. Vertical displacement (δ=d).

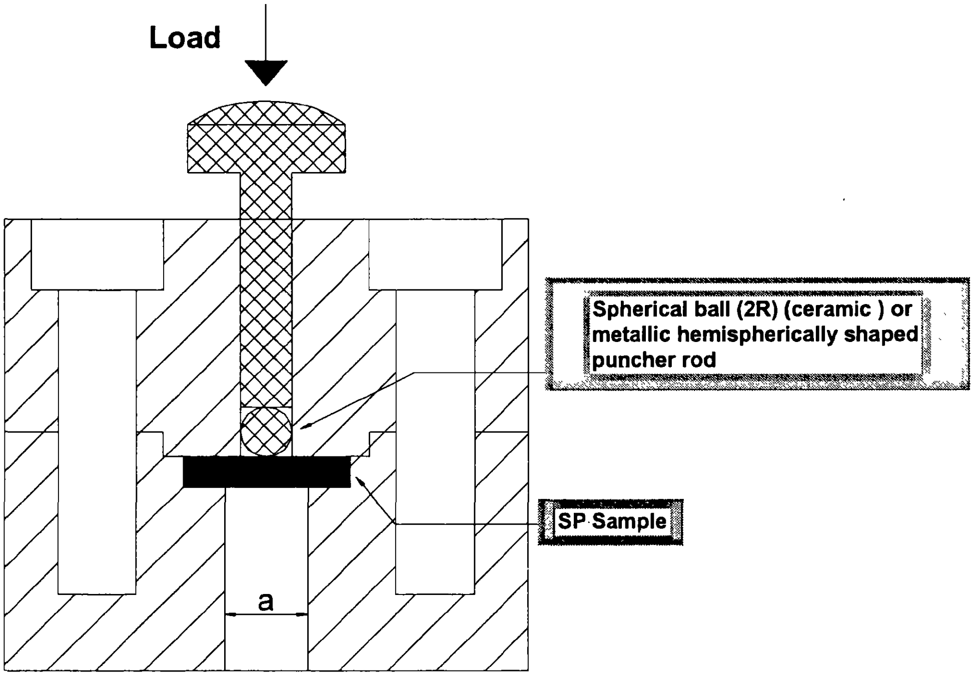

Figure 2-8: Schematic of a SP configuration with clamping system

3. Aim of Programme

The programme was designed to evaluate the reliability of the SP testing method as an alternative mechanical test technique for evaluation of the residual life and integrity assessment of components in ageing plants. The considerable economical and environmental gains derived from plant life extension are of major importance for plant operators and for the EU economy.

As a key component of the development of the test methodology, a new analytical stress-strain model will be based on measurements taken on SP specimens from interrupted tests. Its implementation will offer an important tool for converting the load normally employed in a SP test to the equivalent state of stress and strain, which defines the material behaviour.

The SP testing technique will be applied to the low alloy - 2¼Cr 1Mo V modified ferritic steel widely selected for construction of high temperature components in petrochemical plants. The technique will be shown to facilitate determination of both creep and tensile properties of materials. However, special attention will be directed to the potential of the SP creep testing technique for assessing the deterioration of material due to hydrogen attack and thermal-ageing, in comparison with conventional uniaxial creep methods.

It is intended that this present work will contribute towards improving the acceptability of the SP test for industrial application.

4. Experimental Procedures

The main two test facilities employed during this project were a SP creep testing rig and a SP tensile rig. The SP creep equipment was designed originally by the University in Wales Swansea (UK) and adapted and modified during the current project. The SP tensile test rig was completely designed by the author of this current project according to a technique developed by Dr. Whelan of the JRC in Ispra (IT). In this chapter the experimental procedure adopted, in order to assure the accuracy and the repeatability of results, will be detailed.

4.1. SP Creep facilities

4.1.1. The equipment as received from Swansea University.

The SP equipment, which is working at constant load, has been developed in the University of Swansea under the direction of Prof. Parker and Dr. G. Stratford. The author made the training on this equipment by participating to a round robin exercise, which involved three others laboratories, including Swansea University. The Small Punch testing set-up is illustrate schematically in Figure 4-1 (pag. 75). The main elements defining the essence of the rig are the:

- The small specimen. A disc of 8 mm diameter and 0,5 mm thick.
- The clamping system, which avoids any sliding of the sample during the test.
- The hemispherical puncher by which the load was applied to the sample.

- The furnace, which made it possible to run tests at relatively high temperatures (up to 650° C).
- The gas sealing system, which kept the sample in a controlled atmosphere.
- The measuring devices, which were two LVDT's and one thermocouple and a data acquisition system, recording the output signals.

The sample and the procedure for its preparation will be described in detail elsewhere in 4.8 where the material chosen for this project will be illustrated. The puncher was constructed from a creep resistant Nimonic alloy and machined by CNC (Computer Numerically Controlled) technology to have a perfectly hemispherical tip. The hemispherical tip of the punch has a diameter of $\varnothing$ d1 = 2 mm and it was pushed against the specimen by a constant force. The SP specimen with an initial thickness of $t_o = 0.5$ mm was located in a recess on a stainless steel die and clamped around the edges by a stainless steel upper die, which works also as a guide for the puncher. Because of the absence of any sign of sliding on the SP disc at the end of the test, the clamping force was presumed to be high enough to avoid any sliding. A circular hole of $\varnothing$ d2 = 4 mm was located in the die below the specimen, into which the sample would bulge under the action of the punch at the specified load. The geometries respect the empirical relation: $[d2 \geq d1 + 2 \cdot t_o]$ to avoid the friction of the disc with the inner wall of the lower die [Mao (1987)].

To maintain the sample at the desired temperature, the whole of the die/specimen/punch arrangement was enclosed in a cylindrical furnace. The furnace was based on a resistance heating system and controlled by the Eurotherm® 2132 temperature controller. Based on the input of a thermocouple mounted next to the wall of the furnace a solid state relay closes or opens the circuit following the need of heating or cooling for keeping the temperature of the sample within ± 1°C. The standard deviation expressing the temperature stability normally obtained during a 500 h test was around 0,2° C In the two opposite side of the furnace a cooling system worked by circulating cold water to maintain the temperature of those two cold points at temperature below 50°C in order to prevent damage to the rubber 'o' rings, which seal the gas system.

Type N thermocouples were used to measure the temperature. The temperature of the sample was taken from a thermocouple placed on the upper die close to the sample because it was impossible, during the test, to fix the thermocouple directly on the sample. The tip of the thermocouple was placed in a small hole and in order to avoid any uncontrolled displacement during the test some steel wire was employed to secure it. There exists a gradient of temperature within the clamping system, which determines a difference of temperature between the sample and the place where the thermocouple was positioned. Such gradient make the temperature of the sample generally lower then the temperature at the measuring point. This difference was not constant and needed to be calibrated at different temperatures, as detailed later in the calibration section.

All tests were performed in a protective atmosphere of argon with an industrial purity (argon 4.6). A valve regulates the flux of argon at 0.3 Lt/min. Such a flow was verified not to influence at all the temperature field around the sample. Before the tests start a visual inspection was made in order to discover eventual leak of gas from the equipment. The gas should be evacuated only from the valve fixed in the bottom part of the equipment to assure the sample was not in contact with an appreciable quantity of oxygen. To avoid leaking of argon from the connection between the mobile puncher and the fixed part of the equipment a rubber bellow was employed. During the preliminary phase and within the round robin exercise a single test (128 hrs) was run without argon in order to assess the influence of oxidation on results, but the time of failure obtained was comparable with the other tests made in Ar. So the argon protection does not apparently influence the results at least for tests lasting up to around 100 hrs and at the temperature of 605°C.

The central deflection was measured by two LVDT extensometers type AG 1.0 manufactured by Solartron®. The data was triggered by the transmitter Solartron® OD2. The range of operability was of 2 mm and the deviation from linearity is shown in the paragraph dedicated to the calibration procedure. One of these LVDT (Bottom LVDT) was directly taking measurements from the displacement of a ceramic (quartz: Al_2O_3) rod applied on the lower surface of the disc. The rod was ceramic to assure the absence of any appreciable false reading due to thermal expansion. The contact between the rod and the lower surface of the sample was assured by a small spring. Furthermore, the contact has to be flat as much as possible in order to assure the reading refers only to the central bulge of the sample. The second LVDT (Top LVDT) was taking measurements by an aluminium rod (far away from the hottest point of the equipment) attached to the puncher and it was reading the distance moved by the puncher at the point where the rod was attached. The heat coming from the furnace can influence the measurement of the

Top LVDT. To limit this effect a heat sink was positioned on the puncher below the rod connected to the LVDT. However the displacement measured by the Top LVDT was not reliable because this reading was influenced by the deformation of the puncher. In fact, because of the more reliability for the measurement coming from the Bottom LVDT all the results were given referring to this LVDT. The Top LVDT was thus employed just as controller and back-up extensometer.

4.1.2. Upgrade of the equipment.

The equipment so far has been described as was delivered to the JRC from the Swansea University at the beginning of the project. Later some upgrades were carried out mainly concerning the data acquisition system and the loading system.

In order to automate the data acquisition system and make easier the recording, the author has developed a LabView® software for managing the data by a FieldPoint® National Instrument hardware. As a result the measurements were continuously recorded in ASCII files on a PC. A friendly interface was create in order to set up the test parameters such as the rate at which to record the data. Actually, the system was capable to record displacements and temperature at any desired interval of time and for any event the user wished to consider. In general any variation of temperature greater than 0.5°C and any displacement greater than 10 μm was recorded. The software was also capable to trigger the recorded data with a specific event such as the switching off of the furnace and so on.

Another important upgrade that was implemented during the testing programme was the loading system. A hydraulic piston working with compressed air was added in order to allow the instantaneous loading and to guarantee then the reproducibility. In the first tests carried out within the Round Robin exercise the load was applied manually with a rate that was obviously not very constant. For instance, in charging 300 N the first 200 N came within the first 10-20 sec while the rest followed in the next 10-20 sec. Instead, the hydraulic device that was adopted guaranteed the complete loading within only one second. The only circumstance to pay attention to was that during the loading the puncher had to be slightly raised for some seconds, and the small temperature variation (anyway less then ±2°C) induced in the sample lasted just few minutes, and cannot be considered crucial. Furthermore this hydraulic system became very useful when the need to interrupt tests was required during the later phases of the project.

4.1.3. Suggestion for further improvement

Definitely the main change the author suggests is to substitute the fixed hemispherical puncher with a single use spherical ceramic ball. The reason is for assuring the uniformity of shape and dimension of the puncher ball for each test. As detailed in the chapter regarding the stress-strain model the radius and the shape of the puncher were crucial factors in defining the state of stress and strain in the SP sample. For running this project two SP creep equipments were employed. One device was used for almost two years, to which should be added one year for the previous period before being set up in the JRC laboratories, while the second was new. Although the state of the puncher was analyzed optically at the beginning and at the end of the project without evidencing any appreciable change, the limits of such a procedure does not exclude alteration of the puncher state.

4.1.4. Calibration Procedure

The whole process involves measurement of load, temperature, and displacement.. Among these the temperature was the more important because of the crucial role it plays in the creep phenomena. Several factors affect the measurement of these quantities. For instance an uncertainty of 5 K could mean uncertainty in the time of failure and thus was not acceptable for standard creep test methods (ASTM E 139, BS 3500, DIN 51226, ISO 204, ISO 7500_part2). Calibration procedure and test techniques were performed and established in order to reduce the bounds of those uncertainties.

4.1.4.1. Temperature

In the SP equipment thermocouples of type N were used. Under the current conditions they can be considered reliable with a degree of uncertainty of ± 0,5 °C. Each of them were calibrated by a reference furnace. Such a furnace was provided from ISOTECH® with a certification which shows a declared uncertainty of ± 0,5 °C in the range of temperature from 200° to 650° C. In this reference furnace narrow deep cavities hold the thermocouples to be calibrated together with the reference thermocouple. As a result of the calibration, for each thermocouple a correction factor was obtained which was applicable in the range of temperature where the calibration was carried out. In fact, the considered range was between 550 °C and 600 °C, the range where the thermocouples were working. Then the correction factor so calculated was expected to provide a value of temperature, which was reliable within the limit of precision of the type N thermocouple.

Another factor affecting the uncertainty of the temperature value was the stability of the furnace in the SP equipment. From the reading obtained during the tests it appeared that the furnace was stable and the variation of the measured temperature of the sample was kept in the range of ± 0,5 °C.

There was another aspect to take in consideration. During the test it was impossible to fix a thermocouple directly on the sample, thus its real temperature was derived from the measurement taken by a thermocouple positioned in the upper die. The difference between the two temperatures was assumed to be the same if the boundary conditions and the geometry configuration of the equipment do not change for each test. That difference (temperature sample lower than the upper die temperature) was most likely due to the design of the clamping system that resulted in a quite strong dispersion of heat through the bottom die, by mainly conduction and radiation. The convection due to the Ar flow does not change the thermal behaviour of the system, at least up to the limit value of 0.5 L/min (measured at the entrance to the system). It became essential to calibrate the system in order to assess that difference. The equipment was set up and the only change with respect to the ordinary configuration was that the ceramic rod was substituted by a thermocouple spot-welded directly on the bottom surface of a SP sample. Thus it was reasonable to assume that in the two configurations the thermal behaviour was equivalent. The spot-welded thermocouple was also calibrated by the reference furnace and as usual with an expected precision of ± 1 °C. The system was heated up and the standard thermocouple in the upper die was correlated with the spot-weld thermocouple in order to obtain the correction factor as function of the temperature (Figure 4-2, p. 76). Once the correction was known the real temperature of the sample was calculated subtracting such difference from the reading of the thermocouple. Experience suggests that the systematic error affecting such a process of deriving the temperature of the sample from a reading in different location, can be also kept within ± 1 °C. Hence, it was possible to consider the final uncertainty of the temperature value given as the root of the sum of the square of the single uncertainty, with a final uncertainty of ± 1,6 °C. Such uncertainty was however within the acceptable range for conventional creep tests. (ASTM E 139, BS 3500, DIN 51226, ISO 204, ISO 7500_part2).

4.1.4.2. Load

The load was fixed for a given thickness of the sample. The nominal thickness was fixed at $t_N = 500$ µm. In the circumstances that the disc thickness was different, to assure an equivalent level of stress in the sample an empirical relation between the load and the real thickness t_R of the disc has been given [Maile (1998)]: (look at the load-stress relationship from the stress model)

Eq. 4-1

$$L_R = L_N \cdot {}^{t_R}\!/_{t_N}$$

In any case in order to reduce the uncertainty coming from this relationship only samples with average thickness of 500 ± 5 µm were admitted.

Another important point was to assure both that the load was applied perpendicular to the top surface of the sample and that the sample was perfectly parallel to the holder and die. A spirit level was employed in order to guarantee the planarity of the sample, and then a weight suspended by a thread was employed to check if the frame guiding the puncher was perpendicular to the sample.

Eccentricity of loading was not so important because the sample was securely clamped around its border and an eventual eccentricity of the load resulted just in an off-centre deformed bulge.

The employed weights were calibrated by a balance with a precision of ± 5 gr. (± 0.05 N). This was the main source of error because others factors were considered irrelevant. For instance, the error of ± 1 μm made in measuring the disc's thickness translated to an error for the load of ± 0.002 N or ± 0.2 gr. Other small mechanical factors, such as the small spring employed to keep the ceramic rod in contact with the sample and the effect of the rubber elbow were considered non-critical.

Thus, a final accuracy for the load of ± 0.05 N was assumed.

4.1.4.3. Displacement

Two LVDT's were employed in order to measure the deflection of the disc. The linearity of the transducers was assessed by inserting ceramic gauge-blocks under the measurement tip of the LVDT. The signal was a 4 to 20 mA current and the calibration was performed reading the signal twice increasing and decreasing the displacement respectively. The average value (S_a) of the two reading was then linked to the displacement (d) by the relation:

Eq. 4-2 $$d = (S_a - \text{Zero}) * \text{Gain}$$

where (Zero) was an arbitrary value and the (Gain) was fixed in order to minimize the deviation from linearity. The linearity of the transducers was evaluated comparing the result of the equation Eq. 4-2 with the real thickness of the gauge-block (*t*) by the percent of deviation:

Eq. 4-3 $$\text{dev}\% = \frac{(t-d)}{2} * 100$$

The LVDT's showed in the working range a deviation from linearity less than 0.1 %. (Figure 4-3, p. 76).

4.1.5. Test procedures

Once the sample was fixed in the equipment, before heating up the furnace, the puncher was positioned on the sample.

- The sample was positioned in the clamping dies and the thermocouple fixed at the appropriate location in the upper die.
- Once the puncher was positioned in contact with the sample and the sealing assured the argon flux was provided by an open circuit with no over-pressure.
- The puncher load defined the so called pre-load, which was less than 20 N.
- The furnace started to heat.
- Time needed to reach the test temperature: about 2 h.
- Time for temperature stabilisation before loading: preferably 4 h.
- During this time extensometer was set to zero.
- Test zero time: at the instant when full loading was started

- Time for full loading: less than 1 sec.
- Deflection measurements: digital recording by FieldPoint + LabView interface.
- Time intervals: not homogeneous, 1 measurement per each displacement of 10 microns and for each variation of temperature greater than 0.5°C.
- The output of the SP creep test was a graph where the vertical displacement was plotted versus time.

As a general rule, an excessive overriding of testing temperature during heating (5°C) was avoided. The temperature of the sample was controlled and maintained within ± 1°C.

4.1.6. Interrupted test

By using the hydraulic device subsequently adopted on the equipment, it was possible to run interrupted tests. Once the chosen time to interrupt the test was reached the hydraulic piston was activated and the load raised almost instantly. The main geometrical features to be measured on an interrupted sample were the extension of the contact area between the puncher and the sample and the thickness distribution along this area. In order to get such information the sample was first of all observed in the SEM (Scanning Electron Microscope) looking both at the front view and at the side view, and pictures were taken and next employed for measuring the bulged area (Figure 4-4, p. 77) and the diameter of the imprint left by the puncher on the sample (Figure 4-5, p. 77). These measurements were affected by an uncertainty of ± 5 μm. Next, the thickness of the sample at the tip of the bulge was measured directly with a micrometer giving an uncertainty of ± 5 μm. These errors affected the general thickness measurement all along the contact area. Assuming that the shape of the contact surface between the sample and the puncher was spherical, those data were enough to calculate the thickness distribution along the contact area. Some samples coming from interrupted test were cut at their bulge cross section and observed at the SEM for a microstructural investigation. The sample was finally represented in a sketch drawn using a CAD program (Figure 4-6, p.78). Based on this sketch, the main geometrical features, such as thickness and angles were measured. The uncertainty of such measurement can be given for the thickness with a bias of ± 5 μm, and for the angles with ± 1 ° degree.

4.2. Uniaxial creep equipment

The uniaxial creep equipment employed in this project were 20 KN constant load creep machines. The loading arms and the thermocouples were periodically calibrated and the accuracy for the applied stress evaluated as ± 1 MPa, and for temperature of ± 1° C. The displacement transducers were working in a range of 10 mm with a deviation from linearity of ± 0.5 %.

4.3. SP tensile facilities

An Instron servo-hydraulic machine was adapted with a special environmental chamber for working over a range of temperature between −160°C and 300°C. The load was applied by fixing a constant displacement rate in compression. It was applied at the top of a small rod of 2 cm length which had a hemispherical puncher of diameter 2R=2.5 mm at the opposite end. To assure the load was applied perpendicularly to the sample surface a special rolling bearing system was mounted at the head of the Instron machine. The load values were given by a load cell which worked in the range of ± 5 kN. The SP sample was clamped strongly at its edge and under the action of the load was forced to deflect in the receiving aperture of 4 mm diameter. An image acquisition system was adapted for capturing images of the lower disc surface in order to check visually the deformation and the fracture behaviour. Two LVDT's read the vertical displacement of the puncher, which was consistent with the disc deflection. The vertical displacement was then plotted versus the load.

This equipment was designed to work down to cryogenic temperatures, but most of the tests were made at room temperature looking just at the tensile properties of the material and at the specific tensile features of the SP testing technique. The work done was a good basis for further research aimed at investigating the potential of the SP testing technique for assessing the fracture toughness properties of materials (Ductile-Brittle-Transition-Temperature, etc …).

4.3.1. Calibration Procedure

The whole process involved measurement of load, displacement and temperature. Several factors affected the measurement of those quantities. Calibration procedure and test techniques were performed and established in order to reduce the magnitude of any errors.

4.3.1.1. Load

Instron provided the load cell with the capacity of 5 KN with a calibration certificate, which assured an error in the linearity of less than 0.15 % in the range from 500 N to 5500 N. At loads below 500 N the level of deviation from linearity was not given, but it was expected not to vary too much from the value previously given. It was impossible to carry out our own calibration because a special calibration rig would be needed which was unfortunately not available in the laboratories.

4.3.1.2. Displacement

The two LVDT's were applied close to the head of the puncher and they measured the displacement due to the deformation of the sample and also the contribution of the elastic deformation of the bearing elements between the point of application of the two LVDT's and the sample. In order to distinguish between these different contributions, a compliance test was made. A rigid surface was positioned in place of the sample and then a load displacement curve was recorded. This compliance curve was then subtracted, proportionally to the load, from the displacement normally recorded during the ordinary test.

The two LVDT's employed were special and could be used down to – 200 °C. The calibration was made at – 50 °C by the supplier with a certified deviation from the linearity less then 1% over the range of 10 mm. A second home based calibration was made by the author at room temperature and for a range of about 3 mm. Then, assigning the appropriate gain the deviation from linearity in the defined range was less than 0,3 %.

4.3.1.3. Temperature

The SP tensile equipment was mainly used at room temperature. Some attempts to work at temperatures below zero were made. In those cases the measurement of the sample temperature was taken by a thermocouple of type N, but unfortunately without any calibration at such low temperatures. Also the location of such a thermocouple was not in direct contact with the sample, and the eventual difference was not established. Therefore the uncertainty was relatively large and in the order of ± 5° C at -160° C.

4.3.2. Test Procedure

A list of the test procedure is given below.

- First the sample was clamped inside the holders. The clamping force had to be large enough to avoid any sliding of the sample during the test
- If the test was to be made at a temperature different from room temperature, then the thermocouple had to be fixed
- The holder was then positioned in the SP testing equipment and fixed in order to allow the endoscopes of the camera to take images of the bottom of the sample
- The puncher was also inserted and positioned in contact with the top surface of the sample and next the head of the loading was fixed above the puncher and a preloading is applied below the material elastic limit

- At this stage the two LVDT's were set to zero, taking care that they were working in the calibrated range.
- If the test had to run at different temperature than room temperature, then the heating/cooling chamber was activated.
- The deflection rate was defined and introduced by the controller of the Instron machine. Some limits for safety reasons could be also fixed.
- The tests started and the load increased with the displacement following the hardening law of the material.
- Displacement data were recorded from the two LVDT's and from the head of the Instron machine, and finally the temperature was recorded through a PC on to an ASCII file. The control of the camera and the recording of data were managed by a LabView software developed by the author of this thesis.
- The output of the SP tensile test was a plot where the load was plotted versus the displacement, which was automatically corrected by using the compliance data.

4.4. Uniaxial Tensile equipment

The same Instron equipment employed for the SP tensile tests was employed for the conventional uniaxial tensile tests and with a different load cell (100 KN). In this case the data coming from another project was used in the form of a single uniaxial test on a sample cut from the same batch of material used in this project.

4.5. Hardness measurement

The hardness measurements were made by a micro-hardness tester, which expresses the measurement as a Vickers hardness number. When the measurement was made directly on the SP specimen, the load to be applied was chosen based on a compromise. In fact the imprint left by the indenter was more easily interpreted when a greater load was used. On the other hand, the small thickness of the SP sample limited the intensity of the load. According to ASTM E 92, the diagonal of the imprint left by the pyramidal indenter has to be at least one or one and half time the whole thickness of the sample. Hence the load was chosen as 10 Kgf, which led the diagonal to be for this material around 300-320 μm, which was less then two third of the thickness (500 μm). The load was always applied for 10 seconds. The surface of the SP disc, as detailed later, was finished to 1200 grit, which was enough for the hardness measurement. Finally, the calibration and the procedures adopted assure that all the hardness numbers were given with an uncertainty of ± 2 units.

4.6. H_2 exposure equipment

Such equipment represented the most hazardous aspect of the experimental work. Extremely high precautions had to be taken when dealing with hydrogen because of its tendency to explode when in contact with oxygen. A special laboratory had the right facilities, including a small pressure vessel capable of containing H_2 gas up to a pressure of 200 bars and up to a temperature of 650° C. The distribution of temperature inside the vessel was known, and precaution was taken in order to assure that the material to be exposed was in the zone where the temperature was approximately uniform with a degree of uncertainty kept at ± 2° C. The pressure of H_2 was set at 180 bars and the temperature of exposure at 600° C. The rate at which the temperature was raised to the given value of 600° C was set at 0,5° C per minute. The same rate was adopted for the descending temperature after the furnace was switched off. The pressure was raised at a slower rate. In the calculation of the total time of exposure the contribution of such transitional fractions of time were ignored and only the time when the pressure was stabilized at 180 bars was considered. The H_2 pressure was quite stable and varying only within ± 2 bars. Later some precautions were taken in order to produce the SP samples from such exposed material as detailed in the paragraph regarding the material preparation. Two sessions of hydrogen exposure were organized. The first was extended for a time of approximately 3000 h. The second was planned to reach 6000 hrs but the vessel had to be stopped for a safety problem after only 5000 hrs.

4.7. Thermal-ageing equipment

In this case, the material was kept in a furnace in the presence of air for a given number of hours. The distribution of temperature within the furnace had an approximately vertical gradient with a relatively small region where the temperature could be considered uniform with an uncertainty of ± 2° C. In this region the material to be exposed was positioned. Only a single exposure of about 3000 hrs at the temperature of 600° C was made. The rate at which the temperature was raised to the given value of

600° C was set at 0,5° C per minutes. The same rate was adopted for the descending temperature after the furnace was switched off.

4.8. Testing Material

USINOR INDUSTEEL provided the material. It was the low alloy heat-resistant chromium-molybdenum steel: 2 ¼ Cr – 1 Mo, V modified.

According to the supplies, the composition in %was expected to be:

C = 0.10-0.15; Mn = 0.3-0.6; S < 0.01; P < 0.015; Si < 0.10; Cr = 2.00-2.50; Mo = 0.9-1.10; V = 0.25-0.35; Ni < 0.25; Cu < 0.20; [could be also some B = 0.001-0.003, some Ti = 0.015-0.035 and some Ca < 0.15]

V modified Cr-Mo steel has come into quite common use to manufacture hydroprocessing reactors in the last decade, and represents a most promising option, due both to its good hydrogen attack resistance and for economic considerations. For this project, this material was also chosenbecause of the large amount of creep data coming from the Predich Project [Bocquet (2000)], and because of the potential for collaboration with another concurrent piece of work at JRC.

The batch of material (Figure 4-8, p. 79) was sent to JRC - Petten in a block with four weldment lines. From this block, the material for the SP discs and the uniaxial creep specimens were taken out by spark erosion (Figure 4-9, p. 80). Some of the pieces were exposed to hydrogen or thermally-aged. The pieces were classified with a letter and a number, which identified the exact location of each of them. The cylinders, which were then machined to produce uniaxial specimen, were classified with the letter: U. The others pieces were classified with the letters from K, L, M, N, P and they were used for obtaining SP samples.

4.8.1. Uniaxial Specimens

Thirteen specimens for uniaxial creep tests (Type U) were cut along the X direction. Afterwards they were machined in order to obtain the cylindrical specimens as illustrated in the Figure 4-10, p. 81. Some of them were exposed later to hydrogen and some others thermally-aged .

4.8.2. Small Punch Specimens.

For the purpose of this project the use of base metal was considered sufficient. However, the possibility to extend the research suggested the preparation of some material with weldments was to be included. The samples L and M were wholly base metal while the pieces P, N and K contain weldments. All those pieces were cut to a cylindrical shape, with the only exception of the pieces type K. Some uncertainty on how the weldments should appear on the SP sample resulted in leaving the piece K with a rough shape for a further analysis. All cylinders were cut to a diameter of 9 mm. Next, some of them were exposed to hydrogen and some others were thermally-aged. Only after such an operation, all the cylinders were machined in order to reduce the diameter to 8 mm. This procedure was chosen to assure the complete absence of any effect that the aging processes could have on the surface of the cylinders and consequently on the outside perimeter of the SP discs. For example, the hydrogen exposure can lead to some decarburisation at the surface, which under the conditions prescribed for the current project, can reach a depth of 0,2-0,5 mm. The SP samples of 8 mm diameter and 500 µm thick were next produced by cutting cylinders in slices.

The slices were cut in the beginning at approximately 550 µm on a "Struers Accutom-5 cutting machine Type 356 CA Aluminium Oxide blade, 500 microns thick. The blade speed was 3000 rpm, with a continuous rotation of sample and then with feed speed of 0.010 mm/s. The resulting discs were fine ground from both sides equally. The first grind was on 800 grit SiC paper to get to approximately 525 µm, followed by final polishing on 1200 grit to reach 500 µm. In the preliminary work done during the round robin exercise (creep) some tests were made to assess the eventual influence on results of the sample preparation. For this purpose, some discs were cut at 700 µm instead of the usual 550 µm and polished down to 500 µm to assess the possible influence of an eventual hardening of the disc surface due to the grinding procedure. But, there wasn't any effect of sample preparation on the results, the failure time in creep being comparable to the conventional samples. The thickness of the discs was measured accurately by a vertical micrometer (± 1µm precision) using as base a metallic sphere. Five points (with a resolution on the disc surface of 100 µm) were taken on the disc both at the centre and at four points at 2 mm distance from the centre. An average value of thickness was used to calculate the exact load for applying on the discs.

4.8.3. Microstructure and hardness values for as received and aged material (base metal).

All the SP samples from base metal were prepared both from the cylinders of type L and M. It was noted that the SP sample coming from the type L pieces had got the same grain orientation with respect to the test tensile load, comparing with the uniaxial specimens. In order to investigate possible differences between these two opposite orientations both a metallographic analysis and hardness measurements were made. The two pictures taken with the SEM microscope (Figure 4-11, p. 82, and Figure 4-12, p. 83) showed practically no differences in the grain size and general structure with the microstructure being typical of a low carbon bainitic (acicular ferrite) steel. The hardness measurement were carried out on discs coming from both type L and M and the results were practically the same as summarised in the next table:

Vickers Hardness	HV_{10}
Type L	202, 203, 201
Type M	203, 206, 207 204, 201, 201, 202, 200, 204

Table 4-1: Vickers hardness HV_{10} for the as received material at the two orientations defined by the type L and M cylinders.

Hence, because of the larger availability of material of the type M, most of the results came from SP samples made from those cylinders.

Once some of the material was aged, the degree of damage accumulated was defined by hardness measurement. In fact the microstructure analysis was not a feasible method as the changes in the microstructure were not visible at all. In fact, the evaluation of hydrogen attack sensitivity of the materials could not be performed at the service temperature (450 to 480°C) because the processes of carbide destabilization by hydrogen needed a very long time at that temperature. It was recognised that accelerated damage may be observed after exposure for about 1000 hours at 600°C, and classification of the materials was commonly based on this type of test. It has been reported in literature that the 2 ¼ Cr – 1 Mo, V modified steel was a promising hydrogen attack resistant material [Bocquet (2000)] and the chosen level of exposure was expected to lead to not very different levels of damage with, in any case, no evident trace of cavitation in the material, even if reduction in creep life was expected. The characterization of the damage by hardness measurement is summarized in the next table:

Vickers Hardness	HV_{10}
Hydrogen damage (3000 hrs exposure)	191, 192, 191
Hydrogen damage (5000 hrs exposure)	182, 186, 186, 185, 184, 184
Thermal-ageing (3000 hrs exposure)	190, 190, 190, 188, 190, 190

Table 4-2: Vickers hardness HV_{10} for the damaged material.

The softening of the material due to the hydrogen exposure was a consequence of the decarburisation. In fact the methane bubbles had nucleated and linked-up mainly at the grain boundaries consuming carbon from carbides situated inside the grain. Then the reduction of the hardness value could be considered as an effect of the hydrogen attack.

In the same way the softening at room temperature of the thermal-aged samples also highlighted that the microstructure of the material was slight changed. Most probably the thermal exposure made possible the precipitation and coarsening of Cr, Mo and V compounds (Laves phase) at the grain boundaries. The exact composition and location of such carbides could possibly be deduced from TEM analysis.

4.8.4. SP sample from the weldments.

The Small Punch specimens with weldments were made starting from the cylinders of type N and P, or from the block type K. The cylinders type N-P are represented in the Figure 4-13, p. 84. In this case the SP specimen should be made around the most critical area, which is the heat affected zone (HAZ), leading to only one specimen from each cylinder. From the block K it was possible to cut cylinders as shown in Figure 4-14, p. 84. In this case many SP samples could be cut, but the repeatability of results has to be assessed, as this time the eccentricity of loading will be an important factor.

Actually only one SP sample was taken out from the type P cylinder. Before proceeding to cut the disc, the distribution of the hardness values on two opposite side of the cylinder P was mapped. The weakest area of the weldments was the fine grain heat affected zone which was defined by the lowest hardness values. (Average base-metal: HV_{10} = 203; Average weld: HV_{10} = 225; Average Fine-Grain HAZ: HV_{10} = 195). Once this region was identified on both sides of the cylinder then an elliptical disc was cut along the demarcation line. Of course the initial thickness was kept at around 600 μm.

Later further polishing with the final grid at 1200 reduced the thickness to about 500 μm. Finally some hardness measurements were made on both sides of the SP sample finding approximately the same values corresponding to the minimum value found before the weld was mapped (top side: $HV_{10} = 194$; underside: $HV_{10} = 194$). Hence it is possible to be confident that this SP specimen was composed mainly of the fine grain heat affected zone.

4.9. Figures – experimental procedures

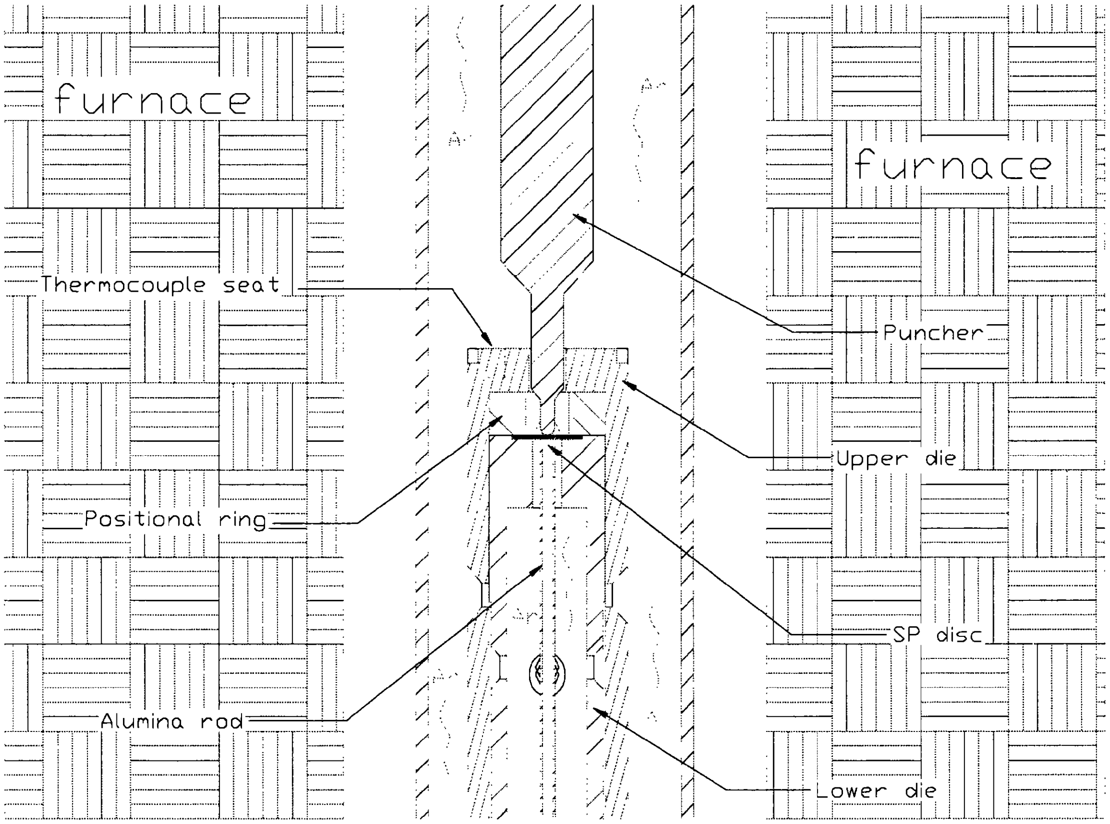

Figure 4-1: Schematic of experimental set-up.

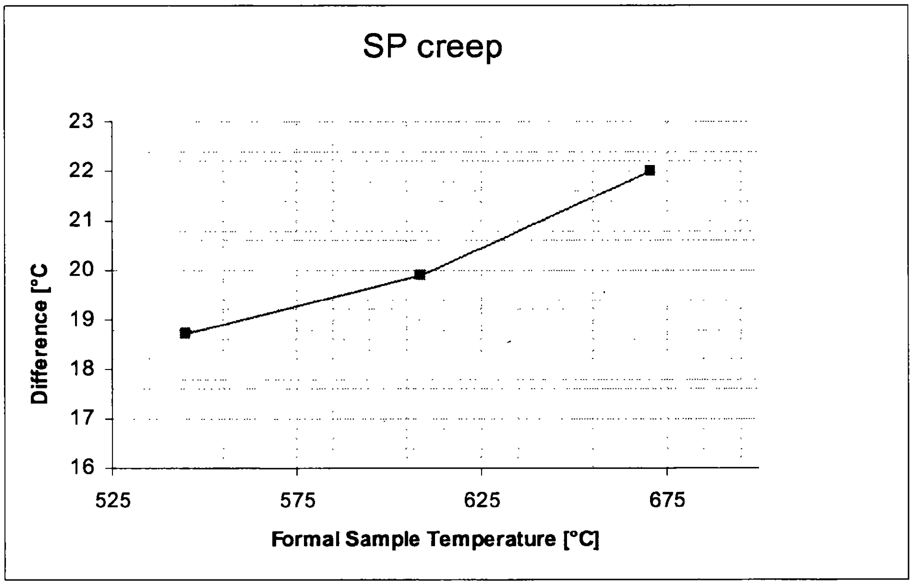

Figure 4-2: Calibration of the reference temperature of the sample (SP creep)

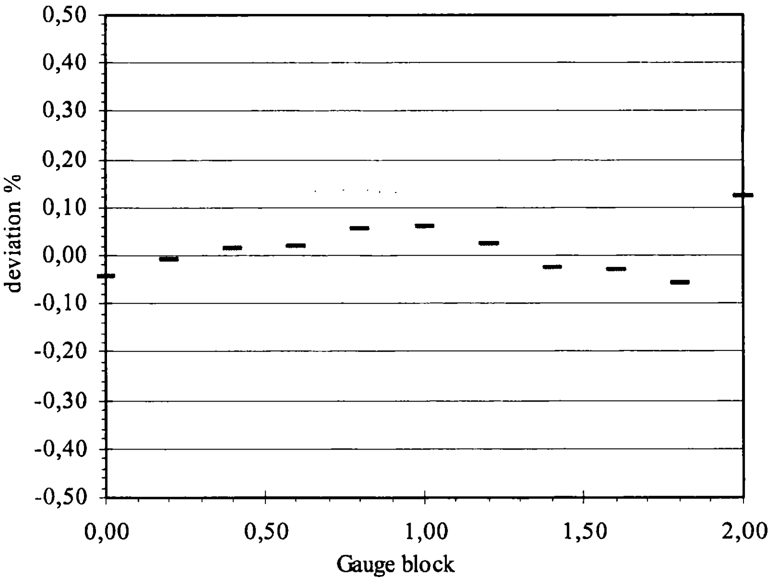

Figure 4-3: Deviation from linearity of the bottom LVDT .

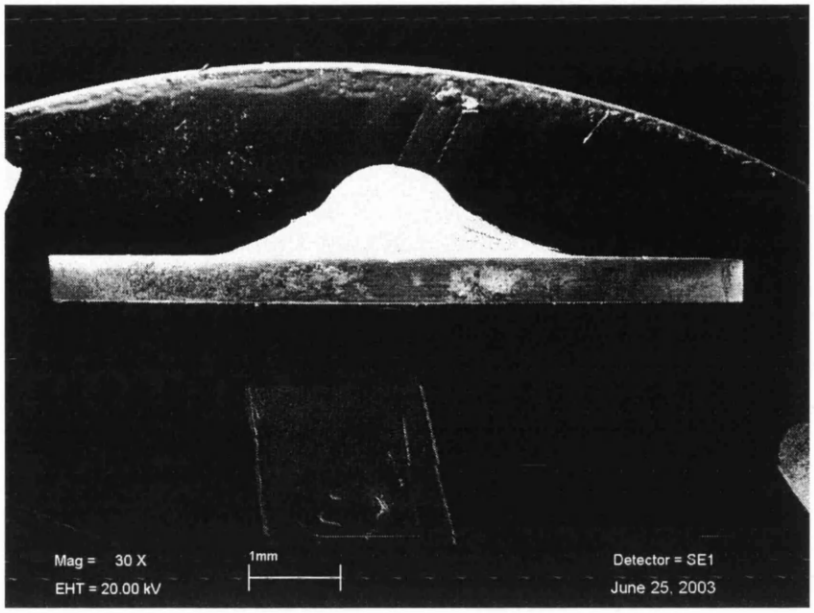

Figure 4-4: SEM image of the bulge shape of the interrupted test HM3-09.

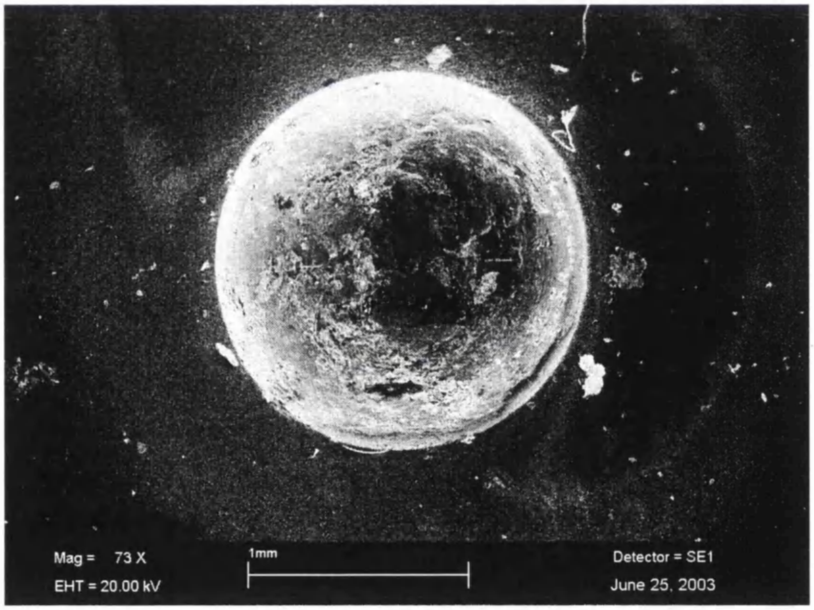

Figure 4-5: hemispherical print left by the puncher on the interrupted test HM3-09

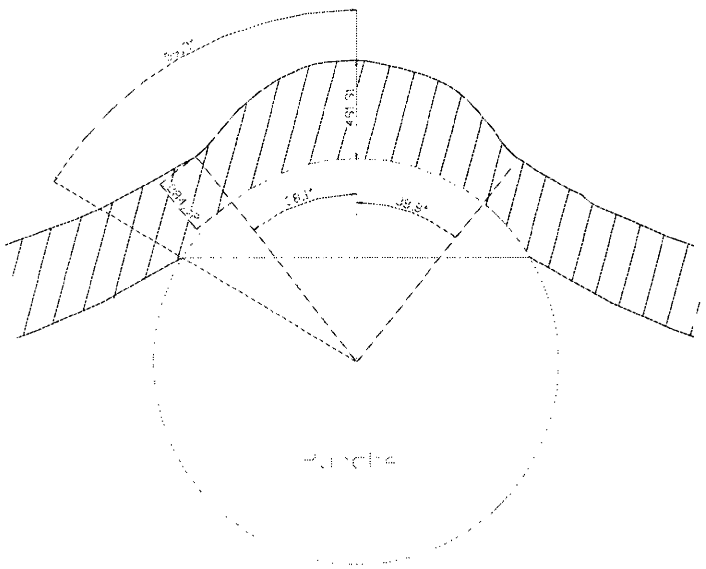

Figure 4-6: sketch of the deformed sample for the interrupted test HM3-09

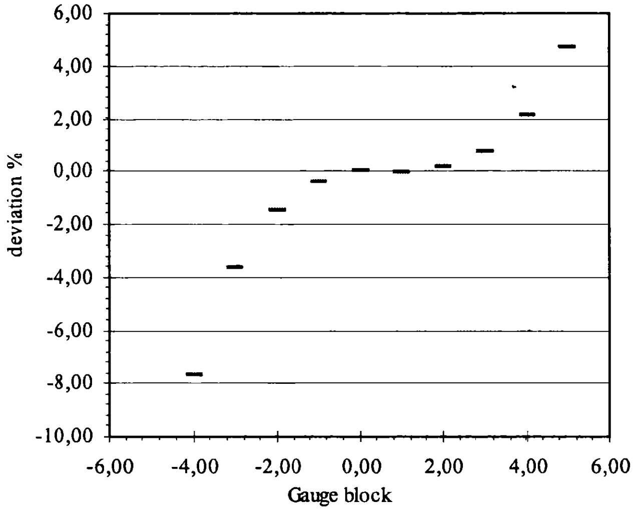

Figure 4-7: Deviation from linearity of LVDT in the SP tensile device.

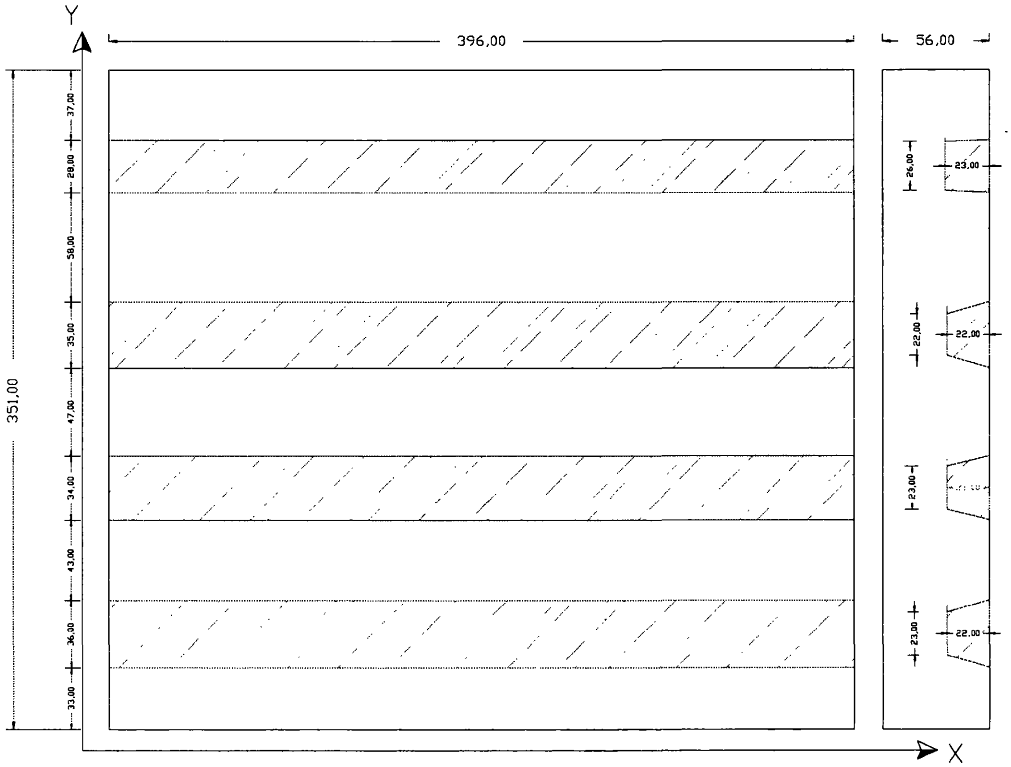

Figure 4-8: Dimension of the (2¼Cr-1Mo V) block with the four weldments lines.

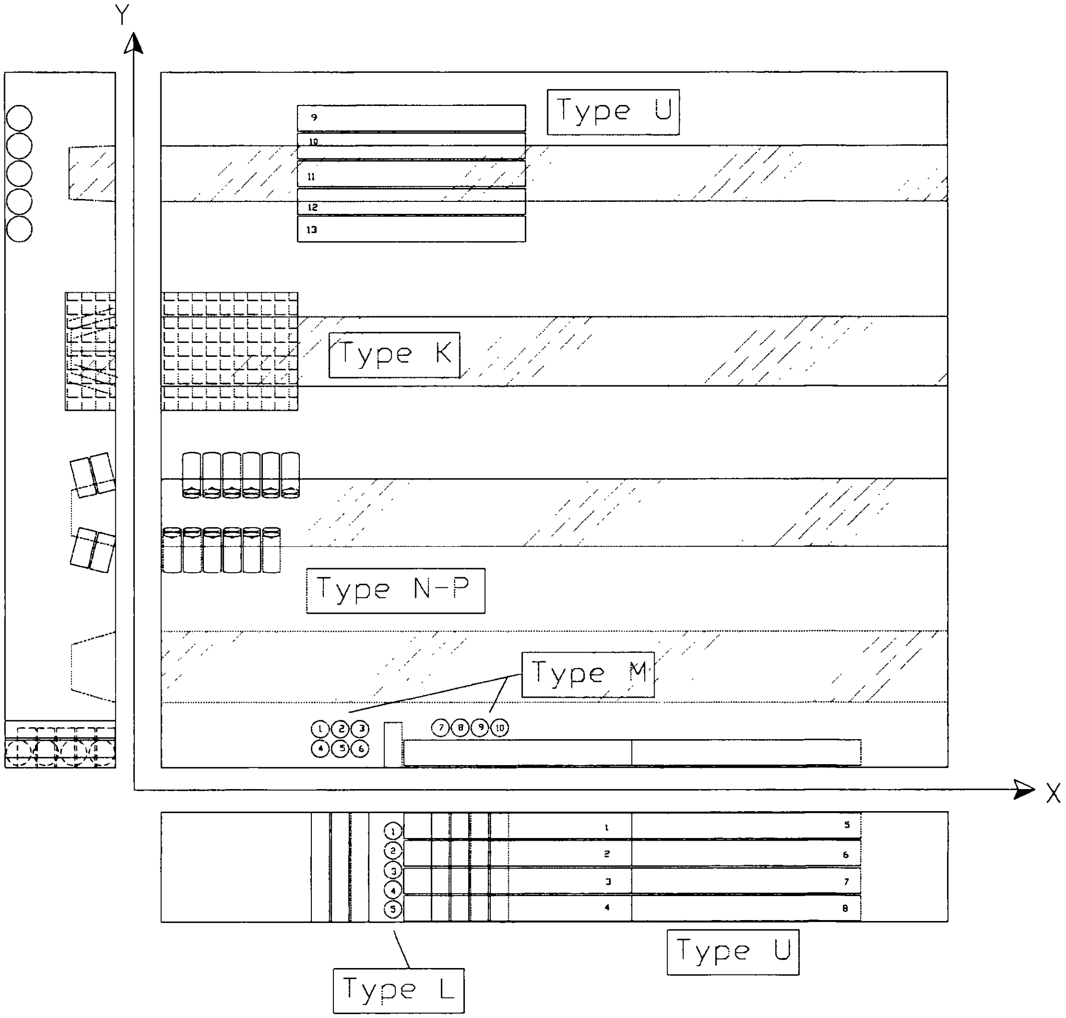

Figure 4-9: Schematic sketch with location of material removal from the block.

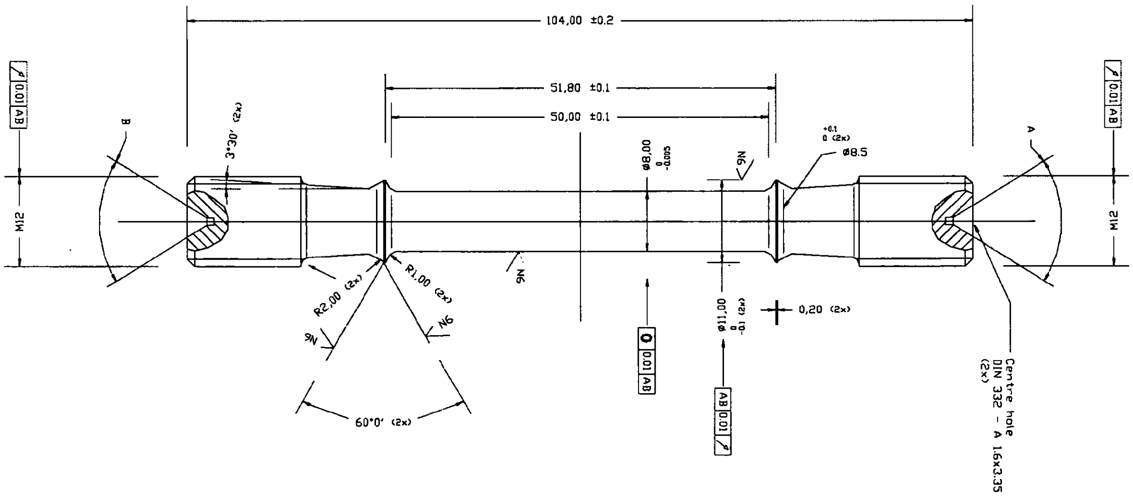

Figure 4-10: Design drawing for the uniaxial creep specimens.

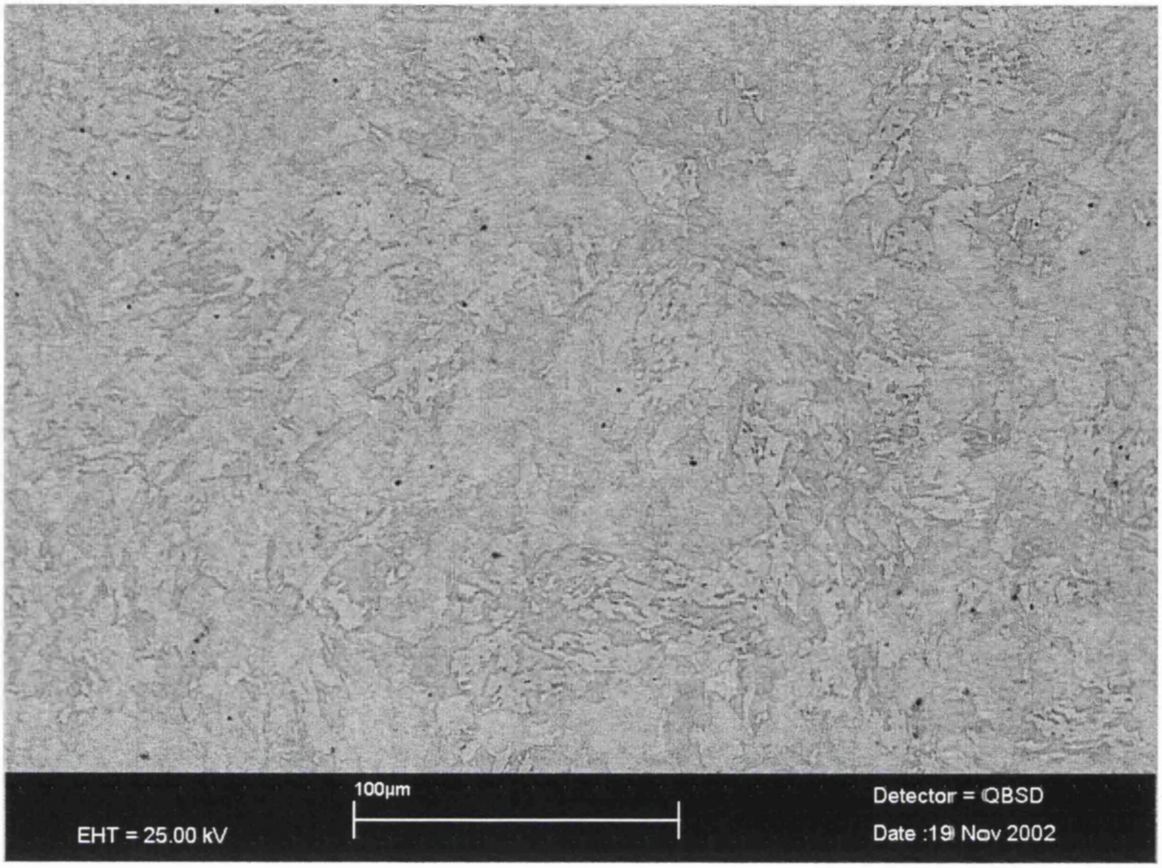

Figure 4-11: Picture taken by SEM with back scattered electrons. Cross section of cylinders type L

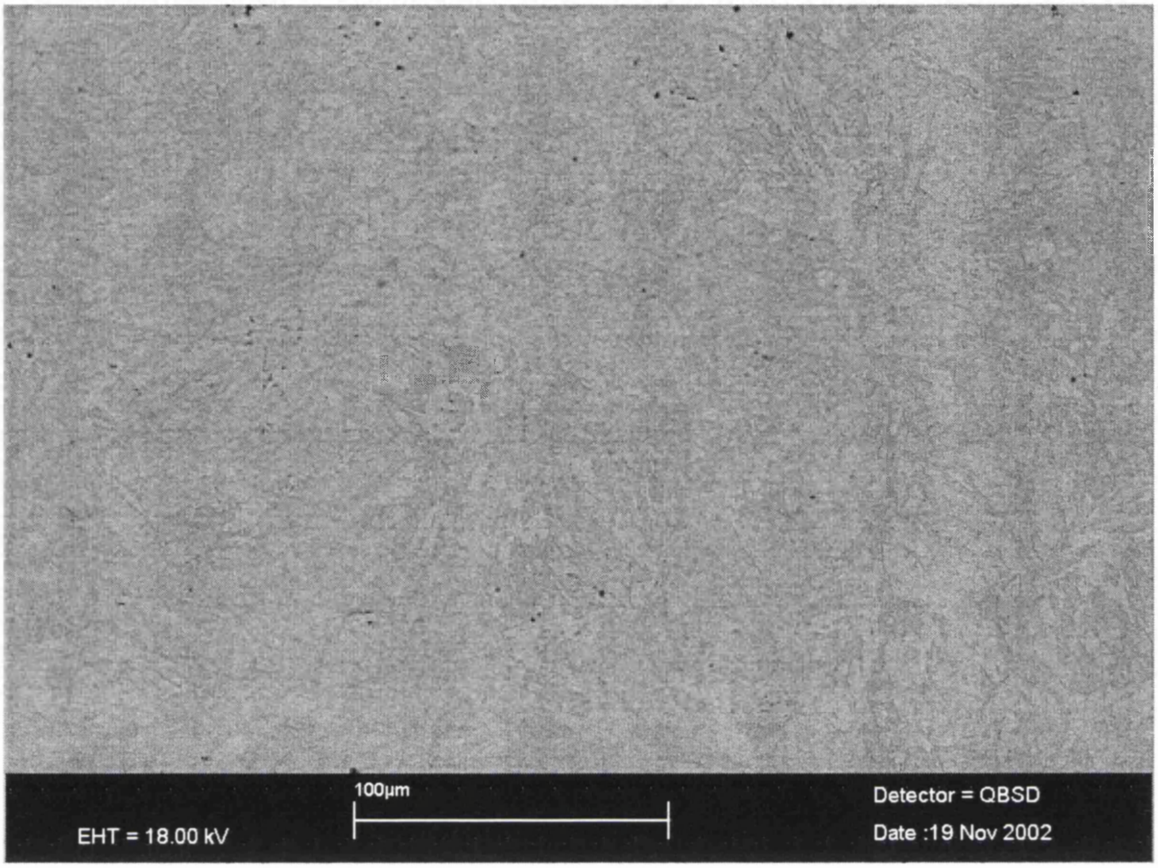

Figure 4-12: Picture taken by SEM with back scattered electrons. Cross section of cylinders type M

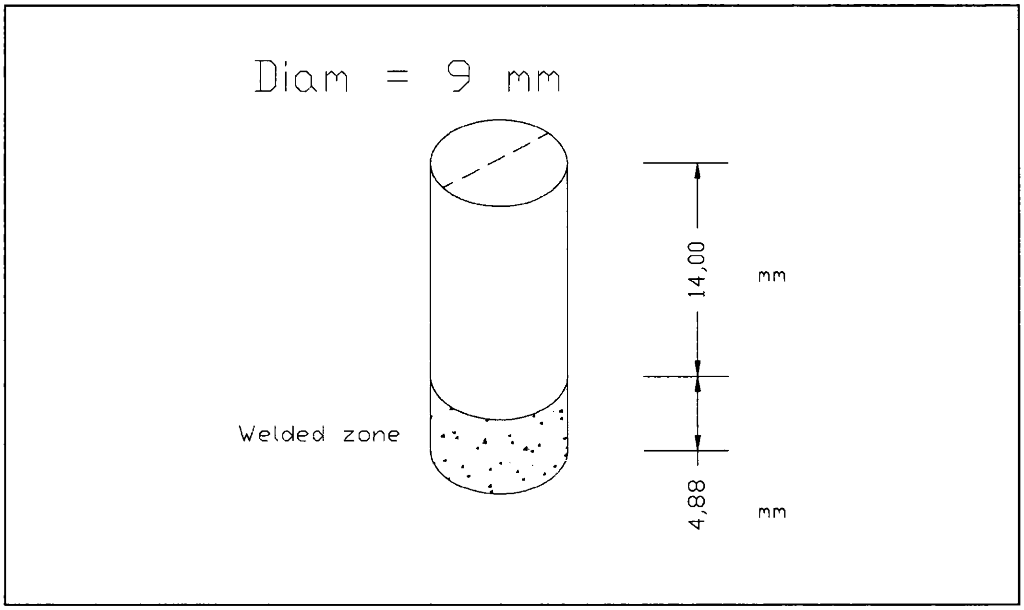

Figure 4-13: Sketch of the cylinders of type N or P with weldments.

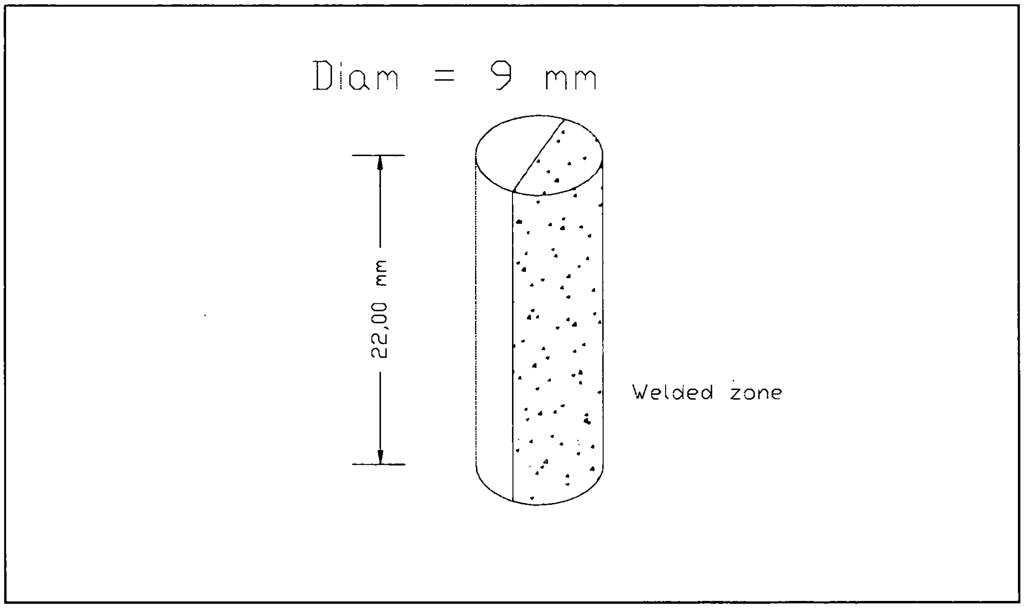

Figure 4-14: Sketch of the cylinders of type K with weldments.

5. Experimental Results

The specific outcomes of the present programme are considered in relation to the information gained through participation in a multi-laboratories Round Robin exercise focused on SP testing. The results are grouped according to the type of test with a basic explanation of the trends in behaviour reported. The detailed interpretation of the results is given in chapter 7.

5.1. Round robin exercise on the Cr-Mo rotor steel

In order to gain experience and to calibrate the SP equipment, preliminary experimental work during the first stages of the current project was performed as a JRC contribution to a Round Robin exercise. The round robin was a "Contribution In Kind" project that was carried out along the lines fixed from a series of discussions in the EPERC network (European Pressure Equipment Research Council), namely in the Technical Task Force 5 (TTF5, "Service Integrity during Operation"). The work followed the main scheme of co-operation, as agreed by the partners:

- UWS (University of Wales Swansea-UK) provided the material and uniaxial data for reference
- CESI (Milan- IT) made the co-ordination and produced/updated the test matrix
- JRC (Joint Research Centre- NL) collected and assessed the creep rupture data
- CESI, JRC, UWS and CRAC (Cracow University- PL) carried out the SP tests.

5.1.1. Round robin test conditions

Initially, it was planned to perform SP creep tests at individual, distinct temperatures, as typical with iso-stress curves derived from uniaxial testing. However, this was found to be difficult to manage in a round robin. Therefore, after some discussions between partners, the conclusion was drawn that only two or three temperatures had to be selected in advance and never modified, and multiple (probably 3) identical tests should be completed at each temperature. For the initial tests, the nominal expected life was selected to be about 100 h. The second condition was chosen to provide a duration of about 24 h and the third was intended for 1000 h. Based on the UWS data from conventional creep tests conducted on the same material, the partners suggested that, for getting the requested life of 100 h, the conditions should be a load of 300 N and a temperature of 625^0 C. The subsequent temperature levels were decided according to a CESI proposal by choosing a temperature, suitable to give a life of 25 hrs (3 tests) and finally another temperature to last 900 hrs. The other partners agreed and, finally the selected test conditions were 655°C, 625°C and 580°C, always with a load equal to 300 N. However, due to uncontrolled circumstances (CRAC) and also intentionally, a limited programme of "additional tests" addressed other values of temperature and load. After having concluded the definition phase (for partnership and test conditions), on 19 March 2001 the testing phase was started. Most of the tests were run in an argon protective atmosphere, except for CRAC who used air. Agreed geometry details were: t (thickness sample) = 0.5 mm, 2R (radius puncher) = 2.5 mm, D (diameter sample) = 8 mm, h (diameter receiving hole) = 4 mm. However, late in the programme, it was discovered that UWS had used 2R = 2 mm. As JRC had purchased their new SP apparatus from UWS, this same value 2R = 2 mm had also been used in JRC testing. Moreover, UWS used D = 9.5 mm for the SP sample diameter.

5.1.2. Round robin material

The partners decided to use a rather well characterised material for their investigations, namely, 1CrMoV rotor steel (Table 5-1). The material was provided to UWS by Innogy (UK). From the uniaxial tests, the value of Q_c is between 300 and 350 kJ/mol, the Norton coefficient n= 6.5, and the creep ductility is between 15% and 20% in strain.

1CrMoV																	
Element	C	Si	S	P	Mn	Ni	Cr	Mo	V	Cu	Al	Nb	Ti	As	Sb	Sn	Fe
wt %	.25	.24	.005	.013	.74	.60	1.36	.89	.32	.13	.002	<.003	<.003	.036	.022	.014	balance

Table 5-1: Composition of test material

5.1.3. Round robin results

The complete list of the creep SP test results obtained by the partners in this round robin is presented in the next table (Table 5-2):

Table 5-2: The SP creep test results obtained by each distinct partner

Lab	Temp.	Load	Time to rupture hrs (if different unit it will be indicated)	notes
CESI	655 °C	300 N	65.6	
CESI	655 °C	300 N	60.6	
CESI	655 °C	300 N	51.9	
CESI	625 °C	300 N	152 h but correction for under-loading 0.5/0.513 not applied	97.4 h, corrected for n=17.3 (slope of Swansea 1-D life data (but at much lower temperature); 128.6 h, using n=6.5, exponent suggested by Swansea: this is the creep life used in all present analyses in this report
CESI	625 °C	300 N	152.5	
CESI	625 °C	300 N	145.6	
CESI	625 °C	300 N	218.7	
CESI	580 °C	300 N	1362	
CESI	580 °C	300 N	1623	
CESI	580 °C	300 N	1825	
JRC	605 °C	300 N	78.59	Corrected temperature value (-20°C)
JRC	605 °C	300 N	77.45	Corrected temperature value (-20°C)
JRC	605 °C	300 N	97.92	Corrected temperature value (-20°C)
JRC	605 °C	300 N	65.44	Corrected temperature value (-20°C) Test on disc initially cut at 700 μm
JRC	605 °C	300 N	127.99	Corrected temperature value (-20°C) Test in Air
JRC	605°C	300 N	84.22	Corrected temperature value (-20°C) Test on disc initially cut at 700 μm
JRC	635°C	300 N	22.76	Corrected temperature value (-20°C)

Lab	Temp.	Load	Time to rupture hrs (if different unit it will be indicated)	notes
JRC	635°C	300 N	25.09	Corrected temperature value (-20°C)
JRC	560°C	300 N	1027	Corrected temperature value (-20°C)
UWS	625 °C	300 N	29	
UWS	625 °C	300 N	26	
UWS	625 °C	300 N	26	
UWS	625 °C	300 N	22	
UWS	605 °C	300 N	50	
CRAC	625 °C	300 N	210	In air
CRAC	625 °C	300 N	124	In air
CRAC	625 °C	300 N	339	In air
CRAC	625 °C	375 N	12	In air
CRAC	660 °C	300 N	49	In air
CRAC	660 °C	300 N	37	In air
CRAC	660 °C	300 N	41	In air
Additional tests data				
UWS	625°C	190 N	193	
UWS	625°C	245 N	50	
CESI	655 °C	270 N	44.5	
CESI	655 °C	240 N	52.3	
JRC	655°C	270 N	19.6	
JRC	655°C	240 N	20.3	
CRAC	650 °C	500 N	1888 min	In air
CRAC	650 °C	550 N	148 min	In air
CRAC	650 °C	600 N	96 min	In air
CRAC	650 °C	625 N	20 min	In air

Lab	Temp.	Load	**Time to rupture hrs** (if different unit it will be indicated)	notes
CRAC	690 °C	375	727 min	In air
CRAC	720 °C	375	363 min	In air
ERA	625	300 N	> 138	Interrupted at 0.5 mm deflection. In vacuum. Not put in plots and not used in the analysis

Table 5-2: The SP creep test results obtained by each distinct partner

The JRC tests, which were all carried out by this author, followed in principle the matrix of iso-load tests, but a post-test analysis for the thermal behaviour of the test equipment indicated the need to provide a fixed correction to the temperature data. Indeed, the temperature levels hereafter presented and discussed are the values shifted by minus 20°C below the nominal and initially scheduled values (refer to the experimental set-up in the "experimental procedure" section). CRAC carried out all their tests in air and adopted a matrix of tests not always reflecting the matrix selected. Unfortunately many test covered very short-term conditions. UWS ran just a few tests and they accomplished the fixed iso-load matrix only for the middle duration tests (a single test is available with a longer time to failure). CESI completed the matrix of the iso-load tests and performed 2 additional tests.

The results obtained in all the tests carried out in the iso-load programme are presented in Figure 5-1 [pag. 98] in terms of temperature vs. time to failure plot. This plot does not include the "additional test" data, (i.e. values of loads different from 300 N), because the most interesting discussion concerns the iso-load results. The results appear to be distributed along different lines for the different laboratories. The results can be divided in two groups: the JRC&UWS and the CESI&CRAC. The scatter in terms of time between the two groups is of the order of factor 5. In spite of these significant variations, the results are on lines parallel to each other and the results of individual laboratories show quite good reproducibility. The comparable pattern of results at UWS and JRC is a particularly good sign, because the two partners use the same equipment (developed by UWS).

5.2. Creep results for the 2¼ Cr, 1 Mo V modified

The creep tests run under this project were both conventional uniaxial creep tests and SP creep tests. The results can be categorized in two groups: the iso-stress tests (iso-load for SP tests) and the iso-thermal tests. The test conditions were chosen in order to achieve a reasonable time of failure that could range between 100 h and 1500 h for the as-received material. Further, the same conditions were applied to hydrogen-damaged material. Two levels of damage were chosen and a label expressing the H2 exposure time, 3000 h and 5000 h, will identify the respective results. For all conditions, just one single test is performed up to failure. Later, interrupted SP tests were intentionally carried out in order to obtain experimental evidence for validating the stress-strain model proposed in this project.

5.2.1. Test conditions

Firstly, the conditions for the conventional uniaxial creep tests were defined. It is important to note that those test are all undertaken at a constant load, but the relatively small ductility of the material (2¼Cr1MoV) reduces the difference expected from a constant stress test. The temperature chosen for the iso-thermal tests was 600°C with the stress varying in the range of 130 –190 MPa. For the iso-stress tests, a stress of 190 MPa was chosen with temperatures varying in the range of 550° to 600° C. Once those uniaxial tests were concluded, the loads adopted in the equivalent (same temperature) SP tests were chosen in order to give approximately the same lives.

5.2.2. Creep results

The complete list of the creep test results, included SP interrupted tests is presented in the following tables (Table 5-3, Table 5-4, Table 5-5). These tables show that for the uniaxial creep test, as the stress and temperature increase, the life is reduced. Also, the SP results show that for increasing load and temperature the creep life is reducing. The results obtained on the aged material (hydrogen or thermal), show clearly a life reduction. The extent of such a reduction will be discussed in the next chapters. Note that in the Table 5-5 the stresses are given for the thinnest section and also for the critical area (c.a.). (Refer to the chapter 6: discussion)

Isostress (uniaxial) and Isoload (SP) creep results						
test type	**time fail (hr)**	**temp. (°C)**	**Label**	**material**	**Stress (Mpa)**	**Notes**
Uniaxial	1123	550	U-11	As received	190	Test started twice (second start after 100 hr) and finally interrupt at 95% creep life
Uniaxial	279	580	U-07	As received	190	
Uniaxial	70	600	U-12	As received	190	Change of load during test: time of failure calculated as fraction of the total time.
Uniaxial	8	600	U-01	H2 3000 hr	190	
test type	**time fail (hr)**	**temp. (°C)**	**Label**	**material**	**Load (N)**	**Notes**
SP	870	550	M1-01	As received	340	
SP	530	560	M1-02	As received	340	
SP	158	580	M1-11	As received	340	
SP	160	580	M1-14	As received	340	
SP	93	600	M1-03	As received	340	
SP	56	600	M6-01	As received	340	
SP	544	550	HM3-03	H2 3000 hr	340	
SP	195	560	HM3-02	H2 3000 hr	340	
SP	36	580	HM3-14	H2 3000 hr	340	
SP	21,5	600	HM3-01	H2 3000 hr	340	
SP	14,5	600	HM3-11	H2 3000 hr	340	
SP	123	560	HM4-01	H2 5000 hr	340	
SP	50,5	580	HM4-03	H2 5000 hr	340	
SP	11,5	600	HM4-04	H2 5000 hr	340	

Table 5-3: Iso-stress creep results for SP and uniaxial tests on both as received material and aged material.

Isothermal (uniaxial and SP) creep results

test type	time fail (hr)	stress (MPa)	Label	material	temp. (°C)	Notes
Uniaxial	1363	130	U-09	As received	600	
Uniaxial	816	140	U-10	As received	600	
Uniaxial	629	150	U-06	As received	600	
Uniaxial	70	190	U-12	As received	600	
Uniaxial	8	190	U-01	H2 3000 hr	600	
Uniaxial	137	140	U-04	H2 5000 hr	599	
Uniaxial	323	140	U-20	Therm. 3000 hr	600	Different size of the sample and no strain measurement

test type	time fail (hr)	Load (N)	label	material	temp. (°C)	Notes
SP	93	340	M1-03	As received	600	
SP	56	340	M6-01	As received	600	
SP	115	305	M1-07	As received	600	
SP	436	270	M1-08	As received	600	
SP	187	270	M6-10	As received	600	
SP	1215	230	M1-06	As received	600	
SP	21,5	340	HM3-01	H2 3000 hr	600	
SP	14,5	340	HM3-11	H2 3000 hr	600	
SP	107	270	HM3-13	H2 3000 hr	600	
SP	452	210	HM3-06	H2 3000 hr	600	
SP	11,5	340	HM4-04	H2 5000 hr	600	
SP	85	270	HM4-06	H2 5000 hr	600	
SP	448	210	HM4-05	H2 5000 hr	600	
SP	8	340	AM7-03	Therm. 3000 hr	600	
SP	85	270	AM7-02	Therm. 3000 hr	600	
SP	596	210	AM7-01	Therm. 3000 hr	600	

Table 5-4: Isothermal creep results for SP and uniaxial tests on both as received material and aged material.

test type	% creep life	Creep Phase	Load (N)	temp (°C)	min.th. (mm)	angle phi (deg)	angle phi contact (deg)	label	material	Stress min. thick. (Mpa)	Stress critic. area (Mpa)	Load / (stress c.a.)	Average ratio
SP	< 1	I°	340	560	0,465	17,0	29,0	M1-09	As received				
SP	< 1	I°	340	560	0,441	24,2	35,3	M1-10	As received				
SP	5	II°	340	560	0,390	29,0	48,4	M1-15	As received	201	175	1,94	1,89
SP	20	II°	340	560	0,361	32,2	52,9	M1-16	As received	183	155	2,19	
SP	40	II°	340	560	0,280	34,2	59,6	M6-02	As received	175	160	2,13	
SP	80	II°	340	560	0,215	45,0	64,2	M1-19	As received	181	181	1,88	
SP	80	II°	340	560	0,240	43,4	60,8	M6-12	As received	187	186	1,83	
SP	50	II°	270	600	0,294	34,6	53,4	M9-01	As received	165	150	1,80	
SP	60	II°	270	600	0,238	36,7	60,9	M6-08	As received	151	145	1,86	
SP	97	III°	270	600	0,147	43,0	65,9	M6-11	As received	185	185	1,46	
SP	40	II°	340	560	0,281	38,5	59,2	HM3-09	H2 3000 hr	178	150	2,27	2,19
SP	50	II°	340	560	0,294	37,0	59,6	HM3-10	H2 3000 hr	171	140	2,43	
SP	70	II°	340	560	0,197	44,5	67,5	HM3-07	H2 3000 hr	177	165	2,06	
SP	75	II°	340	560	0,231	46,0	62,4	HM3-12	H2 3000 hr	180	170	2,00	
SP	40	II°	340	560	0,290	36,7	52,5	HM4-08	H2 5000 hr	218	190	1,79	1,71
SP	15	II°	340	560	0,307	34,3	50,7	HM4-10	H2 5000 hr	222	180	1,89	
SP	97	III°	340	560	0,161	48,0	62,1	HM4-02	H2 5000 hr	232	232	1,47	
SP	50	II°	340	560	0,268	37,3	54,3	AM7-05	therm.3000 hr	216	200-Extrp	1,70	1,70
SP	55	II°	340	580	0,242	41,4	55,2	WP9-01	weld(FG-HAZ)	223	205-Extrp	1,66	1,66

Table 5-5: SP interrupted creep tests on both as received material and aged material.

The SP results are described by the creep curve where the vertical deflection is plotted versus time (e.g. the test M6-10 shown in Figure 5-2, p. 98) and by the course of the deflection rate plotted against the vertical deflection (Figure 5-3, p. 99). A linear dependence of the time of failure on the minimum deflection rate is obtained as shown in Figure 5-4 (p. 99). The interrupted tests are also included if they lasted enough time to pass the point of the minimum deflection rate. In these cases, the failure time is calculated by means of the equation emerging from the linear fit of the completed tests points. The uncertainty then is fixed at ± 15% of calculated time of failure.

5.3. Thesis SP tensile results

The SP tensile tests were carried out on as-received material, on hydrogen-damaged material exposed for 5000 hours and on the thermal-aged material exposed at high temperature for 3000 hours. The SP tests were carried out at the crosshead speed of 0,003 mm/sec and all at room temperature (20 - 25°C). It is important to note that the puncher radius for these tests was R=1.25 mm, while in the creep test it was R=1.00 mm because of the different equipment employed.

5.3.1. SP tensile results

The complete list of the SP tensile test results (they are all interrupted tests) is presented in the following table (Table 5-6). This table shows that the load is increasing with increasing vertical deflection (at least before reaching the point of the maximum load) as it is expected considering the hardening process occurring in a tensile test. The results on damaged material show a perceptible drop of the maximum load and a slight shift of such a point at higher vertical deflection.

SP tensile tests								
test type	Vertical deflection (mm)	Load (N)	min.th. (mm)	angle phi (deg)	angle phi contact (deg)	label	material	note
SP	1,570	1658	0,285	38,0	69,9	M6-18	As received	interrupted at max load
SP	1,650	1704	0,270	37,0	73,5	M6-19	As received	interrupted at max load
SP	0,580	706	0,458	18,8	32,6	M6-20	As received	
SP	1,030	1304	0,393	31,5	52,1	M6-21	As received	
SP	1,857	1580	0,210	43,5	84,0	M1-20	As received	interrupted at failure
SP	1,643	1573	0,258	41,7	72,6	HM4-11	H2 5000 hr	interrupted at max load
SP	0,043	204	0,499	/	/	HM4-12	H2 5000 hr	
SP	0,121	302	0,493	/	/	HM4-13	H2 5000 hr	
SP	0,242	405	0,490	9,7	19,8	HM4-14	H2 5000 hr	
SP	0,422	504	0,473	14,0	26,5	HM4-15	H2 5000 hr	
SP	0,546	603	0,459	18,1	30,1	HM4-16	H2 5000 hr	
SP	0,886	1006	0,407	25,8	45,5	HM4-17	H2 5000 hr	
SP	1,281	1405	0,344	38,8	60,7	HM4-18	H2 5000 hr	
SP	1,950	1486	0,157	47,3	80,3	HM4-07	H2 5000 hr	interrupted at failure
SP	1,713	1571	0,239	43,5	74,6	AM7-06	therm.3000 hr	interrupted at max load
SP	0,044	206	0,490	/	/	AM7-07	therm.3000 hr	
SP	0,109	303	0,492	/	/	AM7-08	therm.3000 hr	
SP	0,229	406	0,484	9,1	18,9	AM7-09	therm.3000 hr	
SP	0,389	506	0,475	14,5	24,9	AM7-10	therm.3000 hr	
SP	0,514	607	0,457	18,0	30,0	AM7-11	therm.3000 hr	
SP	0,844	1009	0,418	25,5	43,6	AM7-12	therm.3000 hr	
SP	1,273	1412	0,352	32,9	60,4	AM7-13	therm.3000 hr	
SP	1,927	1434	0,178	45,0	80,2	AM7-04	therm.3000 hr	interrupted at failure

Table 5-6: Results of the interrupted SP tensile tests on both as received and aged material.

5.4. Figures – experimental results

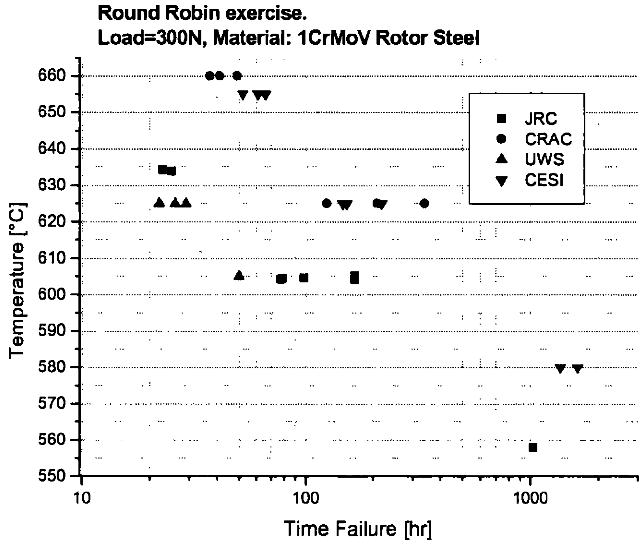

Figure 5-1: SP creep results for round robin exercise. Iso-load (300 N).

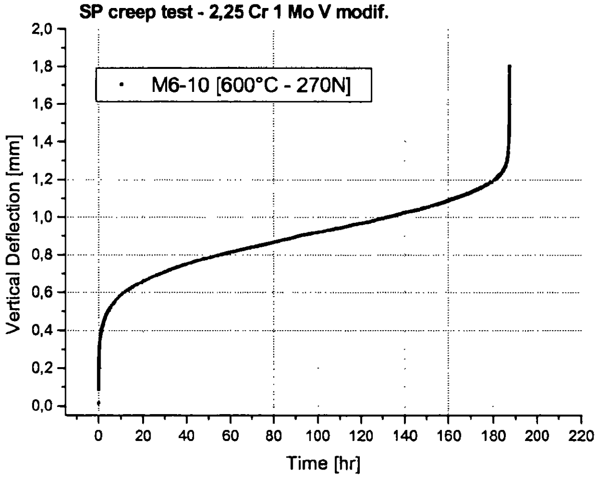

Figure 5-2: Example of a SP creep curve (test: M6-10)

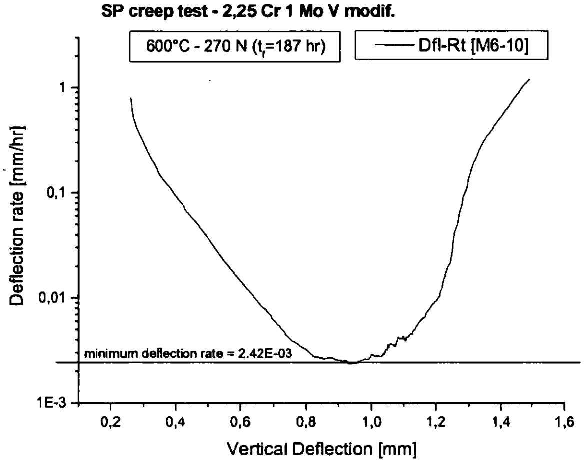

Figure 5-3: Example of plot - deflection rate vs. vertical deflection - [M6-10]

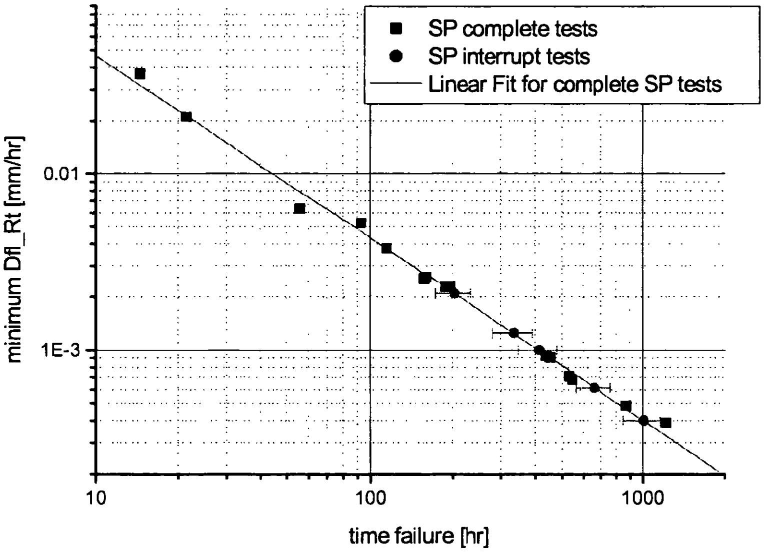

Figure 5-4: Logarithmic relationship between time of failure and minimum deflection rate in SP tests

6. Presentation of the model

The main doubts regarding the applicability of the SP technique are linked to the uncertainty about the evolution of stress and strain within the SP sample. Unless a link can be made to the uniaxial creep properties of the material, no prediction of remaining creep life can be made. In order to answer such doubt, a stress-strain model is introduced and a relatively simple relationship expressing the ratio of the applied load in the SP test to the resulting appropiate stress is established.

6.1. Why is stress so important?

The SP test is a promising non-destructive technique for estimating the residual life of in-service industrial components. The technique would work if it was possible to define the stresses that lead to failure at the critical location in the component. Thus, the SP test conducted on a specimen extracted from the component would answer such a question, only if the state of stress and strain were known during the whole test. This is a quite complex problem in the SP test, because a tri-axial state of stress is acting, which is most certainly also varying with time. However, in spite of these difficulties a model has been proposed taking into account the results from the Round Robin exercise in which the author participated [Bicego (2003)].

6.2. SP creep test. Stress evaluation and the Round Robin exercise.

In the SP creep test, a constant load is applied to the SP disc by a hemispherical puncher. The resulting deformation is recorded by the vertical displacement taken at the underside of the disc. If this displacement is plotted versus time, the resulting curve will look like the typical uniaxial creep curve characterized by a secondary and tertiary creep phase (Figure 6-1, p. 127). That is not the only similarity with the classical uniaxial creep test. In fact, considering the minimum deflection rate or the failure time, a power-law relationship is also valid for the SP tests [Parker (1998), Komazay (2000)].

Eq. 6-1

$$\dot{d}_{\min} \propto {}^{1}\!/_{t_f} = B \cdot L^{m} \cdot e^{-\frac{Q_c}{RT}}$$

Those similarities allowed those authors to confirm the existence of a relationship between the stress in the uniaxial creep test and the load in the SP creep test. However, this load/stress ratio was based only on empirical assumptions.

The Round Robin exercise on 1Cr Mo V steel, presented a suitable opportunity to approach the problem from an analytical point of view. As detailed in the experimental results (Chap. 5) the round robin data sets appear to belong to two populations; the CESI and CRAC on one side and JRC and UWS on the other side. This work indicated that the main reasons for such a discrepancy was the differences in the puncher radius. CESI and CRAC used a puncher with a radius 25% bigger than the other two partners, JRC and UWS. The use of some simplified models proposed in the literature for correlating the punch load to the uniaxial stress in a conventional creep test, based on an estimation of the membrane-stretching stress in the SP specimen, led to a significant grouping of all

SP results for the four laboratories into a single trend. The analysis of the round robin discrepancies has been performed by employing three different load/stress relationships. However, because the puncher radius R is in all cases linearly dependent on the load/stress ratio, no substantial differences emerge in the analysis. The first relation was from the work of Tettamenti (1998)

Eq. 6-2
$$L/\sigma = [2\pi \cdot t \cdot (R + t/2)\sin\phi_c] \cdot \sin\phi_c$$

The second relationship was proposed by Dobes-Milicka, [Dobes, (2001)]:

Eq. 6-3
$$L/\sigma = \frac{2\pi R \cdot t \cdot \sin\phi_c \cdot \tan\phi_c}{\left(1 + \tan^2\phi_c\right)^{1/2}}$$

and the third was suggested by Chakrabarty (1970)

Eq. 6-4
$$L/\sigma = 2\pi R \cdot \sin^2\phi_c \cdot t_0 \cdot \left\{\frac{1+\cos\phi_c}{1+\cos\phi_c}\right\}^2$$

In the above equations, t_0 is initial thickness, t is a sort of uniform reduced thickness, ϕ_c the contact angle which defines the extension of the contact, and R the puncher radius. All these relationships are built up by considering the equilibrium of the SP specimen at the given boundary conditions. Unfortunately, although the main hypothesis of the membrane-stretching mode for specimen deformation is assumed, such models do not take into account the necking process. Thus, the thickness t for equations Eq. 6-2 and Eq. 6-3 is calculated assuming a uniform reduction all along the specimen, bearing in mind that the volume of the specimen is kept constant during plastic deformation. Then, the contact angle for the last two equations was calculated by a semiempirical relationship that links the measured vertical deflection *d* with the radius *c* of the hemispherical contact surface (half chord) between the puncher and the specimen. Alternatively, for the Tettamenti relationship, the contact angle was defined with a fixed value. These proposed models then gave approximate results and they could only be used for qualitative studies. The equivalent stresses were calculated for all the SP data, as all the partners used the same puncher of 2R = 2.5 mm, and then plotted together with the uniaxial data in a chart where the Larson-Miller parameter is a function of stress on a logarithmic scale. [Figure 6-2, pag. 128]. The results of this round robin exercise showed that, although such models are quite approximate and inexact, the logic behind the idea worked well and any stress model should relate linearly the stress with the load and with the puncher radius. Thus, such an idea was considered to be a good starting point for the further development of a better model.

The analytical model to be introduced was based on the equilibrium in the SP specimen at the given boundary conditions, but this time looking more carefully at the real behaviour of the SP specimen. In order to develop this model, it was worthwhile to know, for each step of the test, how and by how much the SP sample was deformed.

6.3. Qualitative description of the SP specimen deformation

The deformation of large and thin plate has been the object of study around the middle of the 20th century, because of the needs of the metal forming industry. Some theoretical analysis has been carried out by Timoshenko (1957) within the framework of the large plate bending theory, and more specific applied research has been concerned with stretch forming over hemispherical punch heads by Chakrabarty (1970) (Eq. 6-4, pag. 102). Other models have then been proposed, but without substantial change in respect to their precursor (Eq. 6-2 [pag. 102] and Eq. 6-3 [pag. 102]). In order to understand better the evolution of stress and strain, it is best to start by analysing in detail the deformation of the SP specimen.

Two separate analyses were done both for the SP creep test and for the SP tensile test, with the plastic behaviour being different in the two cases. Also, it is important to keep in mind one principal difference in the experimental set-up for the two test facilities. This was the difference in the puncher radius, which was R = 1.25 mm in the tensile test equipment, instead of the 1.00 mm for the SP creep facilities. Finally, in order to avoid misunderstanding in the interpretation of the geometrical features of the SP specimen, any sliding of the specimen had to be excluded by assuring an adequate clamping force.

6.3.1. Specimen deformation in the SP creep test

Once the load is applied on the specimen, a certain percentage of the total vertical deflection occurs at this very first stage of the test. The amount of such preliminary vertical deflection is directly related to the temperature and to the applied load. Later, a secondary creep phase will follow with an approximately constant deflection rate. At the end of this phase, a very fast rate will bring the sample to failure (tertiary creep phase). Now, the question is, how was the sample deforming during the test? In order to respond, some SP creep tests were interrupted and the geometrical features were analysed (Figure 6-3, p. 129 - Figure 6-4, p. ~~32)~~ 130).

First of all it is worth emphasizing how the creep ductility can influence the way in which the SP specimen deforms. It has been shown for uniaxial creep tests that the creep ductility generally increases at higher temperatures and loads [Cane (1981), Greenwood (1973)], and such behaviour is expected also in the SP specimen. Another important factor, which is normally decreasing the creep ductility, is progressive damage or ageing of the material [Bocquet (2000), Byeon (2003)]. This aspect will be again considered in the chapter where the results will be discussed.

Actually, the vertical deflection, which is the most typical output for a SP test, only partially shows what is going on in the sample. Other geometrical factors play a role in the description of the deformation. The thinning of the sample along the contact area, the angle ϕ pointing out the thinnest section, and the contact radius c are also important and also they have links with the vertical deflection.

In more detail, we now consider how such geometrical factors evolve during a creep test. A significant fraction of the contact radius c is gained during the very first moments of the test. This fast rate is due to the very high stresses acting beneath the small contact area between the hemispherical punch and the sample at the beginning of the test. The resulting deformation is then mainly due to bending of the specimen. Afterwards, as the contact area is increasing, it will increase the portion of sample bearing the load and consequently the stresses will decrease, leading to a slower ratio. The small hemispherical cup formed just beneath the tip of the puncher will not be substantially deformed any more and the deformation of the rest of the specimen starts to be driven by a membrane-stretching process, which will be more evident as the vertical displacement rate turns out to be about constant. Hence, the membrane-stretching process of deformation in the SP creep test is predominant compared with the bending mode, which is only present at the early stage of the test [Komazai (2000)]. This can be appreciated by inspecting the graph where the vertical deflection is plotted against the contact radius $c = R \cdot \sin\phi_c$ (Figure 6-5, p. 131). This plot represents only the data referring to the as-received material tested at 340 N and 560° C. A transition region, which lasts for relatively short time, can also be defined.

Before necking appears at the underside of the specimen, a section with a minimum thickness can be defined. In fact, at the contact surface, the specimen is forced to assume a hemispherical shape of radius R due to the action of the ball puncher. Then, the combination with the shape that the surface of the specimen assumes at the underside creates a gradient in the thickness distribution along the contact area with a well defined minimum. Later, necking appears at the underside when the material reaches its creep plastic limit. This has been observed to happen around 20-30 % of the sample creep life. The annular area defined by the necking will lead the specimen later to failure. The thinnest section is delineated by the contact angle ϕ.

6.3.2. Specimen deformation in the SP tensile test

In the SP tensile test, the load is applied to the specimen in order to give a constant deflection rate. So, the load rate is different at each stage of deformation. At the beginning it is linear, because the specimen is bending in the elastic regime, although some limited yielding occurs in the quite small contact area due to the indentation phenomenon. Very soon, the deformation departs from linearity because the material starts to yield. The bending mode is still going on (plastic bending), but soon the specimen enters into a transition phase where the deformation mode switches to membrane-stretching. Finally, the load reaches the maximum peak value with the onset of the plastic instability, which leads to necking at the underside of the SP specimen at a certain contact angle ϕ. Subsequently, the membrane mode of deformation is concentrated within this annular area defined by the necking, which will lead eventually to failure. The transition between the bending and stretching membrane mode can be defined by considering the relationship between the vertical deflection d and the contact radius c (Figure 6-6, p. 132) [Mao (1987)], as was done for the SP creep test. In this case, the transition between the bending and the membrane-stretching mode was less definite and it persisted for a relatively long time.

At this point, before entering in more detail about the equilibrium of such deformed SP specimens, some simplified stress models for uniaxial specimens are introduced.

6.4. Standard uniaxial stress model

In the conventional uniaxial tests, the stresses are normally expressed as the engineering value, which means that the axial stress is calculated for a constant cross section. In reality, especially at high degree of plastic deformation, the cross section tends to decrease, which leads the effective true stress to increase. Eventually, when necking starts the stress state becomes slightly triaxial, with a further increase of the main axial stress. A more consistent analysis of the stress state in the neck has been carried out by several authors [Bridgman (1944), Davidenkov (1946)]. These models show an increase in the nominal stress in the neck as function of the residual radius of the sample *a* and of the necking external radius *R* [Figure 6-7, p. 133] as:

Eq. 6-5

$$\sigma_z = \sigma_n \cdot \frac{1+\ln\dfrac{a^2+2aR-r^2}{2aR}}{\left(1+\dfrac{2R}{a}\right)\cdot\ln\left(1+\dfrac{a}{2R}\right)}$$

This model shows also that the highest stress should act at the centre of the specimen (r=0). This is a good approximation as the uniaxial sample often starts to crack at the centre of the sample.

This model could be applied both to the conventional uniaxial creep test and to the uniaxial tensile test. It is then possible to evaluate the evolution of stress and strain within standard specimens from the beginning of the test up to failure.

6.4.1. Stress evolution in the uniaxial creep test

The stress evolution in a uniaxial creep test at constant load is strictly related to the creep ductility of the material, which can be expressed by the elongation at failure and by the reduction of area if eventually a neck appears.

In order to plot the possible evolution of stress in the uniaxial specimen for the material currently employed in this project, the interrupted test U11 at 550°C and 190 MPa on the "as-received" material was selected. This test had been interrupted before failure at around 95 % of the sample creep life. The overall diameter of the specimen was found to reduce from D_0 = 8.02 mm to D = 7.70 mm with some evidence of necking. Considering the axial stress calculated on the current diameter of D = 7.70 mm:

Eq. 6-6

$$\sigma_n = 190 \cdot \frac{4\pi \cdot D_0^2}{4\pi \cdot D^2} = 206\text{MPa}$$

and adopting the Eq. 6-5 (p. 108) with the measured value of a=3.2mm and R=32mm. This was calculated as a maximum value for the stress, $\sigma_z = \sigma_n \cdot 1{,}02 = 210$ MPa (at 95 % of the sample creep life). This was around 10 % higher then the nominal value of 190 MPa. Simplifying, the stress evolution can be directly related to the strain evolution. Thus, the final value of stress at rupture can be found considering directly the values of strain at failure. In the range of temperature and stress actually employed for the "as-received" material, the strain at failure was normally around 20% (Figure 6-14). Thus, the final value of stress can be considered 20% higher than the nominal value. Then, for instance, adopting this method for the above mentioned interrupted test U-11 and for the complete test U-07 at 580°C and 190 MPa, then the stress evolution can be plotted against the % of creep life [Figure 6-8, p. 133]. The test at 560°C was most probably behaving in the same way.

6.4.2. Stress evolution in the uniaxial tensile test

In the uniaxial tensile test the as-received material showed very high strength and a consistent elastic modulus. The necking started to appear in the uniaxial specimen only after the engineering stress exceeds the σ_{UTS}. The stress calculated up to this point, just considering the cross section reduction as a consequence of the plastic deformation at constant volume, could be defined realistically as the real axial stress. Referring to a tensile test undertaken for the same batch of material in another project within the JRC

[Figure 6-9, p. 133] (speed = 0,001 mm/sec.), when the engineering stress reached the σ_{UTS} of 632 MPa, the real stress should be around 730 MPa.

6.5. Proposed SP stress model

The portion of sample for which the model should attempt to describe the evolution of stress is the one where the failure takes place. During the SP test, as the contact increases, the failure region is shifting from the unsupported region to the contact region. The proposed models will then define the stress-strain state in both regions and indicate whether the governing stress regime is the bending or the membrane-stretching regime. These models are based on finding the equilibrium of any elements of the SP specimen at any time and at the given boundary condition.

6.5.1. Bending mode in the unsupported and contact region

Assume an infinitesimal portion of the small punch disc in the unsupported region of the deformed sample, defined with a cylindrical coordinate system by the radius r (referred at the radius due to the circular shape of the disc), the angle θ, and the perpendicular coordinate z, where the origin is at the middle plane defined by $t_o/2$, where t_o is the initial thickness (Figure 6-10, p. 135). In detail, the infinitesimal element will be like that shown in the Figure 6-11, p. 136. The equilibrium of this element has to be detailed along the three principal directions, which are the circumferential, the vertical and the radial directions.

- For equilibrium in the circumferential direction:

$$\left(\sigma_{\theta 2}-\sigma_{\theta 1}\right)\cdot dr\cdot dz+\left(\tau_{r\theta 2}\cdot r_2-\tau_{r\theta 1}\cdot r_1\right)\cdot d\theta\cdot dz+\left(\tau_{z\theta 2}-\tau_{z\theta 1}\right)\cdot r\cdot d\theta\cdot dr+$$
$$+\left(\tau_{\theta r1}+\tau_{\theta r2}\right)\cdot dr\cdot dz\cdot \sin\left(\frac{d\theta}{2}\right)=0 \qquad \textbf{Eq. 6-7}$$

- For equilibrium in the *z* direction:

$$\left(\sigma_{z2}-\sigma_{z1}\right)\cdot r\cdot d\theta\cdot dr+\left(\tau_{\theta z2}-\tau_{\theta z1}\right)\cdot dr\cdot dz+\left(\tau_{rz2}\cdot r_2-\tau_{r\phi 1}\cdot r_1\right)\cdot d\theta\cdot dz=0 \qquad \textbf{Eq. 6-8}$$

- For equilibrium in the radial direction:

$$\left(\sigma_{r2}\cdot r_2-\sigma_{r1}\cdot r_1\right)\cdot d\theta\cdot dz+\left(\tau_{zr2}-\tau_{zr1}\right)\cdot rd\theta\cdot dr+\left(\tau_{\theta r2}-\tau_{\theta r1}\right)\cdot dr\cdot dz+$$
$$-\left(\sigma_{\theta 2}+\sigma_{\theta 1}\right)\cdot dr\cdot dz\cdot \sin\left(\frac{d\theta}{2}\right)=0 \qquad \textbf{Eq. 6-9}$$

Assuming now the *sin* of a small angle as equal to the angle itself and dividing the three equations by the expression "dθ·dz·dr" then the system of equations become:

$$\begin{aligned}
&\frac{\left(\sigma_{\theta 2}-\sigma_{\theta 1}\right)}{d\theta}+\frac{\left(\tau_{r\theta 2}\cdot r_2-\tau_{r\theta 1}\cdot r_1\right)}{dr}+r\cdot\frac{\left(\tau_{z\theta 2}-\tau_{z\theta 1}\right)}{dz}+\frac{\left(\tau_{\theta r1}+\tau_{\theta r2}\right)}{2}=0\\
&r\cdot\frac{\left(\sigma_{z2}-\sigma_{z1}\right)}{dz}+\frac{\left(\tau_{\theta z2}-\tau_{\theta z1}\right)}{d\theta}+\frac{\left(\tau_{rz2}\cdot r_2-\tau_{r\phi 1}\cdot r_1\right)}{dr}=0 \qquad \textbf{Eq. 6-10}\\
&\frac{\left(\sigma_{r2}\cdot r_2-\sigma_{r1}\cdot r_1\right)}{dr}+r\cdot\frac{\left(\tau_{zr2}-\tau_{zr1}\right)}{dz}+\frac{\left(\tau_{\theta r2}-\tau_{\theta r1}\right)}{d\theta}-\frac{\left(\sigma_{\theta 2}+\sigma_{\theta 1}\right)}{2}=0
\end{aligned}$$

If the dimensions of the element are now reduced to the limit zero, the same equations can be expressed as:

Eq. 6-11

$$\frac{\partial \sigma_\theta}{\partial \theta} + r \cdot \frac{\partial \tau_{r\theta}}{\partial r} + r \cdot \frac{\partial \tau_{z\theta}}{\partial z} + 2 \cdot \tau_{\theta r} = 0$$

$$r \cdot \frac{\partial \sigma_z}{\partial z} + \frac{\partial \tau_{\theta z}}{\partial \theta} + r \cdot \frac{\partial \tau_{rz}}{\partial r} + \tau_{rz} = 0$$

$$r \cdot \frac{\partial \sigma_r}{\partial r} + r \cdot \frac{\partial \tau_{zr}}{\partial z} + \frac{\partial \tau_{\theta r}}{\partial \theta} - \sigma_\theta + \sigma_r = 0$$

Being in general [Timoshenko (1957)]:

Eq. 6-12

$$\frac{\partial [A(r) \cdot r]}{\partial r} = A(r) + \frac{\partial A(r)}{\partial r}$$

Some simplifications are possible because the model can be considered as a solid of revolution deformed symmetrically with respect to an axis of revolution. Therefore the stress components are independent of angle θ and all derivatives with respect to θ vanish. The components of shear stress $\tau_{\theta r}$, $\tau_{r\theta}$, $\tau_{z\theta}$, $\tau_{\theta z}$ also vanish on account of symmetry. Thus, the equation of equilibrium Eq. 6-11 reduces to the new:

Eq. 6-13

$$r \cdot \frac{\partial \sigma_z}{\partial z} + r \cdot \frac{\partial \tau_{rz}}{\partial r} + \tau_{rz} = 0$$

$$r \cdot \frac{\partial \sigma_r}{\partial r} + r \cdot \frac{\partial \tau_{zr}}{\partial z} - \sigma_\theta + \sigma_r = 0$$

The equilibrium of this element has to be assured everywhere within the sample, with respect to the boundary conditions.

The assumptions that are going to be taken about stress trends are valid in the elastic regime. Although they become quite approximate in the plastic regime, it is still assumed to be approximately true.

A first assumption is based on the elementary theory of bending of a plate, namely that linear elements perpendicular to the middle plane of the SP specimen remain straight and normal to the deflection surface of the sample. Hence, all the calculation will be referred to the middle plane. For instance, Figure 6-12 [p.137] shows how the radius r is measured at the inflection point. An important experimental observation is that the contact boundary, so long as no external necking appears, defines at any stage of deformation, the inflection point in the middle plane. Hence, the radius at such a point is designated with r_c

Analysing the shear stress $\tau_{rz} = \tau_{zr}$, this can be simply designated by τ, because it is the only shear component. In the unsupported region, τ can be considered constant. At the clamped edge of the SP specimen, the boundary condition prescribes the shear stress τ as due to the applied load L acting on the surface which is defined by the cylindrical ribbon of the clamped edge of the SP specimen. The value of such a surface can be calculated as $2\pi \cdot a/2 \cdot t_o$, where a is the radius of the receiving hole and t_o the thickness at the clamped perimeter. So:

Eq. 6-14

$$\tau_{\max} = \frac{L}{\pi \cdot a \cdot t_0}$$

The shear stress has been defined as τ_{max} because its distribution along the thickness can be approximately considered as pyramidal, with its maximum value in the middle plane. Thus:

Eq. 6-15

$$\frac{\partial \tau}{\partial z} = \frac{\tau_{\max} \cdot 2}{t_0} = \frac{2 \cdot L}{\pi \cdot a \cdot t_0^{\,2}}$$

where the assumption is made that the thickness along the unsupported region is approximately constant and equal to t_o during the bending phase. As soon as the contact region is considered, τ_{max} has to decrease linearly with the radius r, vanishing finally at the tip of the bulge.

The radial stress σ_r is supposed to have a triangular distribution along the thickness with a zero value in the middle plane and two maximum values σ_r^{max} of opposite sign at the surfaces of the SP sample, which will be respectively in tension and in compression. In the unsupported region, σ_r^{max} is supposed to vary approximately linearly with the radius r, varying from the zero value at the boundary of the contact area (where there is the inflection point) up to the maximum at the perimeter of the clamping ($r = a/2$; tension at the upper side fibres). In the contact region, assume σ_r^{max} is a function of the square of radius r. It will go from the zero value at the boundary of the contact area to another maximum, this time of opposite sign, at the tip of the bulge ($r = 0$; tension in the underside fibres). In the contact region, a relationship for σ_r^{max} , has been assumed of the kind:

Eq. 6-16
$$\sigma_r^{max}\Big|_{r=r_c}^{r=0} = a\cdot r^2 + b\cdot r + c$$

As an even more simplified expression in the unsupported region:

Eq. 6-17
$$\sigma_r^{max}\Big|_{r=a/2}^{r=r_c} = d\cdot r + e$$

Then, anywhere the assumption that $\sigma_r^{max} = \sigma_\theta^{max}$ is valid (Timoshenko, 1957). The unsupported and the contact regions can now be analysed separately. In the unsupported region, from the second component of the equation of equilibrium Eq. 6-13 [p. 112] it is found that:

Eq. 6-18
$$\frac{\partial \sigma_r^{\max}}{\partial r} = \frac{(\sigma_r - \sigma_\theta)}{r} - \frac{\partial \tau}{\partial z} = -\frac{\partial \tau}{\partial z} = -\frac{\tau_{\max} \cdot 2}{t_0}$$

and hence by integration:

Eq. 6-19
$$\sigma_r^{\max} = -\int^{r} \frac{\tau_{\max} \cdot 2}{t_0} \cdot dr = -\frac{\tau_{\max} \cdot 2}{t_0} \cdot r + C$$

valid for $r > r_c$. In addition, because at the inflection point $\sigma_r^{max} = 0$ it is found that:

Eq. 6-20
$$\sigma_r^{\max}\Big|_{r=a/2}^{r=r_c} = \frac{\tau_{\max} \cdot 2}{t_0} \cdot [r_c - r] = \frac{2 \cdot L}{\pi \cdot a \cdot t_0^2} \cdot [r_c - r]$$

which is similar to the Eq. 6-17 [p.114]

In the Eq. 6-16 [p.114] for the contact region, the unknown constants *a, b,* and *c* can be defined by applying three conditions. A first condition is that $\sigma_r^{max} = 0$ at the inflection point. Then, other two conditions are applied to the derivative of the equation:

Eq. 6-21
$$\frac{\partial \sigma_r^{\max}}{\partial r}\Big|_{r=r_c}^{r=0} = 2a \cdot r + b$$

One condition comes from the fact that at the tip of the bulge ($r = 0$), σ_r^{max} has to have its maximum and the final condition comes from fitting the equation of the unsupported region at the contact boundary ($r = r_c$). Resuming, the three conditions are:

Eq. 6-22

$$\sigma_r^{max}\Big|_{r=r_c} = 0$$

$$\frac{\partial \sigma_r^{max}}{\partial r}\Big|_{r=0} = 0$$

$$\frac{\partial \sigma_r^{max}}{\partial r}\Big|_{r=r_c} = -\frac{\tau_{max} \cdot 2}{t_0}$$

From these three conditions, it is found that:

$$a = \frac{\tau_{max}}{t_0 \cdot r_c}; \qquad b = 0; \qquad c = -\frac{\tau_{max} \cdot r_c}{t_0}$$

Hence, the expression for σ_r^{max} in the contact region will be:

Eq. 6-23

$$\sigma_r^{max}\Big|_{r=r_c}^{r=0} = \frac{\tau_{max}}{t_0} \cdot \left[\frac{r^2}{r_c} - r_c\right] = \frac{L}{\pi \cdot a \cdot t_0^{\,2}} \cdot \left[\frac{r^2}{r_c} - r_c\right]$$

6.5.2. Membrane-stretching mode at the contact region

Consider an infinitesimal portion of the small punch disc in the contact region where the portion of the deformed specimen is in contact with the punch ball. Such an element will be defined by the spherical coordinate system (Figure 6-13, p. 137) where the circumferential position is given by the angle θ while the meridian location is given by the contact angle ϕ, and the radial location by the radial coordinate r, which has the zero positioned at the centre of the hemispherical puncher (Figure 6-14, p. 138). Note that this radius coordinate introduced for the contact region is completely different from the radius coordinate defined for modelling the unsupported region. The equilibrium of this element has to be assured everywhere within the sample, with respect to the boundary conditions. The equilibrium of this element is assured if the following equations are accomplished.

- For equilibrium along the circumferential direction:

Eq.6-24

$$(\sigma_{\theta 2}-\sigma_{\theta 1})\cdot rd\phi\cdot dr+(\tau_{\phi\theta 2}-\tau_{\phi\theta 1})\cdot r\sin\phi\cdot d\theta\cdot dr+(\tau_{r\theta 2}\cdot r_2^2-\tau_{r\theta 1}\cdot r_1^2)\cdot\sin\phi\cdot d\theta\cdot d\phi+$$

$$+(\tau_{\theta r1}+\tau_{\theta r2})\cdot rd\phi\cdot dr\cdot\sin\left(\frac{d\theta}{2}\right)=0$$

- For equilibrium along the meridian direction:

Eq.6-25

$$(\sigma_{\phi 2}-\sigma_{\phi 1})\cdot r\sin\phi\cdot d\theta\cdot dr+(\tau_{r\phi 2}\cdot r_2^2-\tau_{r\phi 1}\cdot r_1^2)\cdot\sin\phi\cdot d\theta\cdot d\phi+(\tau_{\theta\phi 2}-\tau_{\theta\phi 1})\cdot rd\phi\cdot dr+$$

$$+(\tau_{\phi r1}+\tau_{\phi r2})\cdot r\sin\phi\cdot d\theta\cdot dr\cdot\sin\left(\frac{d\phi}{2}\right)=0$$

- For equilibrium along the radial direction:

Eq.6-26

$$(\sigma_{r2}\cdot r_2^2-\sigma_{r1}\cdot r_1^2)\cdot\sin\phi\cdot d\theta\cdot d\phi-(\tau_{\theta r2}-\tau_{\theta r1})\cdot rd\phi\cdot dr-(\tau_{\phi r2}-\tau_{\phi r1})\cdot r\sin\phi\cdot d\theta\cdot dr+$$

$$+(\sigma_{\theta 1}+\sigma_{\theta 2})\cdot rd\phi\cdot dt\cdot\sin\left(\frac{d\theta}{2}\right)+(\sigma_{\phi 1}+\sigma_{\phi 2})\cdot r\sin\phi\cdot d\theta\cdot dr\cdot\sin\left(\frac{d\phi}{2}\right)=0$$

Assuming again that the sin of a small angle is equal to the angle itself and dividing the three equations by the expression "r·dϕ·dt·dθ", where *r* can be considered as

Eq. 6-27

$$r=r_1+\frac{(r_2-r_1)}{2}=r_1+\frac{\Delta r}{2}$$

Eq.6-28

$$\frac{(\sigma_{\theta 2}-\sigma_{\theta 1})}{d\theta}+\frac{(\tau_{\phi\theta 2}-\tau_{\phi\theta 1})}{d\phi}\cdot\sin\phi+\frac{(\tau_{r\theta 2}\cdot r_2^2-\tau_{r\theta 1}\cdot r_1^2)}{r\cdot dr}\cdot\sin\phi-\frac{(\tau_{\theta r1}+\tau_{\theta r2})}{2}=0$$

$$\frac{(\sigma_{\phi 2}-\sigma_{\phi 1})}{d\phi}\cdot\sin\phi+\frac{(\tau_{r\phi 2}\cdot r_2^2-\tau_{r\phi 1}\cdot r_1^2)}{r\cdot dr}\cdot\sin\phi+\frac{(\tau_{\theta\phi 2}-\tau_{\theta\phi 1})}{d\theta}-\frac{(\tau_{\phi r1}+\tau_{\phi r2})}{2}\cdot\sin\phi=0$$

$$\frac{(\sigma_{r2}\cdot r_2^2-\sigma_{r1}\cdot r_1^2)}{r\cdot dr}\cdot\sin\phi-\frac{(\tau_{\theta r2}-\tau_{\theta r1})}{d\theta}-\frac{(\tau_{\phi r2}-\tau_{\phi r1})}{d\phi}\cdot\sin\phi+\frac{(\sigma_{\theta 1}+\sigma_{\theta 2})}{2}+\frac{(\sigma_{\phi 1}+\sigma_{\phi 2})}{2}\cdot\sin\phi=0$$

If the dimension of the element are again reduced, to the limit zero, considering that:

Eq. 6-29

$$\lim_{\Delta r\to 0}\left(\frac{r_2^2}{r}\right)=\lim_{\Delta r\to 0}\left[\frac{(r_1+\Delta r)^2}{r_1+\Delta r/2}\right]=r_2$$

applying theEq. 6-12 [p.112] then the Eq.6-28 become:

Eq. 6-30

$$\frac{\partial\sigma_\theta}{\partial\theta}+\frac{\partial\tau_{\phi\theta}}{\partial\phi}\cdot\sin\phi+\frac{\partial\tau_{r\theta}}{\partial r}\cdot r\sin\phi-\tau_{\theta r}+\tau_{r\theta}\cdot\sin\phi=0$$

$$\frac{\partial\sigma_\phi}{\partial\phi}\cdot\sin\phi+\frac{\partial\tau_{r\phi}}{\partial r}\cdot r\sin\phi+\frac{\partial\tau_{\theta\phi}}{\partial\theta}-\tau_{\phi r}\cdot\sin\phi+\tau_{r\phi}\cdot\sin\phi=0$$

$$\frac{\partial\sigma_r}{\partial r}\cdot r\sin\phi-\frac{\partial\tau_{\theta r}}{\partial\theta}-\frac{\partial\tau_{\phi r}}{\partial\phi}\cdot\sin\phi+\sigma_\theta+\sigma_\phi\cdot\sin\phi+\sigma_r\cdot\sin\phi=0$$

Again, some simplificationsare possible because the model can be considered as a solid of revolution deformed symmetrically with respect to an axis of revolution. Therefore, the stress components are independent of angle θ and all derivatives with respect to θ vanish. The component of shearing stress $\tau_{\theta r}$, $\tau_{r\theta}$, $\tau_{\phi\theta}$, $\tau_{\theta\phi}$ also vanish on account of symmetry. Thus, the equation of equilibrium reduces to:

Eq. 6-31

$$\frac{\partial\sigma_\phi}{\partial\phi}+\frac{\partial\tau_{r\phi}}{\partial r}\cdot r=0$$

$$\frac{\partial\sigma_r}{\partial r}\cdot r\sin\phi-\frac{\partial\tau_{\phi r}}{\partial\phi}\cdot\sin\phi+\sigma_\theta+\sigma_\phi\cdot\sin\phi+\sigma_r\cdot\sin\phi=0$$

Note that, ideally at the tip of the bulge, the two tensions σ_θ and σ_ϕ must be the same for a matter of equilibrium and eventually, this state of balanced biaxial tension is assumed to be everywhere in the deformed sample $(\sigma_\theta = \sigma_\phi = \sigma)$. Furthermore, other assumptions can be made considering the boundary conditions. On the contact surface, defined by $r = R$ acts the load L, which is resulting in a pressure for each unit of surface. This pressure can be determined assuming the load distributed on the hemispherical contact surface:

Eq. 6-32

$$p=\frac{L}{2\pi\cdot R^2\cdot(1-\cos\phi_c)}$$

which can be divided in the two components, along the radial direction (p_r) and the tangential direction (p_{tg}).

Eq. 6-33

$$p_r=\frac{L}{2\pi\cdot R^2\cdot(1-\cos\phi_c)}\cdot\cos\phi$$

Eq. 6-34

$$p_{tg}=\frac{L}{2\pi\cdot R^2\cdot(1-\cos\phi_c)}\cdot\sin\phi$$

The radial external force (p_r) compresses the specimen and the distribution of the induced compression stress (σ_r) through the thickness, is assumed to be approximately triangular. Hence, the maximum value of σ_r will be at the contact surface and equal to

p_r, diminishing constantly through the thickness and disappearing at the surface. Thus, it is assumed that:

Eq. 6-35
$$\left.\frac{\partial\sigma_r}{\partial r}\right|_{r=R}^{r=R+t_\phi} = -\frac{p_r}{t_\phi} = -\frac{L\cdot\cos\phi}{2\pi\cdot R^2\cdot(1-\cos\phi_c)\cdot t_\phi}$$

And integrating between R and $R + t_\phi$ the expression for σ_r is obtained:

Eq. 6-36
$$\sigma_r = p_r\cdot\left(1-\frac{t}{t_\phi}\right) = \frac{L\cdot\cos\phi}{2\pi\cdot R^2\cdot(1-\cos\phi_c)}\cdot\left(1-\frac{t}{t_\phi}\right)$$

where t_ϕ is the thickness at the given contact angle ϕ (Figure 6-15, p.139).

The tangential component of load (p_{tg}) will determine the shear component ($\tau_{\phi r}$ and $\tau_{r\phi}$) in the SP sample, which is depending on the friction coefficient f due to the contact between the puncher and the sample. Such shear stress will have an approximate triangular distribution, so the maximum value of $\tau_{\phi r} = \tau_{r\phi} = \tau$ will be at the contact surface

Eq. 6-37
$$\tau = f\cdot p_{tg}$$

diminishing constantly through the thickness and disappearing at the surface. The friction coefficient f will be a number in the range $0 < f \leq 1$. However, for the chosen range of SP creep test temperatures, the two materials involved in the contact (nickel alloy for the puncher and the low alloy ferritic steel for the tested material) are expected to be represented by a friction coefficient f, which should be around 0.8 [Maile, (1998)].

Then, the distribution of such shear stress through the thickness will be defined by:

Eq. 6-38
$$\frac{\partial \tau}{\partial r}\bigg|_{\substack{r=R \\ r=R+t_\phi}} = -f \cdot \frac{p_{tg}}{t_\phi} = -f \cdot \frac{L \cdot \sin\phi}{2\pi \cdot R^2 \cdot (1-\cos\phi_c) \cdot t_\phi}$$

The $\frac{\partial \tau_{\phi r}}{\partial \phi}$ in the Eq. 6-31, which is reducing to $\frac{\partial \tau}{\partial \phi}$, is obtained by derivation of Eq. 6-37 with respect to ϕ:

Eq. 6-39
$$\frac{\partial \tau}{\partial \phi} = f \cdot \frac{\partial p_{tg}}{\partial \phi} = f \cdot \frac{L}{2\pi \cdot R^2 \cdot (1-\cos\phi_c)} \cdot \cos\phi \text{ (equals } f{\cdot}p_r\text{)}$$

Now, the reduced version of equations Eq. 6-31 [p. 119] becomes:

Eq. 6-40
$$\begin{gathered} \frac{\partial \sigma}{\partial \phi} + \frac{\partial \tau}{\partial r} \cdot r = 0 \\ \frac{\partial \sigma_r}{\partial r} \cdot r \sin\phi - \frac{\partial \tau}{\partial \phi} \cdot \sin\phi + \sigma \cdot (1+\sin\phi) + \sigma_r \cdot \sin\phi = 0 \end{gathered}$$

Considering the second component of this equation (Eq. 6-40) and assuming r only for the portion of material of the SP specimen ($R<r< R + t_\phi$) or ($R+t$) and substituting the Eq. 6-35, Eq. 6-36 and Eq. 6-39 it becomes:

Eq.6-41:
$$-\frac{p_r}{t_\phi} \cdot (R+t) \cdot \sin\phi - f \cdot p_r \cdot \sin\phi + \sigma \cdot (1+\sin\phi) + p_r \cdot \left(1 + \frac{t}{t_\phi}\right) \cdot \sin\phi = 0$$

and then:

Eq. 6-42
$$\sigma = \frac{L \cdot \cos\phi \cdot \sin\phi}{2\pi \cdot R^2 \cdot (1-\cos\phi_c) \cdot (1+\sin\phi)} \cdot \left(\frac{R}{t_\phi} + f + 2 \cdot \frac{t}{t_\phi} - 1\right)$$

The first component of the equation of equilibrium (Eq. 6-40) is a second order equation and unfortunately, for the simplification that has been made, cannot be easily verified. In fact, the distribution of the shear stress τ (Eq. 6 -38), in reality, is not perfectly triangular through the thickness of the SP sample and may be also slightly depending on the angle ϕ. Thus, the partial derivate of equation Eq. 6-42 of the stress σ with respect to the angle ϕ ($\frac{\partial\sigma}{\partial\phi}$) cannot be directly equated to the expression $-\frac{\partial\tau}{\partial r}\cdot r$ with $\frac{\partial\tau}{\partial r}$ coming from the simplifiedEq. 6-38.

Resuming, the equation Eq. 6-42 is the expression for both the meridian and the circumferential stress. The other components defining the stress state during the membrane-stretching phase in the contact region are σ_r and τ. Remember that the compressive radial stress σ_r has an approximate triangular distribution through the thickness with the maximum value at the contact (t = 0) and zero value at the surface as appears in the Eq. 6-36 [p.120]. Finally, The shear stress τ has also an approximate triangular distribution through the thickness with maximum value at the contact (t = 0) and zero value at the surface (t = t_ϕ) as appears in the Eq. 6-38, [p. 121], and consequently the shear stress τ will be expressed by:

Eq. 6-43

$$\tau = f \cdot \frac{L \cdot \sin\phi}{2\pi \cdot R^2 \cdot (1-\cos\phi_c)} \cdot \left(1 - \frac{t}{t_\phi}\right)$$

The reliabilityof these relationships can be assessed by experimental data from both creep and tensile SP techniques.

6.5.3. Membrane stretching mode at the unsupported region.

Assume, first of all, that the membrane stretching mode also applies in the unsupported region. For modeling such an area, it is better to refer to the equation of equilibrium already presented when the bending mode was introduced:

Eq. 6-44

$$\begin{gathered} r\cdot\frac{\partial\sigma_z}{\partial z}+r\cdot\frac{\partial\tau_{rz}}{\partial r}+\tau_{rz}=0 \\ r\cdot\frac{\partial\sigma_r}{\partial r}+r\cdot\frac{\partial\tau_{zr}}{\partial z}-\sigma_\theta+\sigma_r=0 \end{gathered}$$

Also, the variation of τ along z is the same, so:

Eq. 6-45

$$\frac{\partial\tau}{\partial z}=\frac{\tau_{\max}\cdot 2}{t_0}=\frac{2\cdot L}{\pi\cdot a\cdot t_0^{\ 2}}$$

In this case, σ_r has to have a uniform distribution along z and $\sigma_r = \sigma_\theta$ is valid all along the unsupported region. It is important now to define in more detail the unsupported region, looking also at the shape assumed by the specimen during such an evolved situation when the membrane mode is on. The unsupported region is the area characterised by a negative curvature opposite to the one at the contact region. Hence, it starts from the inflection points of any fibres all through the thickness up to the clamping zone at the border of the specimen. If there is external necking, then such a distribution can be more complex. This is usual in the SP creep tests. To understand this, it can be useful to map the location of the inflection points for any fibres through the thickness of the SP sample. In this case, from the second expression of the system of Eq. 6-44, p. 123:

Eq. 6-46
$$\frac{\partial \sigma_r}{\partial r} = -\frac{\partial \tau}{\partial z} = -\frac{\tau_{\max} \cdot 2}{t_0}$$

Hence, the value of σ_r can be calculated by integrating such expression:

Eq. 6-47
$$\sigma_r = -\frac{\tau_{\max} \cdot 2}{t_0} \cdot r + C$$

The unknown constant C can be found by knowing that, for any fibres at the inflection point, the stress has to be the same as was calculated by the earlier model of the contact region: σ_{cal}. Consequently,

Eq. 6-48
$$\sigma_r\Big|_{r>r_c} = -\frac{\tau_{\max} \cdot 2}{t_0} \cdot (r - r_c) + \sigma_{cal} = \frac{2 \cdot L}{\pi \cdot a \cdot t_0^{\,2}} \cdot (r_c - r) + \sigma_{cal}$$

6.6. Analytical model for strain

As has been detailed in the definition of the stress model, the portion of sample in which the model should describe the behaviour of the material is the one where the failure will take place. Then, the evolution of strain in such an area will follow the same steps taken for the stress model. Thus, at the first stages of the bending phase, the strain evolves in the elastic field but later, once the yield point is reached, it becomes a plastic strain. Next, in the membrane-stretching phase, the strain will be kept in the plastic regime.

6.6.1. Strain evolution in the membrane stretching phase

The meridian and the circumferential strain are the same ($\varepsilon_\phi = \varepsilon_\theta$) and their addition gives the radial strain, because of the incompressible plastic deformation [Chakrabarty (1970), Byun (2001)].

Eq. 6-49
$$\varepsilon_{\phi}+\varepsilon_{\theta}=\varepsilon_{r}=\varepsilon$$

In a regime of large plastic deformation, the strain component can be written as [Hill (1950)]:

Eq. 6-50
$$\varepsilon=\int_{\delta l}^{\delta l'}\frac{d(\delta l')}{\delta l'}=\ln\left(\frac{\delta l'}{\delta l}\right)$$

where δl is a linear element.

If the state of deformation is homogeneous (displacement as linear function of the body coordinate), the element base δl can be considered as the whole dimension. The radial strain is then directly linked with the thickness reduction and is given in the general form:

Eq. 6-51
$$\varepsilon=\ln\left(\frac{t_0}{t}\right)=\frac{\varepsilon_{\phi}}{2}=\frac{\varepsilon_{\theta}}{2}$$

This is just an alternative way to calculate the strain, which can also be represented by the traditional expression in the percentage form:

Eq. 6-52
$$\varepsilon(\%)=\left(\frac{t_0-t}{t_0}\right)\cdot 100$$

Next, when the strain for SP tests will be mentioned, it will be always expressed in the logarithmic form unless differently specified.

6.7. Precaution in using the model

An uncertainty in applying such a model is due to the elastic components of deformation. Unfortunately, when the tests are interrupted, the elastic component of deformation is recovered. Then, the geometrical features that are observed in the SP specimen after being interrupted are only referring to the plastic component of deformation. Obviously, in the SP tensile tests, the elastic component is expected to be an integral part of the deformation, while generally in the SP creep tests the elastic component is only a very small percentage of the total deformation. Hence, according to the type of SP test, the elastic component of deformation should be quantified and conveniently considered in the stress and strain model.

6.8. Conclusion of the model presentation

This model is based in looking for the equilibrium for the SP specimen at the given boundary conditions. Two stress conditions were considered, the bending mode and the membrane stretching mode. The model referring to the bending mode is working properly only in the elastic regime, but with the appropriate assumption it was adapted to the plastic regime. However, the most relevant outcome, of such a mathematical exercise, was the model referring to the membrane stretching mode, which will be employed in practically all the calculations.

Because of the different stress states acting within the SP specimen, the model was considered separately for the contact region and for the unsupported region, where the compression and the possible shear stress components are missing. Finally, the stress continuity between those two regions was assured.

In the next chapters the main outcome of these models will be employed and their success evaluated.

6.9. *Figures - presentation of the model*

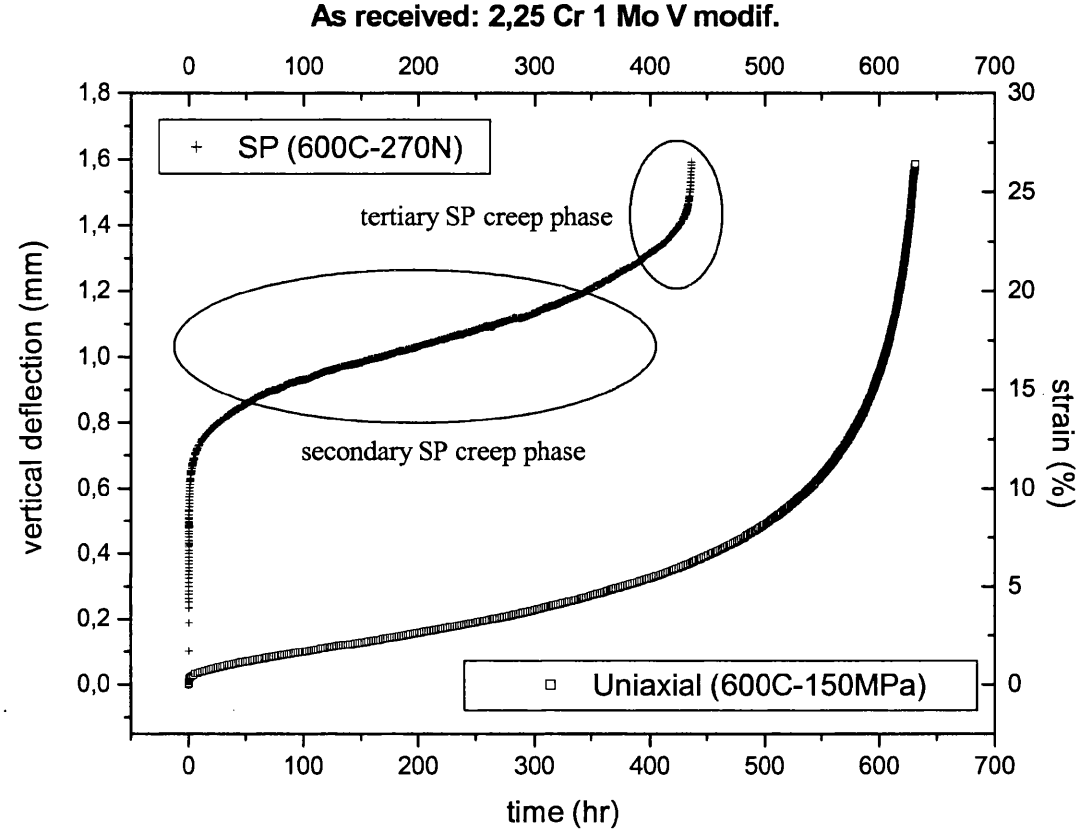

Figure 6-1: Typical SP creep curve compared with the uniaxial creep curve obtained on the same material at the same temperature and with similar rupture life.

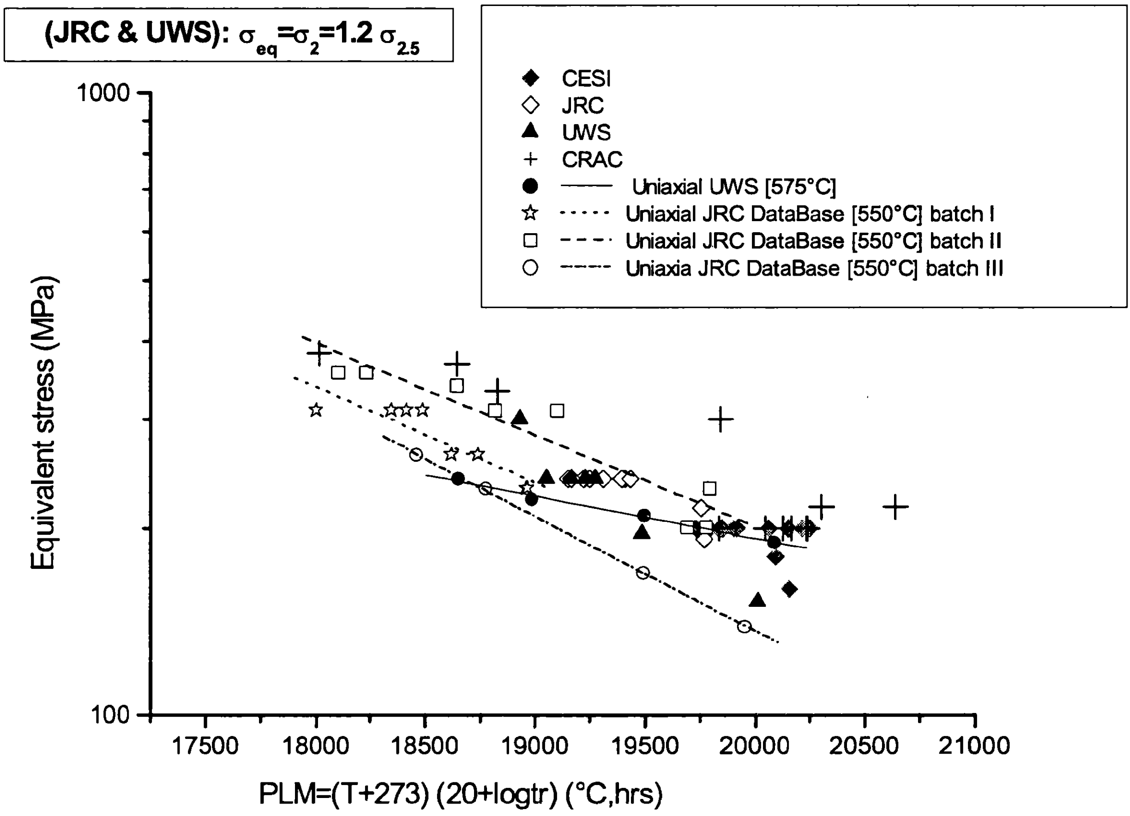

Figure 6-2: The full set of SP round robin results and the uniaxial creep test results in a Larson-Miller parametric representation

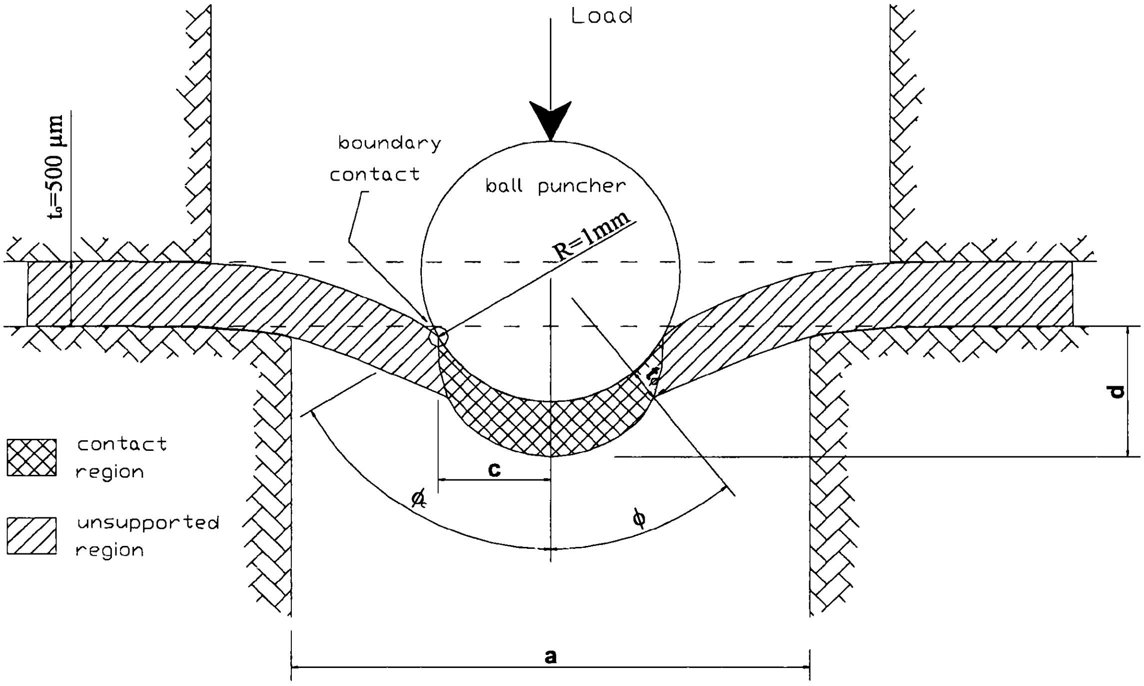

Figure 6-3: Sketch of a typical deformed SP creep specimen (interrupted test HM3-09).

Figure 6-4: Next page - Cross section of the interrupt test HM3-09 (50 % creep life)

puncher

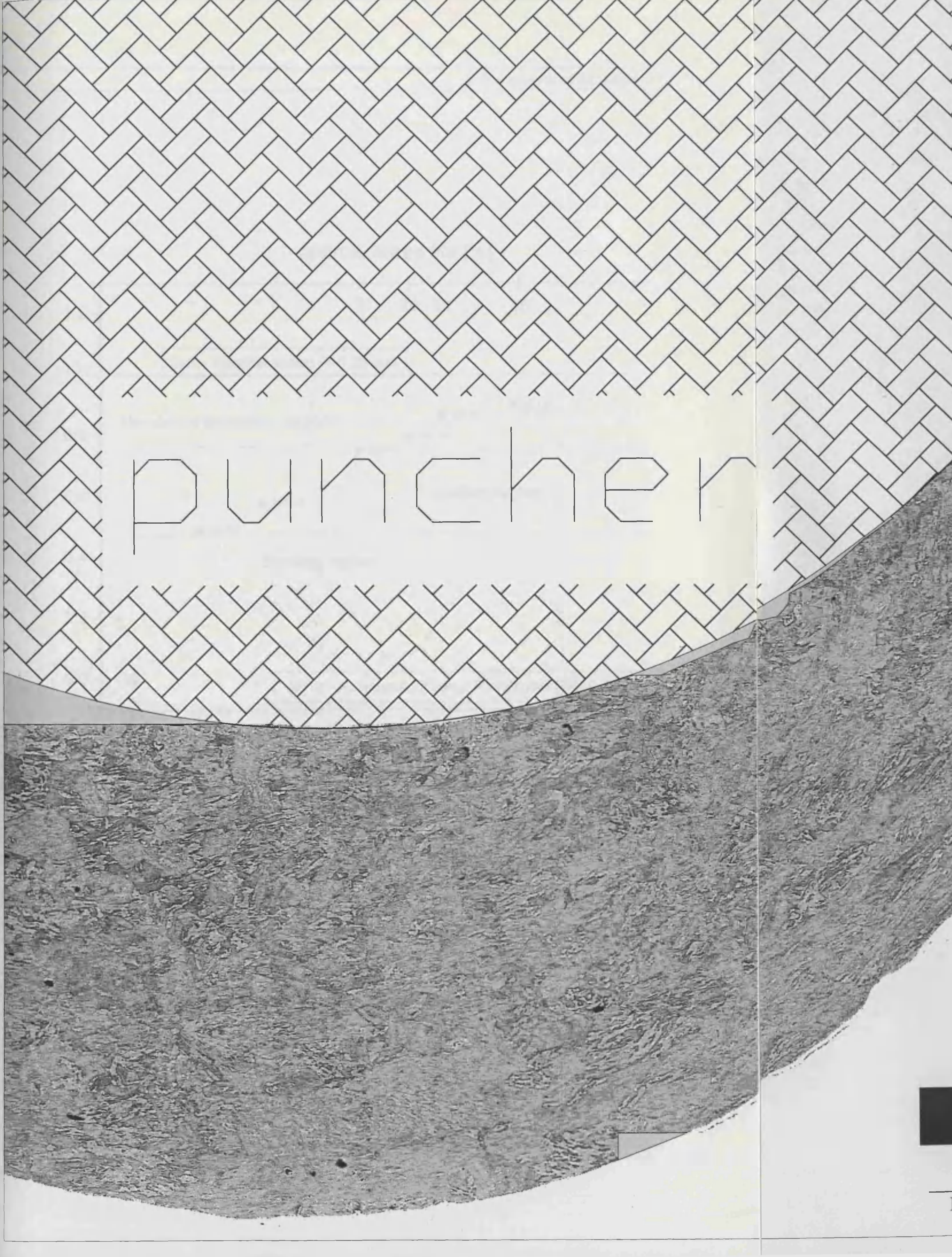

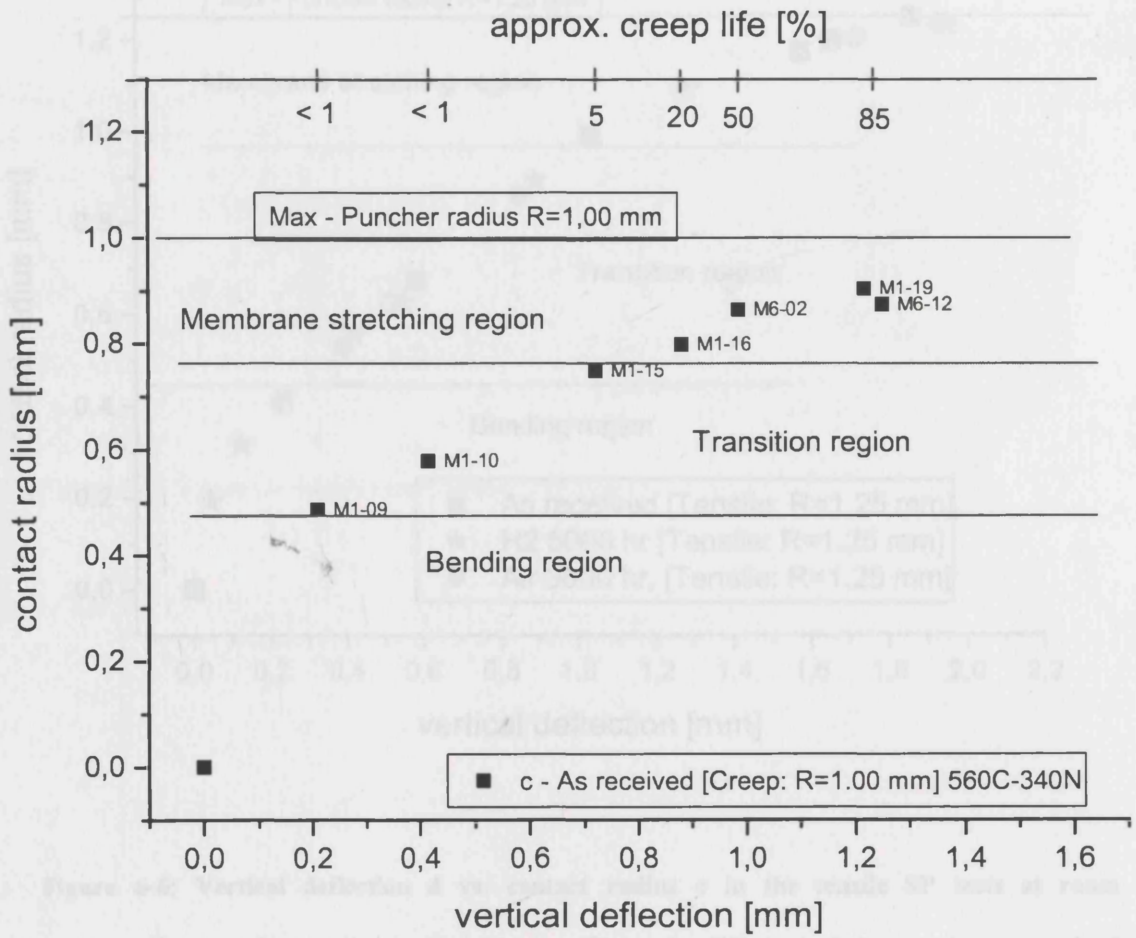

Figure 6-5: Vertical deflection d vs. contact radius c for the as received material at the load of 340N and temperature of 560°C. The puncher radius is R=1,00 mm. Approximate indication in % of creep life.

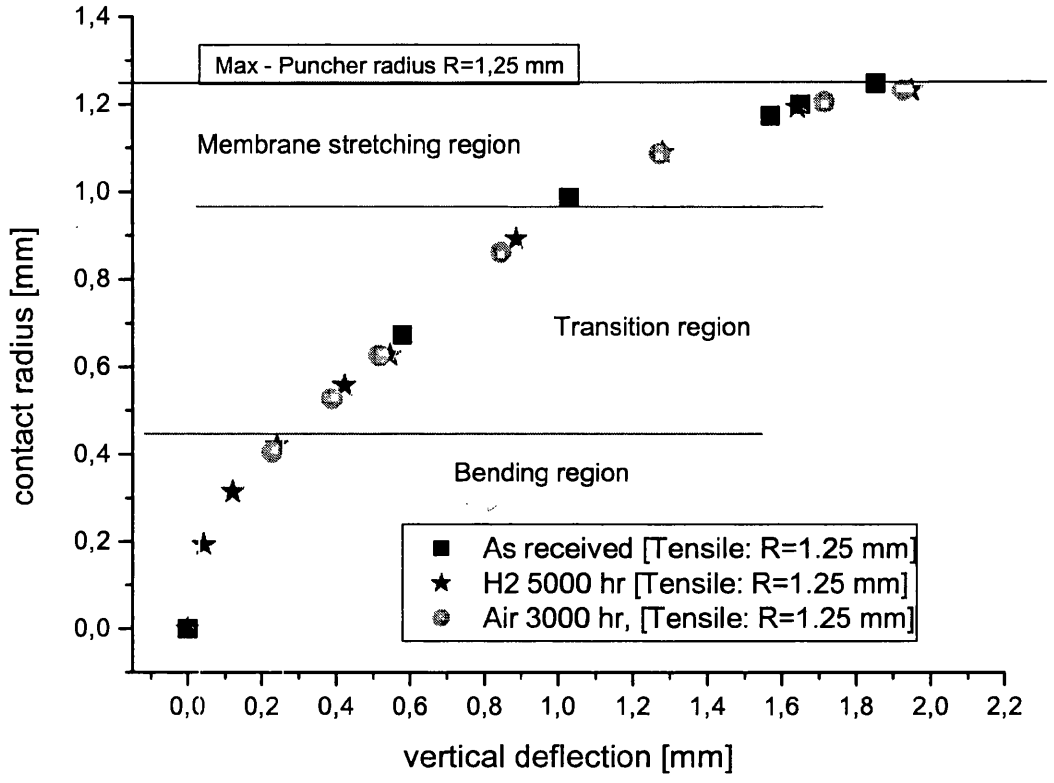

Figure 6-6: Vertical deflection d vs. contact radius c in the tensile SP tests at room temperature. The puncher radius is R=1,25 mm. The only difference between the as received material and the damaged material is at the end of the test where the damaged material at room temperature seems to fail at higher vertical deflection.

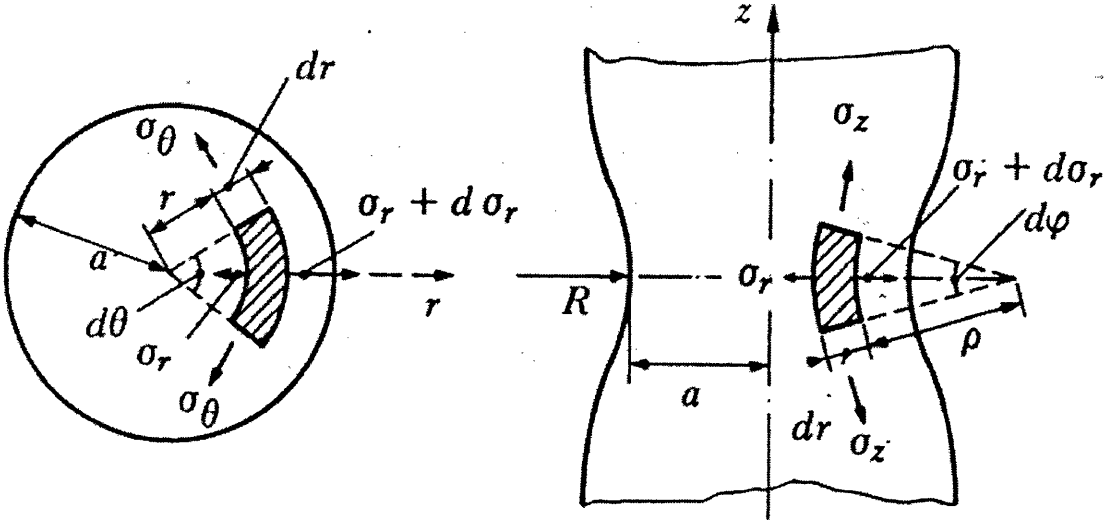

Figure 6-7: Model for the uniaxial necking [Bridgman (1944)].

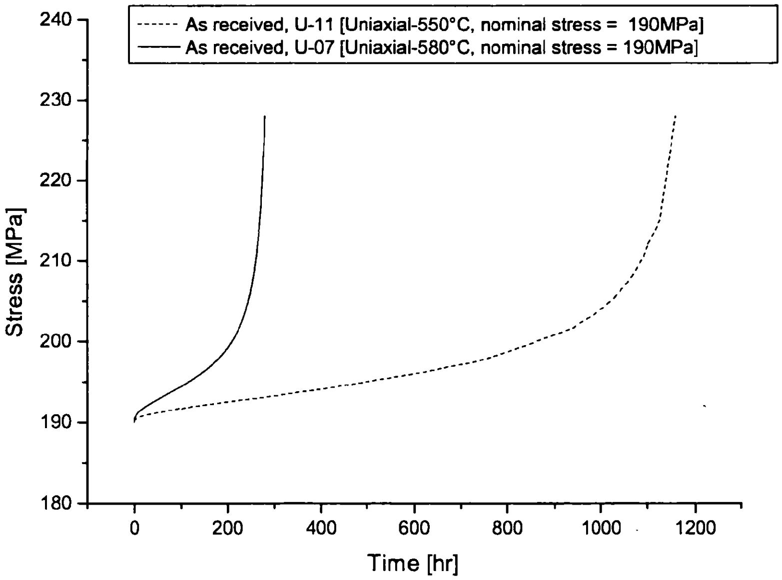

Figure 6-8: Evolution of real stress in uniaxial creep tests (tests: U-11, U-07).

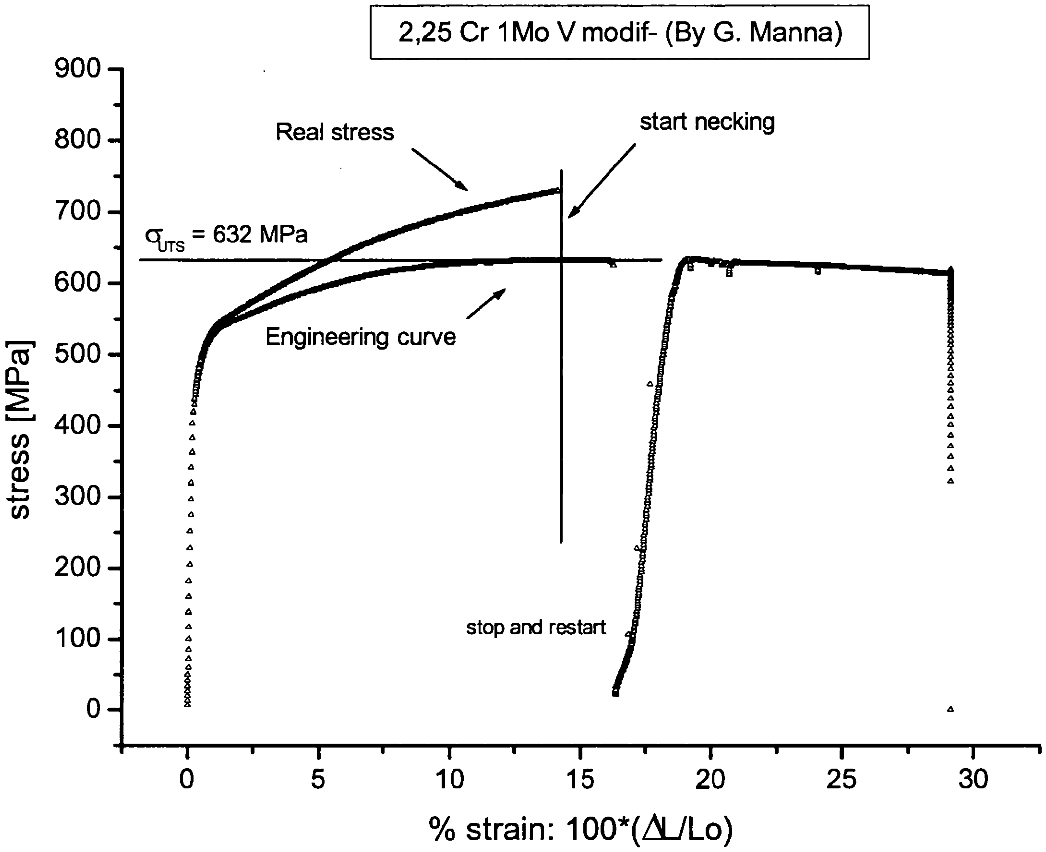

Figure 6-9: Uniaxial tensile test

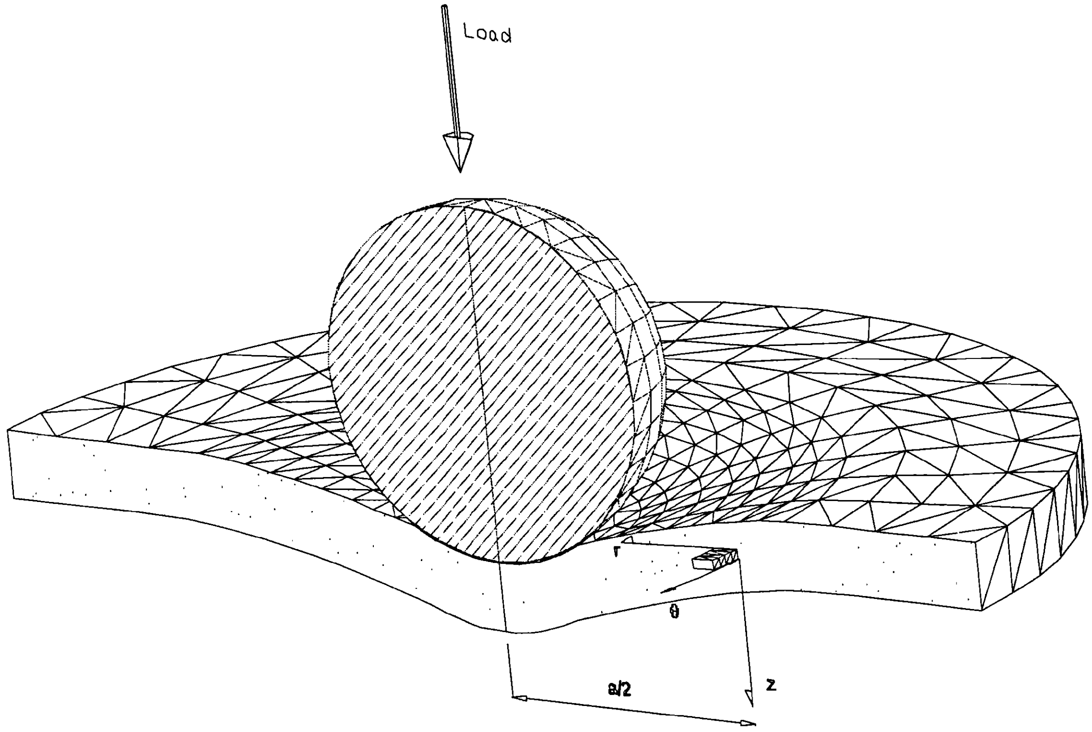

Figure 6-10: Sketch of the tensile SP sample (M6-20) close to the end of the bending phase, with the infinitesimal element and the coordinate system.

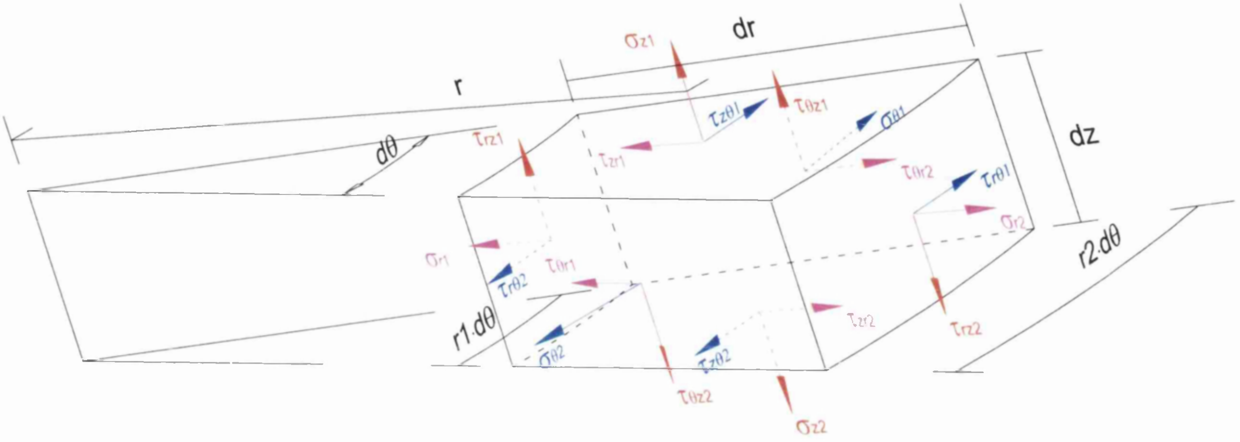

Figure 6-11: Detail of an infinitesimal element of the SP sample in the unsupported region

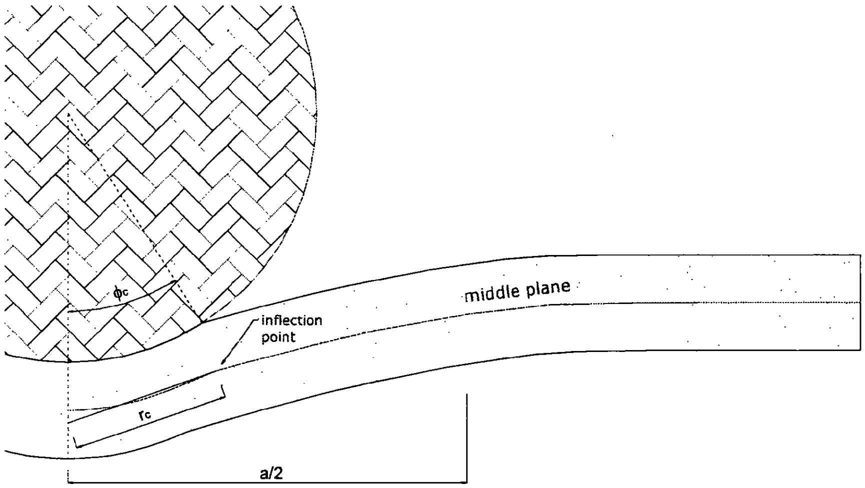

Figure 6-12: Details of the middle plane deformation and definition of radius *r* (M6-20)

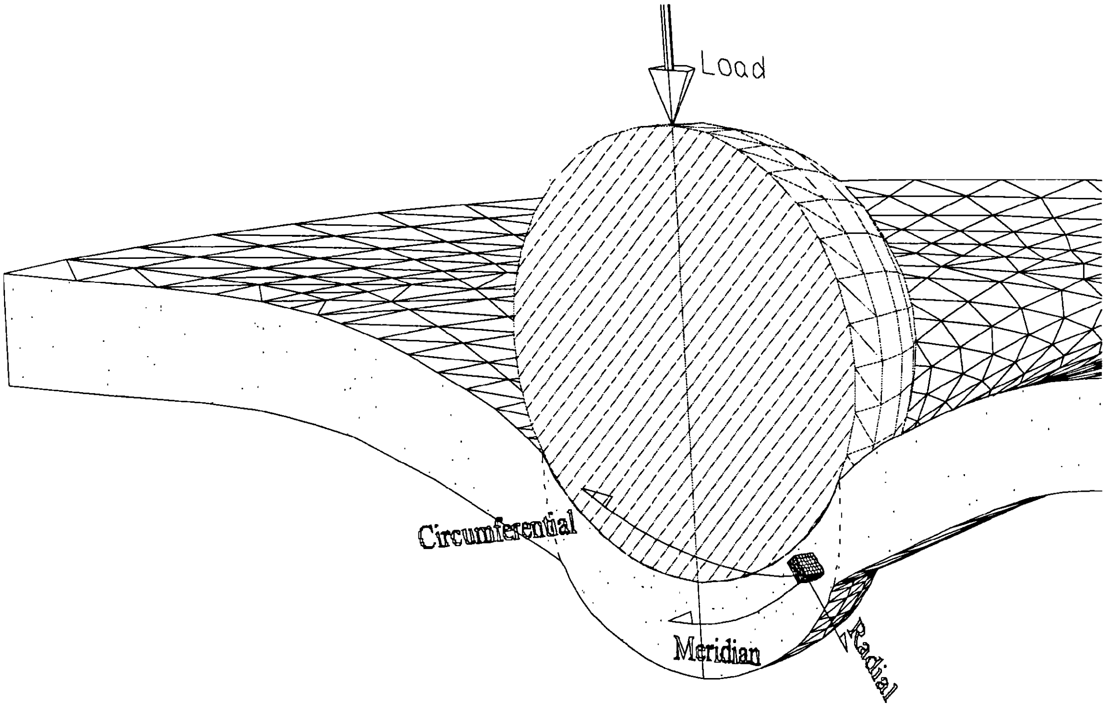

Figure 6-13: Sketch of the SP creep sample (HM3-09) with the main direction and the infinitesimal element.

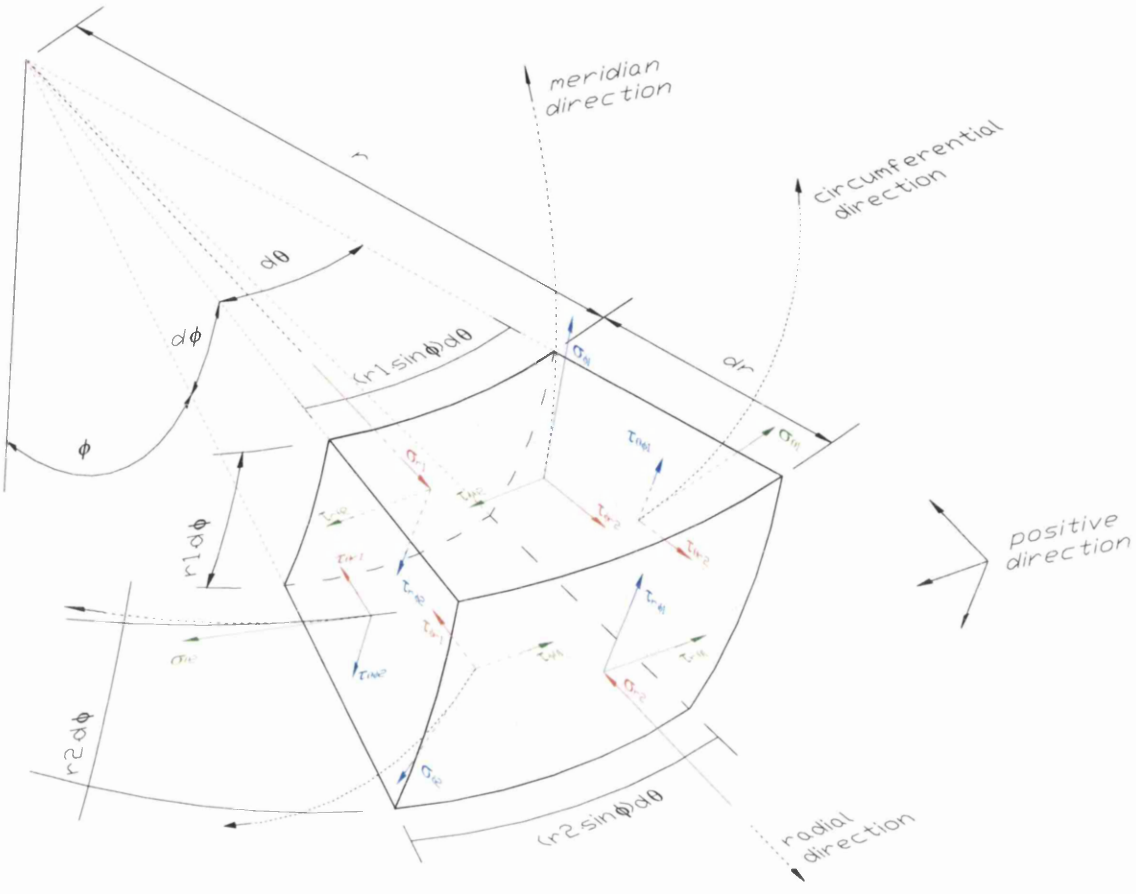

Figure 6-14: Infinitesimal element of the SP sample at the contact region (spherical shape) in polar coordinate

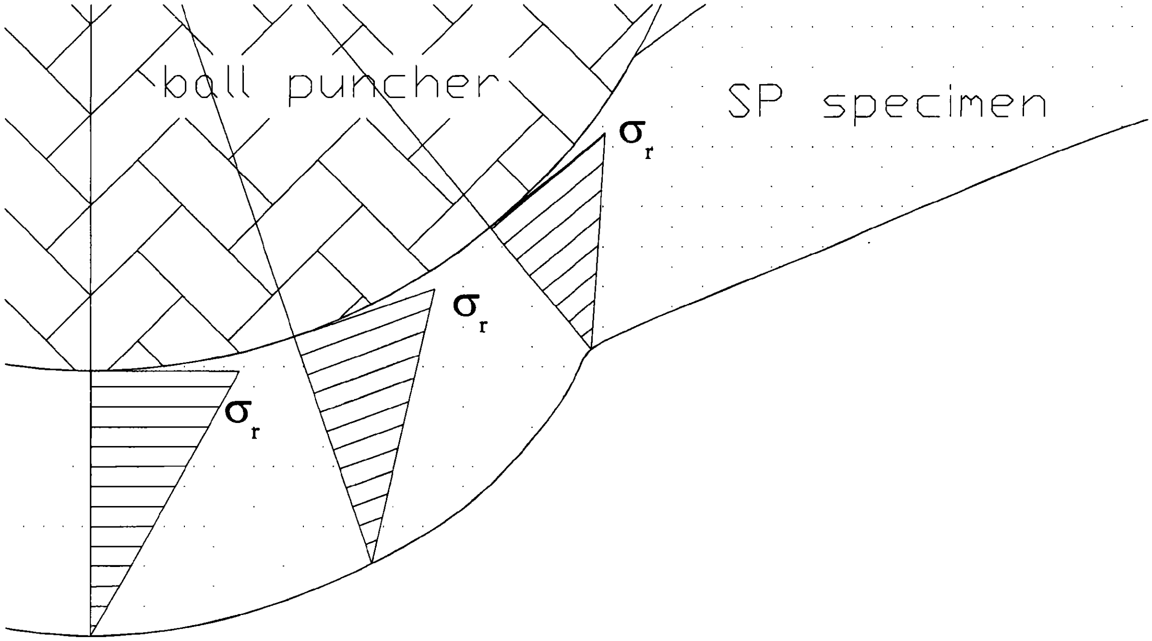

Figure 6-15: radial stress at different location for a typical SP creep sample.

7. Discussion

In this chapter, several pieces of evidence will be brought in favour of the SP technique as a useful tool for plant integrity assessment. First, the proposed stress-strain model will be validated, comparing the SP creep results with the conventional uniaxial creep outcome for the as-received material. Then, such a model will be used to assess the potential and the sensitivity of the SP technique for evaluating the degree of damage in the aged material, with special emphasis on hydrogen-aged material. Finally, a short analysis will be made of the potential of the SP tensile technique.

7.1. SP creep technique

In the last chapter (Chap. 6) a qualitative description has been given about the way the SP specimen is deforming during a test. Based on this information, an analytical stress-strain model was proposed. This model will now be applied to the "as-received material" for describing the evolution of stress and strain in the SP specimen. Some interrupted tests will be analysed, implementing the proposed model, and the outcome will be used to map the evolution of stress and strain within the SP specimen. The validation of the proposed model will be achieved by comparing the calculated stress and strain state for the SP specimen with the equivalent stress and strain state found on the same material tested at the same condition but on the conventional uniaxial standard specimen. It will also be taken into account that, in the SP specimen, the load is applied by contact. This interacts directly with the ductility of material, while introducing a multiaxial state of stress and could lead to some different behaviour patterns. The discussion will be based mainly on the results obtained from the SP creep tests. The SP tensile testing technique will be considered separately.

7.1.1. SP creep stress evolution.

As detailed during presentation of the analytical model, the portion of sample in which the model should describe the behaviour of the material is the one where the failure will eventually take place. In the SP creep tests, this happens along an annular area where initially the thickness reduces due to the necking phenomenon, before crack propagation further reduces the area sustaining the applied load. (Figure 7-1, p. 170).

Before proceeding to the evaluation of the state of stress and strain within the SP creep specimen, it is worth resuming the state of the art. The SP specimen during the test is clearly subject to a multiaxial state of stress, but at the same time, the results reported in the literature [Parker (1998)] and the results of this research show that the mechanism of creep and the rate determining creep damage process (represented by the Norton-Arrenhius relationship) are similar in both SP and uniaxial techniques. Therefore, testing the same material with both techniques at the same temperature, the SP load resulting in the same time of failure is expected to lead to values of stress comparable with the stress of the equivalent uniaxial test. Other work [Hayhurst (1983)] suggests that the criterion for creep failure would be better related to the maximum principal stress, instead of either the Tresca or Von Mises criteria (effective stress). This work was performed on three classes of material: aluminium, copper and stainless steel. Furthermore, other work by Cane (1981), who was analysing the multiaxial creep behaviour of 2.25Cr-1Mo alloy steel, concluded that at relatively low effective stress it is mainly the principal stress which drives the whole creep process.

All this evidence leads to the supposition that the membrane stress in the SP specimen should be comparable with the stress in the uniaxial specimen tested at the same temperature and with a similar rupture life. Once the proposed model will give such a response, it will be considered as an important step for the validation of the model itself.

In order to follow the evolution of stress and strain within the SP creep specimen, a series of interrupted tests at different stages of the sample creep life were run. The interruptions were chosen to consider specific phases of the SP creep test. Thus, some of the tests were interrupted around the transition between the primary to the secondary creep phase, while others were interrupted during the secondary creep phase. Finally, some tests were interrupted close to the failure of the specimen, further in the tertiary creep phase. Then, the geometrical features (Figure 6-3, p. 129), such as the thickness t_{ϕ} at different angles ϕ and the contact angle ϕ_c, can be measured and the state of stress and strain for each of those samples can be defined. It is considered that the elastic components of deformation in creep tests are normally very small. The recovered elastic part is recorded at the end of an interrupted test as a reduction of the vertical deflection. This reduction is of the order of 10-20 μm, which represents about 2 % of the total deflection. Then, the geometrical features measured on the interrupted SP creep sample will be not very different from those present during the test. Consequently, all the calculated stresses and strains will be slightly smaller than the operating one.

In order to track the SP creep stress-strain evolution, it is meaningful to employ the ordinary plot vertical deflection against time, which is representing the material behaviour at the given condition of temperature and load. In this plot, the different creep phases can be well identified (Figure 6-1, p. 127). At each instant, such a plot is the result of the combination and evolution of the state of stress and strain in the whole SP specimen. As mentioned in the previous chapter, the vertical deflection is in some way linked to other geometrical features of the SP specimen. These links are extremely important because they can provide information about the creep properties of the material. In fact, these other geometrical parameters intervene in one way or another in the calculation of stress and strain and it can be helpful to follow the way they may change during the SP creep test. Here are reported the main formulae emerging from the membrane stretching model. First, the membrane stress at the external side of the specimen in the contact region (Figure 6-3, p. 129):

Eq. 7-1:

$$\sigma_c = \frac{L \cdot \cos\phi \cdot \sin\phi}{2\pi \cdot R^2 \cdot (1-\cos\phi_c) \cdot (1+\sin\phi)} \cdot \left(\frac{R}{t_\phi} + f + 1 \right)$$

Also, the strain along the radial (Figure 6-12, p. 137) direction which is:

Eq. 7-2

$$\varepsilon = \ln\left({}^{t_0}\!\!\diagup_{t_\phi} \right)$$

while in the unsupported region σ_u, can be calculated looking at the radial (unsupported model) distances of the considered point (r) and at the radial distance of the point where the σ_c was calculated (r_c):

Eq. 7-3

$$\sigma_u = \frac{2L}{\pi \cdot a \cdot t_0} \cdot (r_c - r) + \sigma_c$$

The Eq. 7-1 shows that the membrane stress is strongly influenced by the contact angle, while the minimum thickness, and mainly the angle ϕ have less importance. For instance, considering the typical values that those geometrical parameters have around the secondary creep phase, a variation of 10 % in the contact angle will lead to a change in the calculated stress of 17 %, while the same variation of the thickness t_ϕ leads to a change of only 6 %. Lastly, the least sensitive factor is the angle ϕ, where even a variation of 10% gives a negligible effect on the calculated stress (< 1%). Eq. 7-3 shows a decreasing stress when considering points far from the neck in the unsupported region.

A first important link is the one between the vertical deflection and the thinning of the sample, which is expressed by the strain. (Figure 7-2, p. 171). The relationship is empirically found, based on measurements from the interrupted tests and can be expressed by:

Eq. 7-4

$$\varepsilon = \ln\left(\frac{t_0}{t}\right) = A \cdot e^{Bd}$$

where d is the vertical deflection and the numerical constants are A = 0,0429 and B= 2,51. This relationship is observed to be valid whichever conditions of temperature and load were chosen for the creep test, and whatever degree and kind of material ageing was chosen. Furthermore, it is remarkable how the points coming from the SP creep interrupted tests are fitting with an equivalent plot (vertical deflection vs. strain) presented by Mao (1987) in which tensile tests (with very different conditions compared to creep) were run on several steels by a SP equipment provided with a puncher of radius 1,00 mm (Figure 2-7, p. 46). Hence, as mentioned in the work of Yang (2003), the vertical deflection can be treated exactly as the elongation is treated in the standard uniaxial test technique and then directly linked to the strain.

There is a second link between the angle pointing out the thinnest section (ϕ) and the value of the minimum thickness itself (Figure 7-3, p. 172). Between them exists a linear relationship which shows that a decreasing thickness t_ϕ always corresponds to an increase of the angle ϕ. In this plot are represented the interrupted tests referring to the set at 340N and 560°C, and the set at 270N and 600°C, both on the as-received material

Another important plot is the one which links the vertical deflection *d* with the contact radius *c*. This plot has been already introduced in the last chapter (Figure 6-5, p. 131) because it clearly shows how the deformation mode is switching from bending to membrane stretching in the SP creep tests [Komazai (2000)]. Remember that the vertical deflection, which is related to the thickness, and the contact radius are both involved with different weight in the calculation of the membrane stress. In this plot, only data coming from interrupted tests run at one set of temperature and load (340N, and 560°C) were included, but the next questions concerns how this plot could change with different sets of load and temperature, and what will influence the membrane stress? When the load or the temperature is increased, the creep life is expected to drop and the creep ductility is expected to increase. The drop in creep life is forcing the shift from the primary to the secondary creep phase at higher vertical deflection (Figure 7-4, p. 173; Figure 7-5, p. 173). This means that, for a shorter creep life, the switching tends to occur at smaller values of the minimum thickness (Figure 7-2, p. 171). Furthermore, it is well known from general creep theory that, for increasing stress and temperature, the creep ductility measured in the conventional uniaxial creep test by the strain at rupture and by the reduction of area is generally increasing (Cane 1981, Greenwood 1973). In the SP test, the increase in creep ductility is expected to increase the contact radius. This is quite evident if one considers the contact features between a completely rigid sphere and a plate made of two materials with different stiffness. In this case, the more ductile material will tend to have larger contact with the sphere. However, looking at the uniaxial results (Figure 7-13, p. 179) at least in the range of stress chosen for the current project, this material does not show appreciable changes in creep ductility. Unfortunately, there was not enough time to run interrupted tests at different sets of load and temperature (apart from the three tests at 270N and 600°C, with an expected similar creep ductility and comparable creep life). However, it was assumed that in the range of temperature and load adopted in this project, the ratio of the membrane stress to the load (σ/L) calculated at the beginning of the membrane stress regime (beginning of the secondary creep phase) will be approximately the same for any set of temperature and load at least over the range fixed in this project.

Now focusing more on what happens in the SP sample in the contact region, the thickness of the sample at the tip of the formed hemispherical cup, apart from a small reduction in the first bending phase, does not change substantially throughout the creep test (Figure 7-6, p.174). This means that this area is not very much involved in the creep process. Instead, the annular area defined by the minimum thickness is the most critical region, where presumably, the stresses are higher. Therefore, it is worth considering whether this region is always pointing to the same portion of material or if during the SP creep test the higher stresses are acting on different portions of material. Because the creep process is a plastic process, and then with no change in the volume of material, the variation of the volume included within this annular region, which will be called "*cup volume*" (Figure 7-7, p.174), represents the shifting of the thinnest section to different portions of the material. For this purpose, it is interesting to plot (Figure 7-8, p.175) the measured *cup volume* for all the interrupted tests on the as-received material. During the relatively fast first stage of deformation, this volume appears to increase at very high rate. Unfortunately, there are not enough interrupted tests to tell the exact evolution of the *cup volume.* Even so, it seems that in the first half of the secondary creep phase, it is kept approximately constant, while it tends to grow in the second part. Consequently, for the calculation of the equivalent stress in the SP sample, it is not enough to consider only the higher stress at the thinnest section, but it is also quite important to take into account portions of material for which this stress should be calculated. Later in the tertiary creep phase, fracture starts to drive the creep process and most probably the propagation of the cracks will force the shift of the thinnest section into regions where the material was previously far away from the most stressed region. However, because this last phase is very short compared with the previous secondary creep phase, it will not play a major role in the stress evolution.

7.1.1.1. SP first fast stage of deformation in the creep test

This first fast stage of the SP creep deformation is driven by the bending mode of deformation in which the elastic component is a very small fraction. Although, in this early phase the creep is already tending to relax the tension by some softening processes, the general distribution of the stresses and particularly the radial stress should still be the same as defined in the bending model. The contact between the puncher ball and the specimen is increasing very fast, just as the area, where later the necking will appear, is reaching quickly the proximity of the contact boundary where the bending model suggests a very small value for the radial stress. However, at that time, the deformation is already switching to the stretching mode, especially at such a critical location. Remember that the transition between the complete switching from the bending to the stretching mode is represented by the transition to the secondary creep phase. Then, considering the "as-received material", there are two interrupted tests, which are believed to belong to such a transition phase. The set of temperature and load were respectively 560°C and 340 N. The complete tests at such conditions are expected to give a time of failure of around 700 hrs, which approximately matches the time of failure of the uniaxial test at 560°C under a stress of 190 MPa. These interrupted tests are identified with the codes M1-09 (interrupted at 0,12 hrs) and M1-10 (interrupted at 0,60 hrs) (Table 5-5, Chap.5: *). Unfortunately, because of the initial extremely fast stage of the SP creep test, it is very difficult to obtain interrupted tests in the genuine early bending phase. In any case, applying the bending model and calculating the stress in the area of interest (at the external side approximately where the necking is expected later), a very small value (< 50 MPa) is found and in compression. Most probably, because the deformation mode is close to switching into the membrane stretching, the stress should be very low anyway but slightly in traction. The full usage of the membrane model is not useful because it is giving a too high membrane stress. For the two aforementioned interrupted tests, values of 370 and 320 MPa are found which are much larger than the expected maximum value of 190 MPa.

7.1.1.2. SP Secondary creep phase

Further along the secondary creep phase, the thinnest section, which is now under the contact region, is expected to assume an approximately constant membrane stress. Indeed, it seems that during secondary SP creep phase the decrease in stress due to the growth of the contact surface tends to be balanced by the reduction in thickness, which pushes up the stress. The peculiarity is that such a region at constant stress is moving in the SP sample touching different portions of material.

The experimental results show such behaviour (Table 5-5, p. 95). (see Appendix) Two sets of creep condition were chosen at 340 N at 560°C and 270 N at 600°C. Consider first the set of interrupted SP test along the secondary creep phase on the "as-received material" for 340 N and 560°C. They are the tests M1-15 and M1-16 which are at the beginning of the secondary creep phase, the test M6-02 at approximately half creep life and finally the tests M1-19 and M6-12, which are at the end of the secondary creep phase. For some of these tests (M1-15, M1-16, and M6-02), it was difficultto give a clear indication of their percentage creep life, because they were interrupted before reaching the point of minimum deflection rate (which can be used to derive the rupture life, Figure 5-2, p. 98). However, it can be roughly estimated (with an uncertainty of ±10%) as a percentage of the failure time of the complete test at the same condition. So, it is found respectively an approximate percentage of M1-15 = 5%, M1-16 = 20% and M6-02 = 40%. On the other hand, for both the tests M1-19 and M6-12, an average value for percentage of creep life of 80% (± 5%) can be easily found because these tests were interrupted after reaching their minimum deflection rate. There are only three tests at 270 N load and 600°C. They are the tests M9-01, and M6-08 which are at half creep life and the test M6-11 which is further in tertiary creep phase. The percentage of creep life is given with a good precision for the longest test: M9-11 = 97 %, while for the other two tests (M9-01 and M6-08) it can be roughly estimated as a percentage of the failure time of the complete test at the same condition. So, it is found respectively an approximate percentage of: M9-01 = 50%, and M6-08 = 60% (±10%).

Applying the membrane model to these interrupted tests (the friction coefficient has been fixed at 0.8 [Maile (1998)]), the stress values found at the thinnest section are respectively in M1-15 = 201 MPa, M1-16 = 183 MPa, M6-02 = 175 MPa, M1-19 = 181 MPa and M6-12 = 187 MPa for the interrupted tests with 340 N of load, and M9-01 = 165 MPa, in M6-08 = 150 MPa, and in M6-11 = 186 MPa for the 270 N interrupted tests. The highest stress found in the test M6-11 justifies thinking that the sample is very close to the failure. In comparison, using the other model presented earlier [Dobes (2001), Chakrabarty (1970)] at the stage of M1-19, the stress calculated are respectively around 400 and 240 MPa, very far from the plausible value of 190 MPa.

Therefore, it seems that, all along the SP secondary creep phase, the membrane stress at the thinnest section is kept approximately constant. The logical explanation is found in the combination of hardening and softening processes, which are developing at the same rate as expected in the steady state creep phase. Remember that the rate of work hardening can be expressed by [Orowan (1946)]

Eq. 7-5

$$h = \left(\frac{\partial \sigma}{\partial \varepsilon} \right)$$

and the rate for recovery by:

Eq. 7-6

$$r = -\left(\frac{\partial \sigma}{\partial t} \right)$$

But also the stress is a function of strain and time:

Eq. 7-7

$$\sigma = f(\varepsilon, t)$$

So, the change in stress due both at the hardening and recovery can be expressed by:

Eq. 7-8

$$d\sigma = \frac{\partial \sigma}{\partial \varepsilon} \cdot d\varepsilon + \frac{\partial \sigma}{\partial t} \cdot dt$$

During the steady state creep, is $d\sigma = 0$, hence:

Eq. 7-9

$$\frac{d\varepsilon}{dt} = \dot{\varepsilon}_s = -\frac{\partial \sigma / \partial t}{\partial \sigma / \partial \varepsilon} = \frac{r}{h}$$

However, this approximately constant stress region is moving within the SP sample during the creep test involving different portions of material. In fact, from the beginning of the secondary creep phase up to approximately half of the sample creep life, the portion of material defined by the thinnest section and thus with the highest stress is approximately the same. But, as soon as the sample enters the second half of its creep life, as the plot in Figure 7-8, p. 175 shows, the *cup volume* will increase. This means that the thinnest section will involve other portions of material. The secondary creep phase is assumed to be the most important phase in the whole SP creep test. In fact, the minimum deflection rate, situated around 50 % of the sample creep life and directly related to the creep life (Figure 5-4, p. 99), is completely defined by the way the SP specimen is deforming during such a phase. Consequently, the critical area of the specimen where the stresses are to be calculated is selected at the underside of the thinnest section when the sample is around the end of its secondary creep phase (80-85 % of creep life). Later in the tertiary creep phase, the driving process would be crack growth, which is occurring at the inner part of the sample at the boundary between the contact region and the unsupported region, as defined at the end of the secondary creep phase.

Considering the two tests M6-02 (40 % creep life) and M6-12 (80 % creep life), the increase of the *cup volume* is about 0,2 mm^3. These data will provide the location of the critical area within the SP sample. Indeed, adding this surplus of volume at the shorter test (M6-02), the angle pointing out the borders of this extra area identifies the location at the underside of the specimen, where at the stage of the M6-12 creep life, the thinnest section will be located (Figure 7-9, p. 176). This portion of material will be then situated in the unsupported region, and consequently the Eq. 7-2 (p. 143) should be used in order to calculate the stresses at the critical location. Following such a methodology, the calculated stresses at the critical area for the available interrupted SP creep tests on the as-received material can be related to their percentage of creep life using the load/stress ratio (Figure 7-10, p. 177). (Table 5-5, p. 95). For further applications, it is worth noting the difference of about 15 MPa found between the stress at the thinnest section (higher stress) and the stress at the critical area when the SP sample is approximately at half of its creep life

7.1.1.3. SP Tertiary creep phase and fracture

When the strain reaches a high enough value for which the material contained in the thinnest section is so damaged that it cannot maintain the balance between hardening and softening, the tertiary creep phase starts and very soon the sample will fail. The failure is due to the growth of cracks resulting from the accumulation of damage, most probably at the grain boundaries (Figure 7-11, p. 178). The fracture will proceed along the more stressed area, which is identified by the arc at the boundary between the contact region and the unsupported region (Figure 6-3, p. 129) (Figure 7-1, p. 170). Increasing stresses are then expected in this last creep phase.

7.1.2. SP creep strain evolution

The strain in SP tests is calculated using the general equation which links the vertical deflection with the thicknessreduction that is reported here:

Eq. 7-10

$$\varepsilon(t) = \ln\left(\frac{t_0}{t}\right) = A \cdot e^{Bd(t)}$$

From such a relationship, the strain rate can be easily calculated as:

Eq. 7-11

$$\dot{\varepsilon}(t) = A \cdot B \cdot \dot{d}(t) \cdot e^{Bd(t)}$$

where d is the vertical deflection and the constants are: A = 0,0429, and B = 2,51.

Now looking at the strain rate trend in the SP creep tests, it appears that the range of time where the strain rate is kept approximately constant is quite wide. From the typical graph where strain rate is plotted against time it appears that the strain rate can be considered approximately constant from the 5% up to the 85% of creep life, which is in accord with the fact that the stresses found on the interrupted tests are approximately constant within this range of creep life. Furthermore, the minimum strain rate is normally located at the early stages of the SP secondary creep phase (20%-30% of creep life) (Figure 7-12, p. 179). This plot is of course referring to the strain at the thinnest section.

At the end of the sample life, the strain at failure is not so easy to identify because the failure is happening all along the annular area and with a section which has an orientation dependent on the creep ductility. However, it is expected that there would be a lower strain at rupture for less ductile materials.

7.1.3. Comparison with the uniaxial creep data (validation of the model)

Before starting to compare the results from the SP creep tests with the uniaxial creep data, it is worth considering the different way in which the stress evolves in the two techniques. First, the uniaxial creep data are coming from tests performed under constant load. Thus, the stresses are continuously increasing in a way strictly related to the rate of creep strain accumulation. The nominal value of stress which identifies the uniaxial creep test is just representing the initial stress. In the uniaxial creep tests, for this material and in the range of the given stresses and temperatures, the increase of the axial stress follows approximately the axial strain trend as the elongation is more or less equivalent to the reduction in area. Thus, for the as-received material at the end of the test, the stresses were estimated to increase up to 20-25 % of the nominal value, whatever level of stress was chosen. (see strain to failure in Figure 7-13, p. 179). Similarly, the stresses in the SP creep sample, as was detailed in the previous paragraph (see Figure 6-1, p. 127, and considers the relationship between the vertical deflection and the strain) appear to be continuously growing through the SP test. This behaviour is reflected in the trend assumed by the load/stress ratio found for the interrupted tests made on the as-received material (Figure 7-10, p. 177). On such a plot can be superimposed the trend of the uniaxial stress for the same material tested at a certain nominal stress, fixing the starting point as the same load/stress ratio as the average for the SP tests. The SP load/stress results fall around the uniaxial curve and can be used to derive an average value of load/stress ratio for comparing SP and uniaxial rupture data. For this purpose, the arithmetical average is giving a value of 1,89 (see Appendix). Consequently, this ratio can be employed for all the SP tests made on the as-received material (Figure 7-14, p. 180) and the relative rupture lives can be represented on an isothermal graph for a temperature of 600°C (Figure 7-15, p. 181), and on an iso-stress rupture life graph for a stress of 340/1,89 = 180 MPa (Figure 7-16, p. 181). These graphs (especially the isothermal plot) show that the SP creep result seems to be slightly conservative in terms of rupture life. A possible explanation could be the effect of multiaxiality, which can play a certain role in diminishing the creep life of the material.

7.1.4. Integrity assessment of hydrogen-aged material by the SP creep technique

According to the analysis made for the as-received material, the proposed model can be considered valid. Now, proceed to investigate whether the procedures so far employed can be usefully applied to the hydrogen-aged material. The hydrogen-aged material is expected to experience a drop in its creep rupture life and a change in its creep ductility. The laboratory evaluation of hydrogen-attack sensitivity of the materials cannot be performed at the service temperature (450 to 480°C) because the processes of carbide destabilization by hydrogen needs a long exposure at that temperature. However, accelerated damage may be observed after exposure for about 1000 hours at 600°C, and classification of these materials is commonly based on this type of test. It is reported that the 2 ¼ Cr – 1 Mo, V modified steel has quite good hydrogen-attack resistance [Bocquet (2000)] and the chosen levels of exposure (3000 and 5000 hours) were expected to lead to similar levels of damage with, in many cases, no significant level of cavitation in the material, even if a reduction in creep life is expected. Nevertheless, and surprisingly, Figure 7-17 (p. 182) shows, where uniaxial tests at 600° C on hydrogen-damaged material are compared with the equivalent tests made on the as-received material, an evident reduction in creep life coincides with an enhancement of creep rate under hydrogen. However, it has to be mentioned that the uniaxial specimen was exposed in hydrogen after manufacture. This, especially at the more severe exposure time, could lead to a serious decarburisation of the external layer of the cylindrical specimen (the decarburised layer was removed from the SP test discs). This decarburisation, the intensity of which decays through the material with a certain gradient, has been estimated (by hardness measurement) to reach a depth of around 0,5 mm for the 5000 hours exposed material. Assuming a logarithmic trend for the depth of decarburisation with the exposure time [Baker (2000)], the decarburisation depth for the 3000 hours exposed material is assumed to be around 0,4 mm. The contribution of this layer to the creep resistance of the creep specimen is without doubt much lower than that from the core of the specimen. This can affect the result of the uniaxial test, leading to lower rupture life, because the effective resistant section is smaller than supposed. However, the correction to be considered for the uniaxial rupture data is difficult to quantify because of the gradient in the intensity of decarburisation. Nevertheless, for the 5000 hours hydrogen exposed material, a hypothetical reduction of around 0,7 mm (0,35 mm depth of decarburised layer) in the diameter of the specimen is assumed, which can increase the nominal stress by around 17 %. For the 3000 hours hydrogen exposed material the reduction is assumed to be 0,5 mm (0,25 mm depth), which can lead to a 12 % higher nominal stress. This can be shown in the isothermal rupture life plot where the nominal stress of the uniaxial data for the hydrogen exposed material can then be represented with a possible range of values (Figure 7-18, p. 182).

In order to analyze the differences in the way the stresses in the SP hydrogen-aged sample are evolving in comparison with the SP "as received" material, some SP creep tests on hydrogen-aged materials were interrupted at different stage of their creep life and their geometrical features analyzed. The SP interrupted creep tests run on the material aged in hydrogen for 3000 h were tested with a load of 340 N at 560°C. All these tests were interrupted within their secondary creep phase. The interrupted creep tests performed on the material aged in hydrogen for 5000 h were also tested at 340 N and 560°C, two in the secondary creep phase and one when the curve moved into the tertiary phase. The critical portion of specimen, where the stress evolution is calculated, can be defined looking at the *cup volume* evolution as was done for the as-received material (Figure 7-19, p. 183). Then, using both the equations for calculating the stresses (the friction coefficient has again been fixed to 0.8 [Maile (1998)]) in the contact region and in the unsupported region, the calculated stresses, at the more critical location in the SP specimen are resumed in (Table 5-5, p. 95) expressed in terms of load/stress ratio along with the average value. These results show that, as for the as-received material, the stresses are increasing in the critical area gradually all along the SP creep tests. Furthermore, the difference in the stress value found between the thinnest section (higher stress) and the critical area when the SP sample is approximately at half of its creep life is of about 15 MPa. In order to compare the SP rupture data with the uniaxial results, the calculated load/stress ratios were plotted against the percentage of creep life (Figure 7-20, p. 184). As with the as-received material, on the same graph can be superimposed the stress trend of the uniaxial tests completed for the same hydrogen-aged material and at a certain nominal stress (the possible effect of decarburisation is not considered), fixing the starting point at the same load/stress ratio as the average of the available interrupted SP tests. For the hydrogen-aged material exposed at 3000 h, the average ratio is 2.19, while for the hydrogen-aged material exposed at 5000 h, the average ratio is 1.71. Both uniaxial curves fit quite well with the SP results. These ratios can be then employed to derive the stresses in the SP test for hydrogen-aged materials (Table 5-4, p. 94). The SP rupture life for the hydrogen-aged material exposed at 3000 h can then be represented on the isothermal rupture life plot for a temperature of 600°C, together with the uniaxial results (Figure 7-21, p. 185). This plot shows, as with the as-received material, that the SP technique seems slightly conservative in terms of rupture life estimation and even more so if the decarburisation factor is considered (possible causing a 12% increasing in the uniaxial nominal stress). A similar plot can be drawn for the hydrogen-aged material exposed at 5000 h. In this case, when considering the decarburisation factor (possibly a 17% increase in the uniaxial nominal stress), the SP technique is rather conservative in terms of rupture life estimation (Figure 7-22, p. 185).The differences for the values of the average ratios found for the different aged materials can then be explained in terms of creep ductility of the material. Actually, the SP creep technique appears to be strongly influenced by the creep ductility, because there is a contact phenomenon involved in the loading of the sample. So the way the specimen is indented by the puncher can lead to different stress states within the SP specimen. The uniaxial creep curves reported in the Figure 7-17 (p .182), show that the material exposed to high pressure of hydrogen for 3000 hours, despite a consistent reduction in creep life, displays even a slight increase of the creep ductility in comparison with the “as-received” material. Instead, the material exposed for 5000 hours also shows, apart from the obvious reduction in the creep life, a lower creep ductility. These slight differences are revealed by the SP technique. This can be observed on the graph where the vertical deflection *d* is plotted against the contact radius *c* (Figure 7-23, p. 186). This plot shows just a portion of the whole graph referring only to the secondary and tertiary creep phase, where the curves can be considered approximately linear. Thus, a reduction of creep ductility, as appears to be the case for the hydrogen-aged material exposed for 5000 h, is expected to lead to a smaller imprint left by the puncher, and then smaller contact radius, while higher creep ductility, as appears to be the case for the hydrogen-aged material exposed for 3000 h, is expected to lead to a bigger contact radius. Remember that the extension of the contact surface (expressed by the angle ϕ_c) has a high relevance in the calculation of stress and, for lower contact radius, the stresses are expected to be higher. For the as-received material the average load/stress ratio (1,89) is just between the average ratios found for the hydrogen-aged material exposed for 3000 hours (2,19) and 5000 hours (1,71). This can in fact explain why the SP results on the hydrogen-aged material exposed for 5000 hours seem to show a slight higher creep life compared with the 3000 hours hydrogen-aged material. The differences involved are however quite small. For a more deep investigation it is suggested to test different materials with more marked differences in creep ductility.

7.1.5. Integrity assessment of thermally-aged material by the SP creep technique

As a result of the apparent difference in creep properties caused by ageing in hydrogen compared to the as-received material and the minimal evidence of hydrogen attack found in terms of cavitation, it was decided to check whether the main contribution to this difference derived from thermal-ageing.

The thermal ageing was obtained at only one level defined by the 3000 hours of exposure in air at high temperature. Only one uniaxial creep test is available on the thermal aged material (140 MPa, 600°C) and the test data is limited to the rupture life (323 hours) and the strain at failure (24%). Yet, while the strain trend is not available, it is proposed to assume for this aged material a strain behaviour similar to the as-received material or the hydrogen-damaged material. In this case, no surface process can affect the result, as the diameter of the uniaxial cylindrical specimen was reduced from 8 mm to 6 mm after the exposure. Looking at the Figure 7-24, (p. 187), it seems that even if the hydrogen ageing can play a role, the contribution of the thermal ageing process during hydrogen exposure is the most important especially if a comparison is made with the "effective" stresses in the hydrogen tests.

The potential of the SP technique for assessing the thermal ageing process was also assessed. A single SP interrupted creep test was completed under the same condition as most of the other interrupted tests (340 N and 560°C) and interrupted around half of the SP sample creep life. Of course, a single test cannot give an exhaustive answer, but some assumptions can be made. For instance, the way the thinnest section is shifting to different portions of material can be assumed to be similar to the other materials (as-received, hydrogen-damaged). Therefore, the stress at the critical area, where the sample will start to fail at the end of the secondary creep phase, can be extrapolated from the data available for the as-received and hydrogen-exposed material in tests interrupted at around half creep life and then reducing about 15 MPa from the value of stress calculated at the thinnest section, which give 216-15 ~ 200 MPa (Table 5-5, p. 95). This

This correspond to a load/stress ratio of 340/200 = 1,7. Applying such approximate ratio to the available SP creep tests made on the thermally-aged material, the plot in Figure 7-25(p. 187) is obtained. This plot shows, even with so few available data, that the rupture data of the SP tests is matching quite well with the single uniaxial test. Thus, although the data was derived from just one single SP interrupted test, its interpretation can be considered as further evidence of the potential of the SP creep technique for integrity assessment.

7.1.6. Suggestion for a procedure for integrity assessment of generally aged material by the SP creep technique.

Therefore, it is expected from these results that the SP creep testing technique has potential for evaluating directly the degradation of creep properties for in-service aged components, both in terms of creep ductility and rupture life. A practical methodology can be then suggested. For instance, from an in-service component working at high temperature and in a rich hydrogen environment, a sufficient number of SP specimens (say 10) can be removed in a non-intrusive way. A few of these can be tested up to failure at different stresses at the operating temperature. A suitable test load is to be chosen to allow the other SP samples to be tested with interruptions at regular life fractions. Analyzing their geometrical features, and using the model presented in this project, the evolution of stress can be defined and evaluated in terms of load/stress ratio. The stress rupture data can then be calculated from the load of the SP tests using the average ratio, and used for remanent life estimation.

7.2. SP tensile technique

In the SP low temperature tests, the ordinary plot of load against vertical deflection is one possible representations of the material behaviour at the given condition of temperature and displacement rate (Manaham 1986). Such a plot at each instant is the result of the combination and evolution of the state of stress and strain in the whole SP specimen and hence it can be used to track such evolution. All the SP tensile tests were made with a vertical deflection rate (or speed) of 0,003 mm/sec. This speed was selected in a way that the resulting strain rate along the meridian direction (calculated with the help of the proposed strain model: Chap. 6) was comparable with the strain rate of the unique available conventional uniaxial tensile test.

The SP tensile test can be divided in different phases, which are marked by the evolution of load during the test (Figure 7-26, p. 188). First, there is the phase 1, characterized by a linear trend, and where the whole specimen is subject to elastic bending. In this phase, the stress-strain state is governed by the Young's modulus with the only exception of the area beneath the puncher where the indentation forces the material to yield. The point *A* defines the departure from linearity and marks the beginning of the phase 2, where the deformation is still in bending mode, but in the plastic regime. Unfortunately, at such low loads, the definition offered by the instrumentation was not adequate for determining the exact position of such a point. In this second phase, the yielding surface is expanding very fast, affecting large portions of the disc, with the stress-strain state governed mainly by the yielding stress of the material and the hardening rate. Later, the deformation mode switches into the membrane mode, which actually increases the capacity of the sample for bearing load. This signals the beginning of the phase 3, and the starting point *B* can be easily found at the inflection point of the load curve. The hardening rate is definitely governing this phase although the membrane stress regime is present only in the SP specimen contact region, while the unsupported region is still controlled by the bending stress regime. Within this phase 3, there is another inflection point in the load curve (point *C*). As subsequently explained, this point can be associated with the passage of the critical area (the portion of material where the SP specimen fails at the end of the test) from the unsupported region to the contact region. At the point *D*, the membrane stress regime is starting to expand very fast in most parts of the SP specimen, affecting also the unsupported region. This marks the beginning of the phase 4, where the strain in the material is so high that the capacity for bearing load is decreasing fast, up to the point *E*, which represents the maximum load and the point where the material reaches its plastic instability. Then necking is appearing and further deformation will be mainly concentrated in the annular area where finally the cracks will start and grow leading to failure.

The tensile properties, at room temperature, of the hydrogen and air aged materials seem to be not very dissimilar from the properties of the as-received material. This can be noted in the graph where the load–displacement curves are plotted for the as-received material, the hydrogen-aged material exposed for 5000 hours and for thermally-aged material exposed in air for 3000 hours (Figure 7-27, p. 189). The two different aged materials are behaving in a similar way and they show just a slightly lower strength compared with the as-received material and an apparently higher ductility (the deflections at the maximum load are slightly larger). This is in accord with the expected behaviour of the aged materials at room temperature [Byeon (2003), Bocquet (2000)]. Hence, the different phases, which define the SP specimen tensile behaviour, can be described more profitably considering the three materials together and, when there is a major difference, some distinction will be remarked. Some SP tensile tests were interrupted at regular fraction during the test, and their geometrical features were analyzed (Figure 7-28, p. 190). All this information was then implemented in the proposed equation (Eq. 6-1, and Eq. 6-3) for calculating stress and strain at the more critical location in the SP specimen. It is then crucial to now identify such a portion of material in order to be able to derive its stress evolution. For this purpose, the links between the different geometrical parameters were analyzed.

The vertical deflection can be related to the thickness of the specimen at the thinnest section by an exponential relationship similar to the one determined for the SP creep testing technique.

Eq. 7-12

$$t_{\phi} = y_0 + A \cdot \exp\left(\frac{d}{x_o}\right)$$

where the constants are determined empirically: $y_0 = 0.586$, $A = -0.08134$, $x_0 = 1.17375$. (Figure 7-29, p. 191) This relationship, as some earlier work shows (Mao 1987), should be the same for whatever kind of material, temperature and deflection rate selected for the test, being only dependent on the radius of the puncher. Unfortunately, the tests carried out within this project were limited to only one temperature (room temperature), and one deflection rate (speed = 0,003 mm/sec), and the different tested aged materials had such similar tensile properties that the previous assertion could not be completely verified.

The variation of the cup volume throughout the SP tensile test is a measure of the shifting of the thinnest section (most stressed area) along different portions of the SP specimen. In the plot (Figure 7-30, p. 192) where the cup volume is plotted against the vertical deflection, it is possible to identify with a good approximation the point *D* (defined by the vertical deflection d ~ 1,05 mm), which defines the beginning of the phase 4 in the load-vertical deflection curve for the as-received material (load ~ 1315 N) (Figure 7-27, p. 189). The same key point can be approximately estimated for the aged materials, at a slightly larger vertical deflection (around d ~ 1,25 mm). After this point, the membrane stress regime, which was so far confined in the contact region, starts to expand in the whole specimen and in the unsupported region, and consequently the thinnest section will be not any more shifting to other portions of the SP specimen. Looking at the plot where the vertical deflection is plotted against the contact radius, the meaning of the point *D* appears clear (Figure 7-31, p. 193). The low rate at which the contact radius is growing, typical of a membrane mode of deformation, starts to be evident after the point *D*, from which the membrane-stretching regime is expanding fast in most parts of the sample. The same can be observed in the graph where the thinning of the tip of the formed hemispherical cup (just beneath the puncher) is plotted against the vertical deflection (Figure 7-32, p. 194). When the membrane stress regime starts to expand then also the thinning at the tip is increasing its rate. This higher rate is kept all along the phase 4, up to when the maximum load is reached (point *E*, begin of necking), and where finally the thinning at the tip is practically zero. Probably this happen because after the point *E,* the deformation starts to be located only at the neck. Hence, for all the interrupted tests previous to the point *D* the position of the most critical area in the SP specimen, the area where at the point *E* the neck is appearing and where later the sample is failing, can be easily located. To their cup volume should be added the volume of material which is missing to fit the difference with the average calculated cup volume on SP tests interrupted after the point *D* [Figure 7-30 (p. 192)]. This critical area will then be identified by an annular strip, which will involve both sides of the specimen. The stress regime at such a critical area has then to be evaluated on both sides of the SP disc and considering if they are in the contact region or in the unsupported region, and finally if the dominating stress regime is the bending or the membrane-stretching.

Consider for instance the hydrogen damaged material exposed for 5000 hours. The available interrupted tests are detailed on the plot in Figure 7-33 (p. 195) (the key points are marked with the "$_H$" as subscript). For each of these tests, the membrane stresses at the critical area are calculated by the equations: (Eq. 6-1, and Eq. 6-3) and at both sides of the SP specimen. The compression stress and the shear stress in the contact region and at the contact side (where they are maximum) are also calculated (membrane model in the contact region: Chap. 6) in order to derive the effective stress (Hill, 1948). The evolution of stress can be then plotted as in Figure 7-34 (p. 196). Byun (2003) adopted a similar methodology, although with a different approach for calculating the stresses. Note that just before the point C_H, the choice of the stress regime (bending or membrane) is becoming difficult because the critical area is very close to the boundary between the contact and the unsupported region. Thus, while for the test HM4-15 it is still considered governing the bending mode stress regime, in the test HM4-16 it has been decided to calculate the stresses using the membrane-stretching model. However, next, the contact side of the critical area passes into the contact region, and this portion of material starts to be subjected both to a compression stress (reported in the plot) and also to a shear stress which leads to an effective stress (von Mises stress- reported also in the plot).

Differently from the SP creep tests, in the SP tensile test, necking is not so evident (at least for this material). Therefore, the critical area has to be considered all through the thickness from the external side to the contact side. Furthermore, the hardening law and the rupture ductile criteria for metals are strictly related to the multiaxiality of the state of stress and to its variation [Brozzo (1972)]. Thus, the SP tensile test results, where the material passes through very different stress states and where the deformation trend is quite complex, cannot be directly compared with the conventional uniaxial tensile test result. The work done in this project on the SP tensile technique is, however, a good step forward in understanding the mechanism of deformation within the SP tensile specimen, especially with the help of the proposed stress-strain model. The SP tensile testing technique has the potential to assess the residual mechanical properties of the material as well as the conventional tests, but further work is needed for a better understanding of the effects of the variation of multiaxiality in the stress state. Other possible applications of the technique, such as the determination of the DBTT (Ductile

Brittle Transition Temperature) or investigation of the fracture mechanics properties (by using notched SP sample), have not been explored in this project. However the work done represents a good starting point.

7.3. Figures – discussion

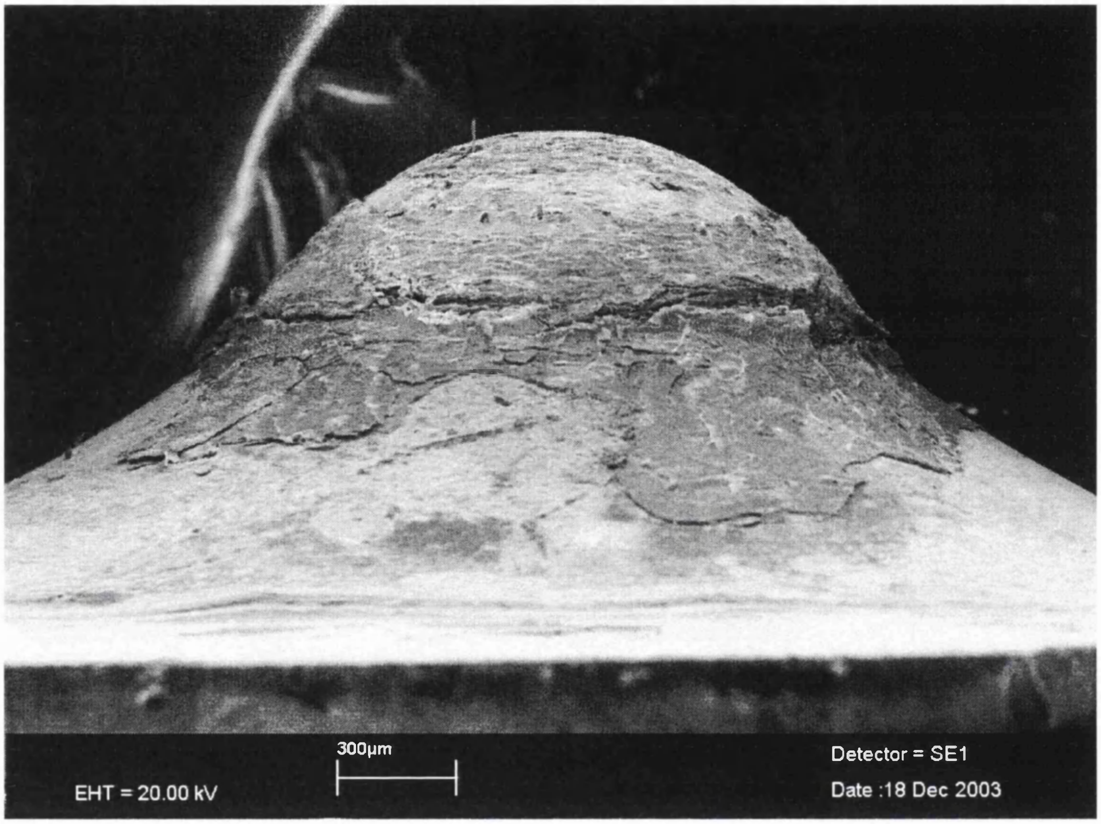

Figure 7-1: Picture showing the annular crack where the SP creep specimen is failing.

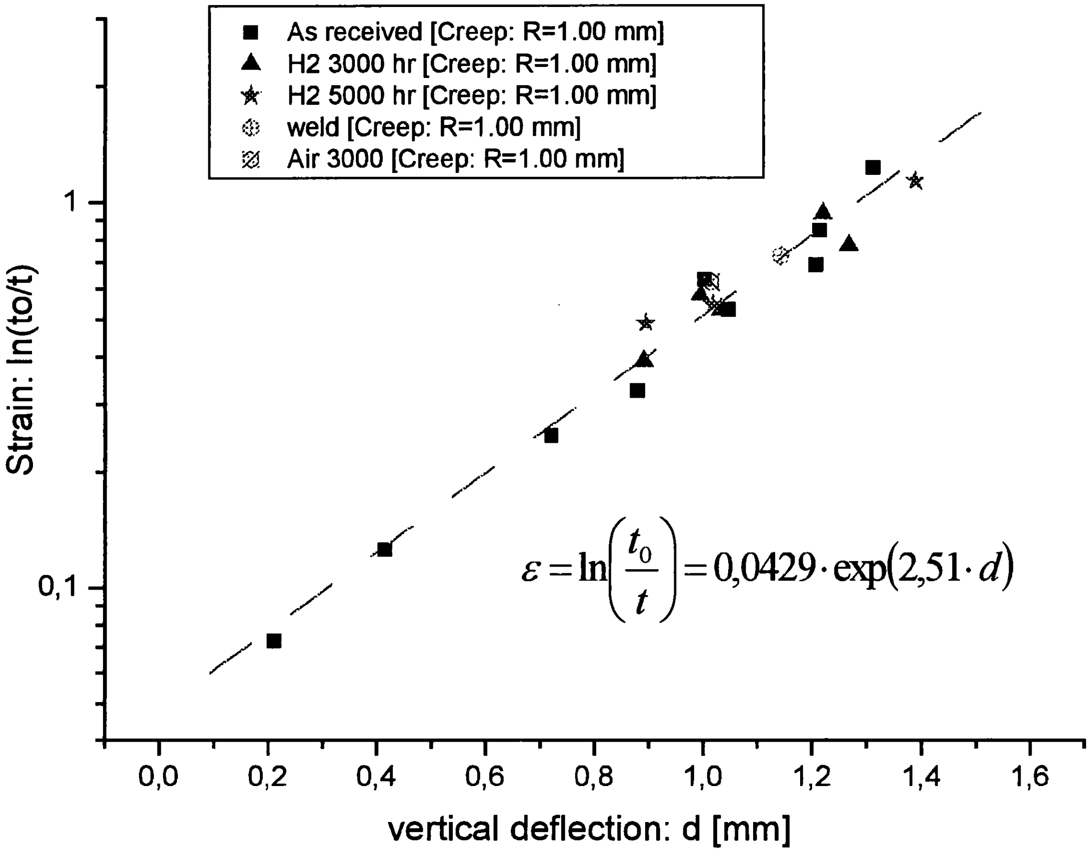

Figure 7-2: Plot of vertical deflection d vs. strain for the SP creep test for the all range of temperature and load (from 600°C to 550°C and from 340 N to 270 N) and for all the level and kind of ageing.

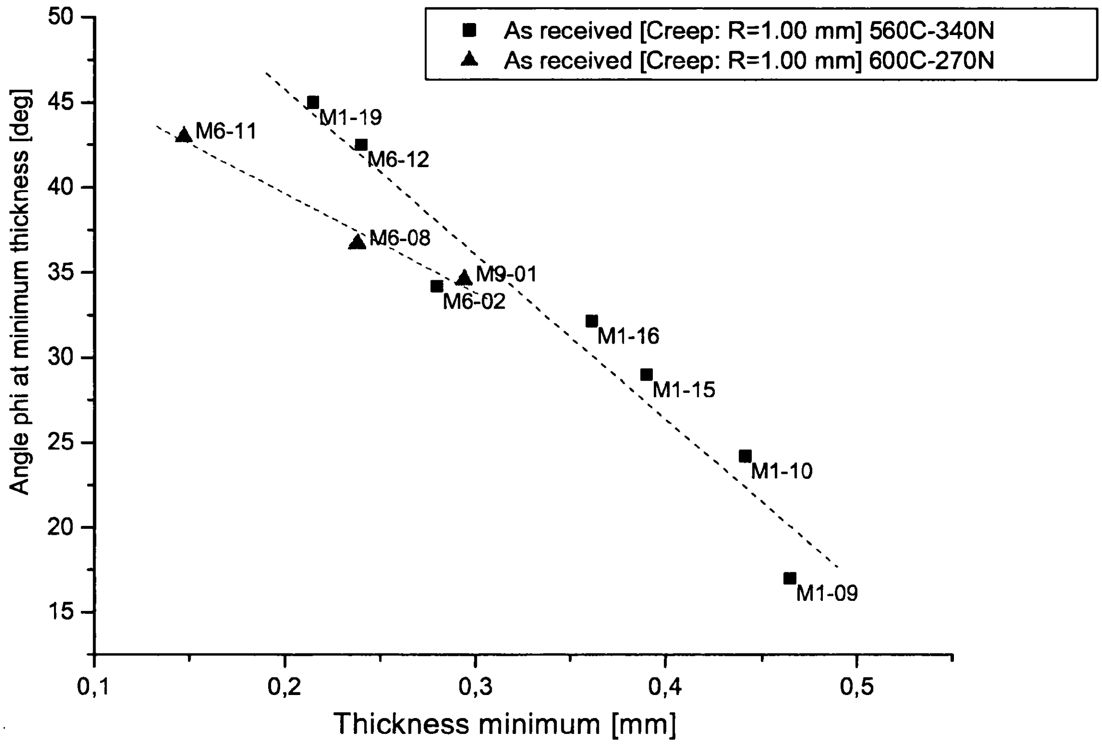

Figure 7-3: Plot of the linear relationship of the minimum thickness against the angle phi.

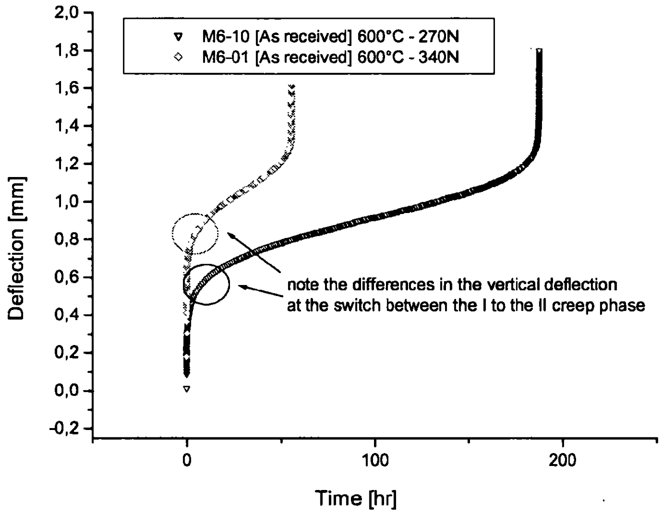

Figure 7-4: Creep curve for the as-received material at the same temperature (600° C) but at two different load: 340 N and 270 N.

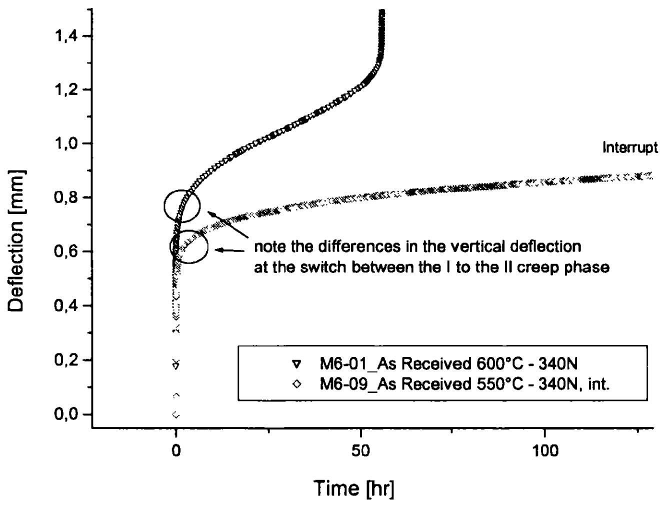

Figure 7-5: Creep curves for the as-received material at the same load (340 N) but at two different temperature: 550° C and 600° C. Note the difference in the value of the vertical deflection at the switch to the secondary creep phase.

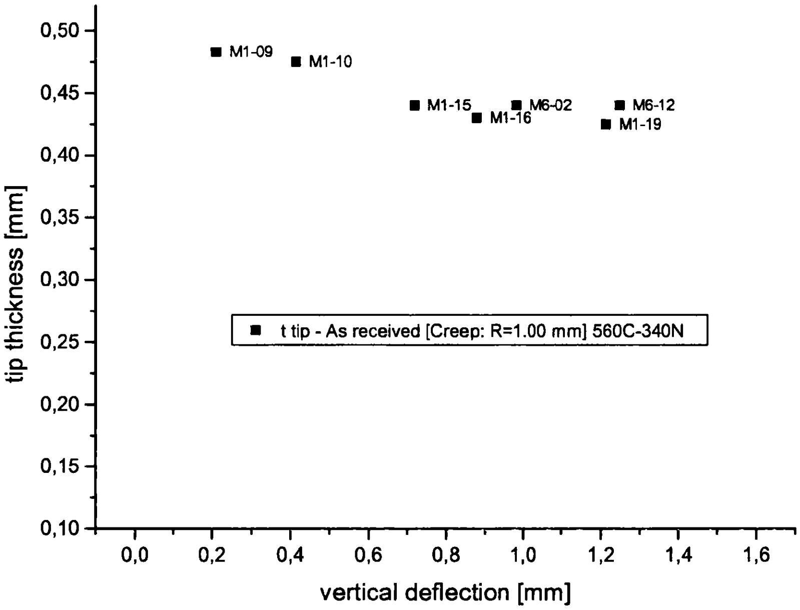

Figure 7-6: Plot of vertical deflection against the thickness at the tip of the hemispherical cup.

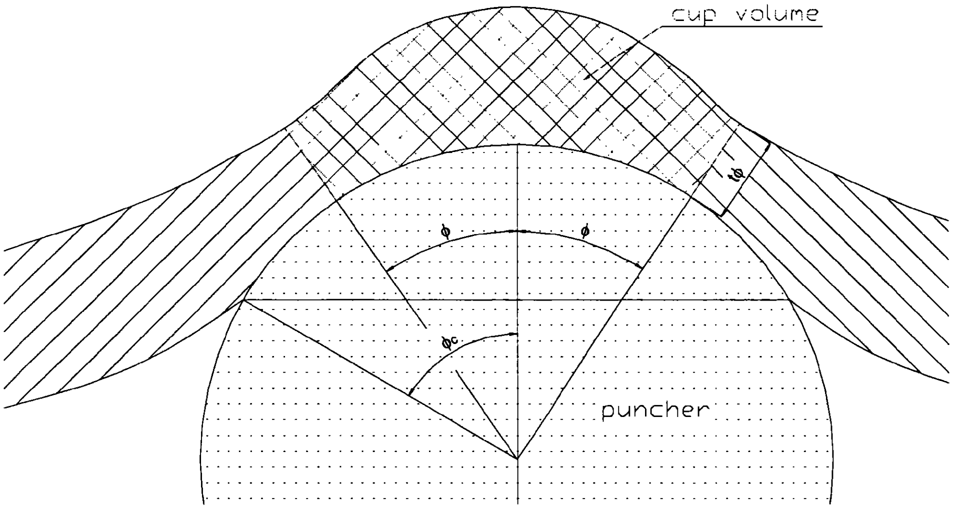

Figure 7-7: Sketch of the section of the "cup volume" in a typical SP creep test.

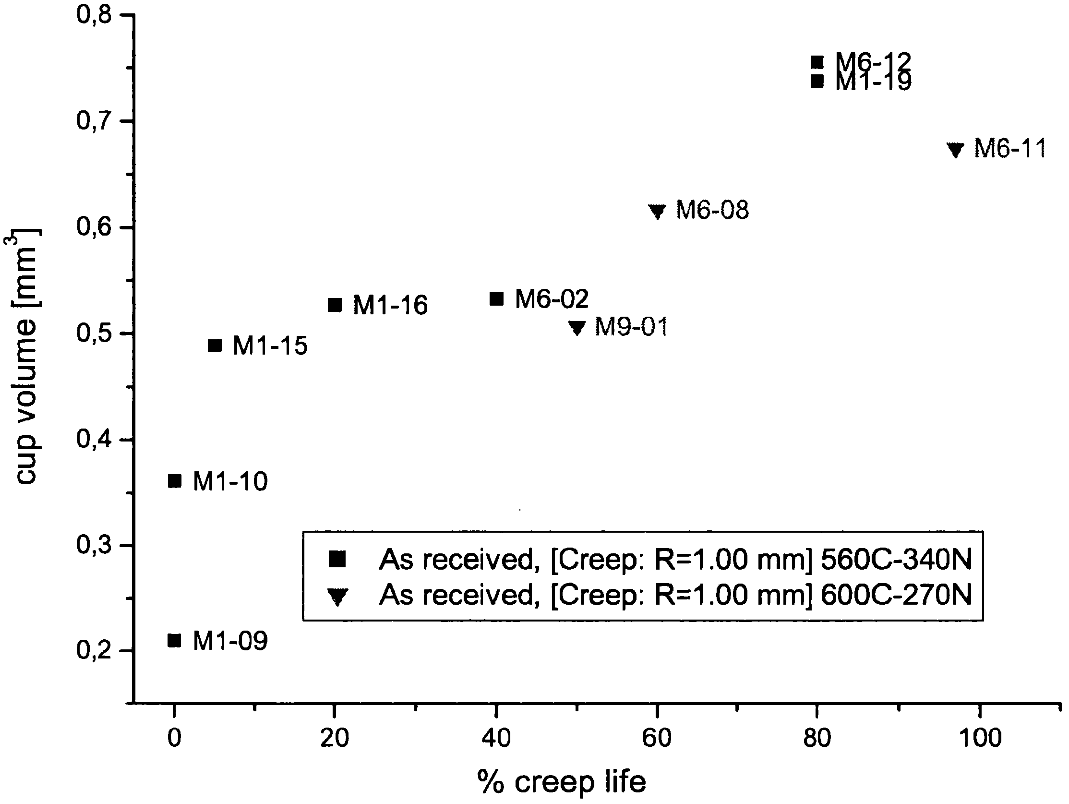

Figure 7-8: Variation of the volume included within the annular strip where the thickness has its minimum. This volume is named as "cup volume". It appears to be constant in the first half of the secondary creep phase growing then in the second part. The same trend is observed in the SP tests with the two set of condition 560°C – 340 N and 600°C – 270 N.

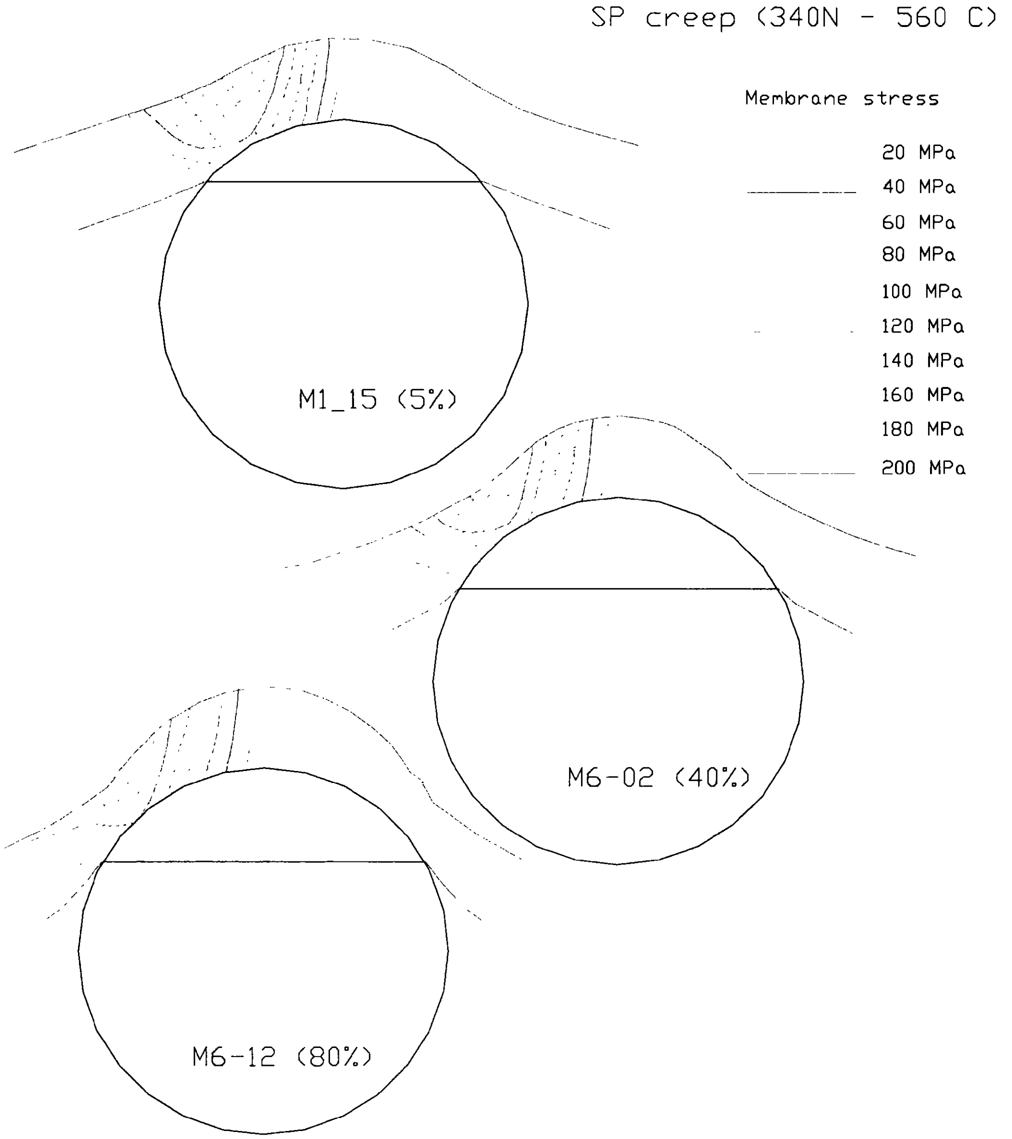

Figure 7-9: Mapping of the evolution of the membrane stress around the thinnest section. SP creep tests at 340 N and 560° C interrupted at 5%, 40%, and 80 % of its creep life. Note how the thinnest section situated in the beginning between the portion of material defined by the lines 5 and 6 is moving a little at 40 % while at 80 % shows a considerable movement in the portion of material defined by the lines 6 and 7.

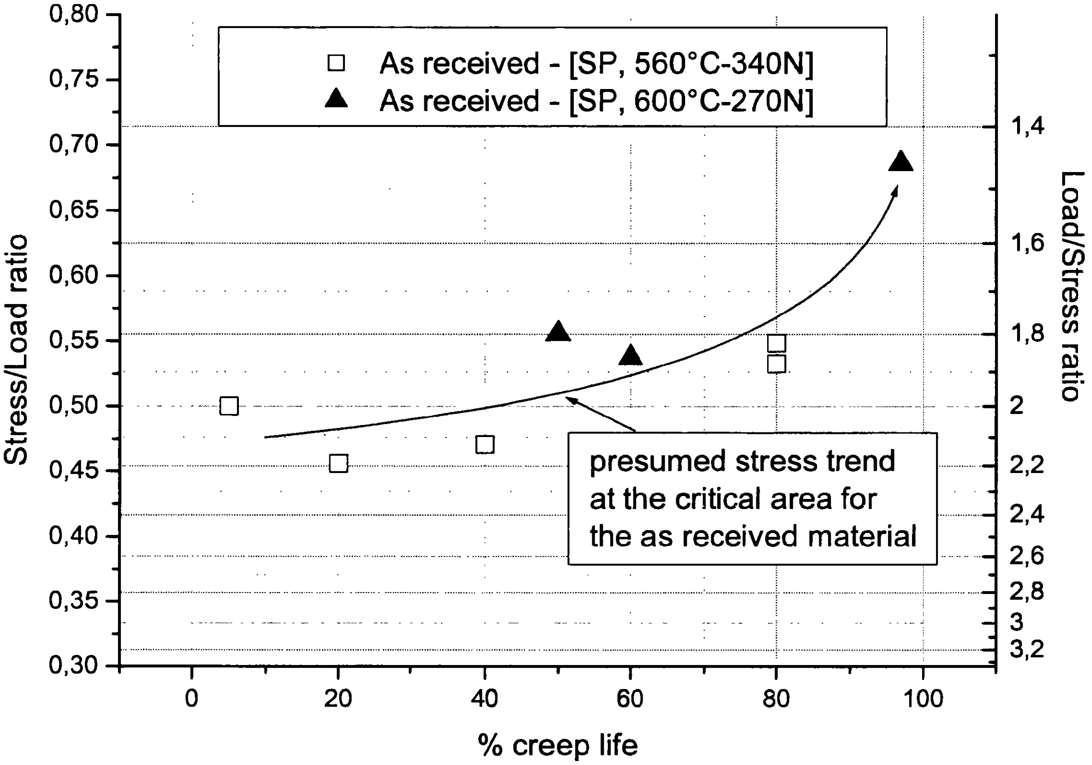

Figure 7-10: Evolution of the SP stress in terms of load/stress ratio for the as-received material.

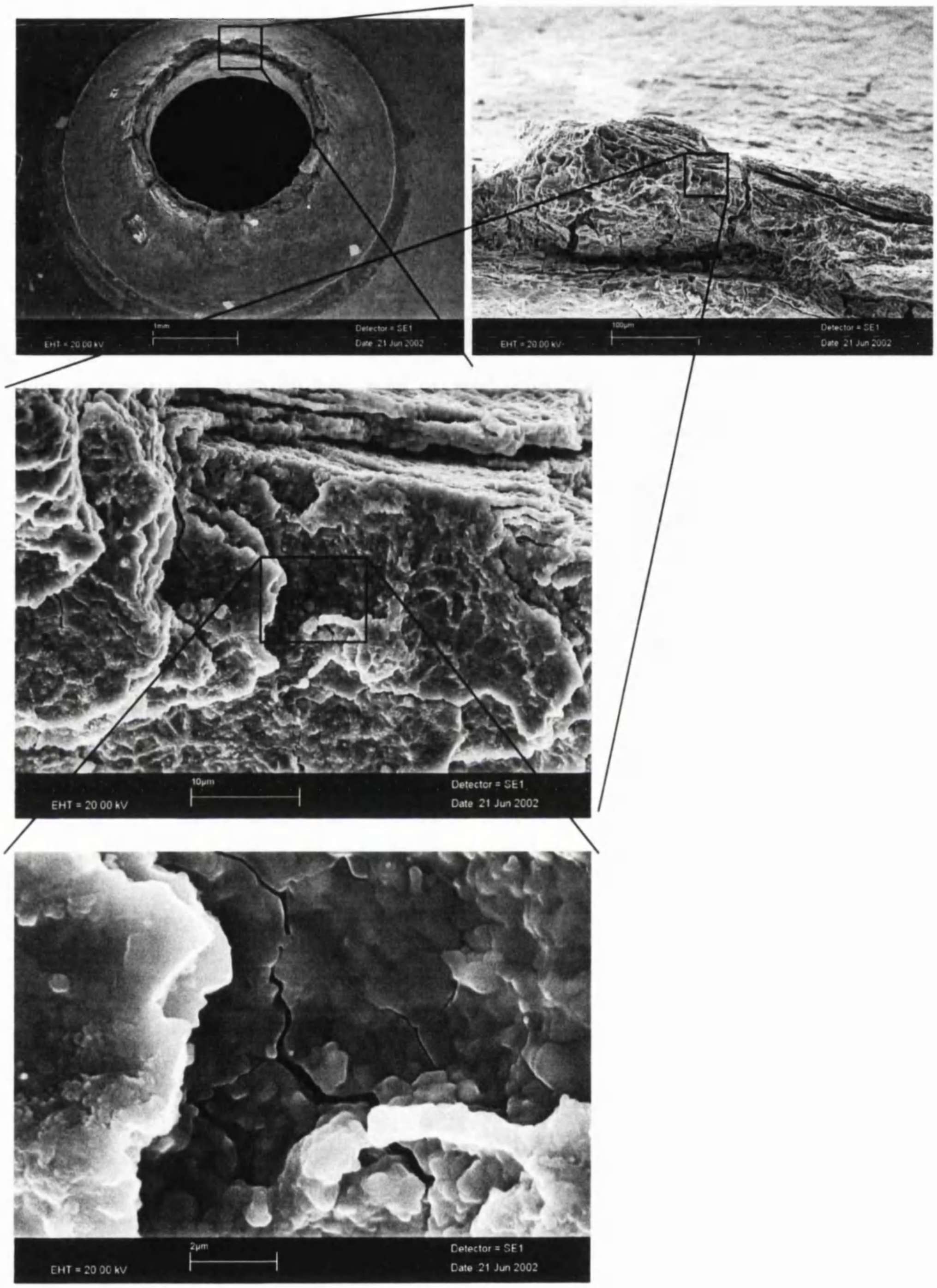

Figure 7-11: Micrographs with the details of the fracture surface in a SP creep specimen. Note the typical intergranular triple point cracks.

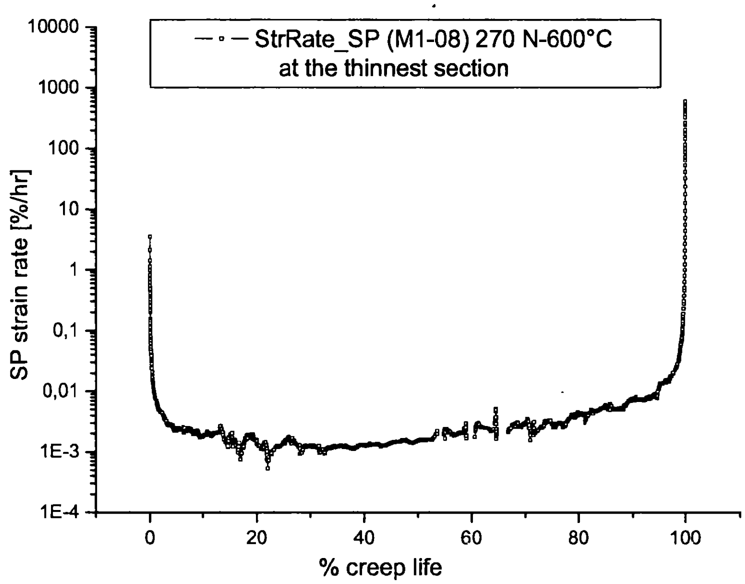

Figure 7-12: Strain rate for the SP test.

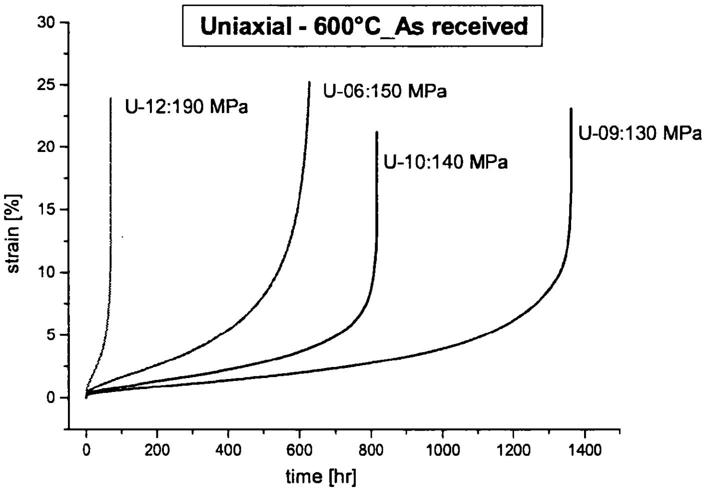

Figure 7-13: Isothermal uniaxial creep curves (600°C) on as-received material.

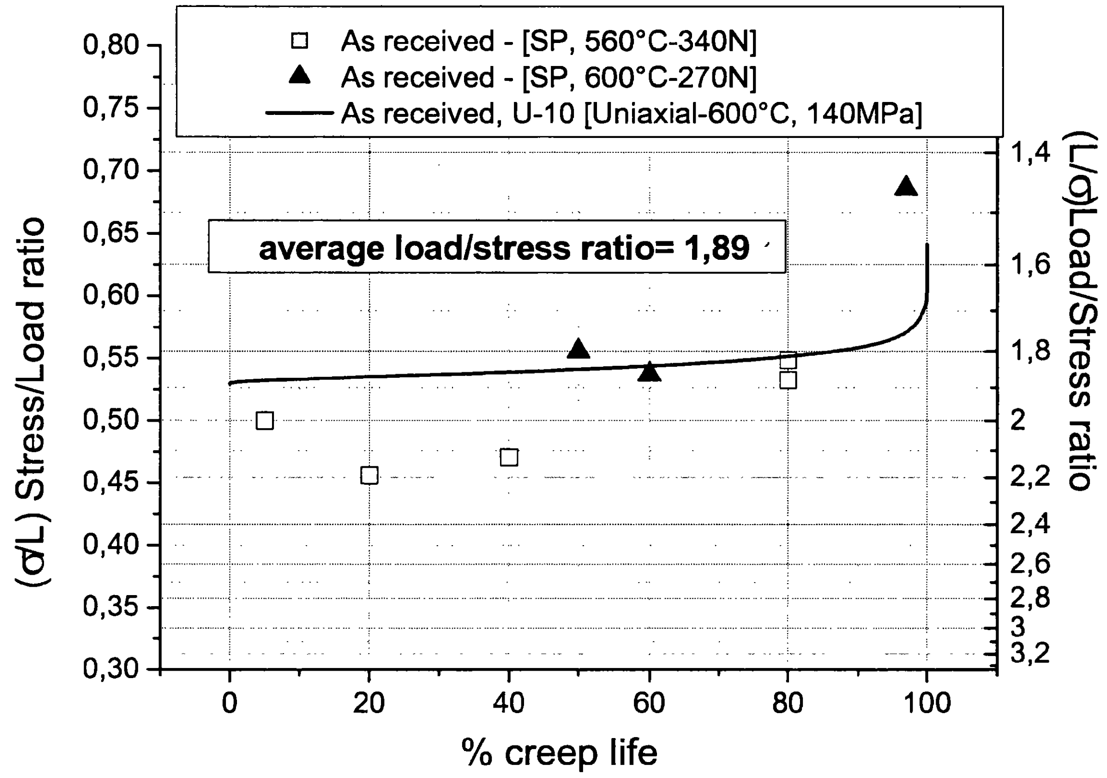

Figure 7-14: Estimation of the SP stress trend compared with the stress trend in the uniaxial creep tests for the as-received material.

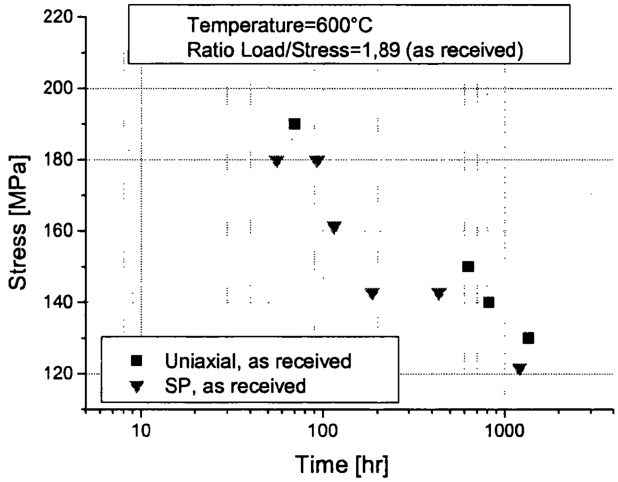

Figure 7-15: Isothermal rupture life plot for the as-received material. The series of complete SP test at 600°C are presented together with the equivalent uniaxial rupture life.

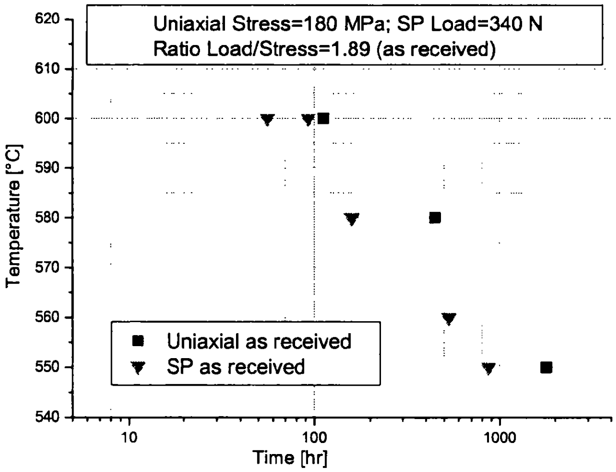

Figure 7-16: Iso-stress rupture life plot for the as-received material. The series of complete SP test at 340 N are presented together with the equivalent uniaxial rupture life. The uniaxial data has been corrected considering the difference of 10 MPa with the real data.

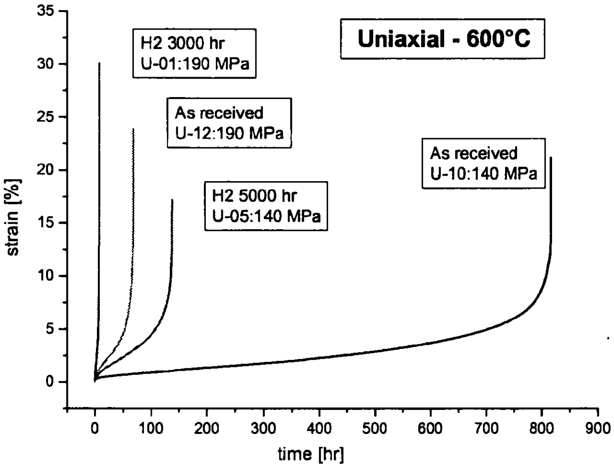

Figure 7-17: Isothermal uniaxial creep curve for the as-received material and for the hydrogen damaged material.

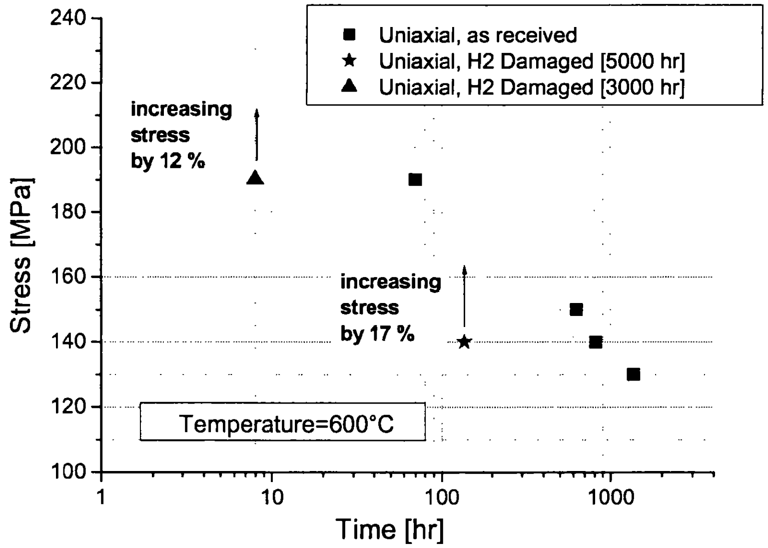

Figure 7-18: Isothermal rupture life plot for the hydrogen-aged material, considering the possible shift of data due to the decarburisation of the cylindrical specimen external surface.

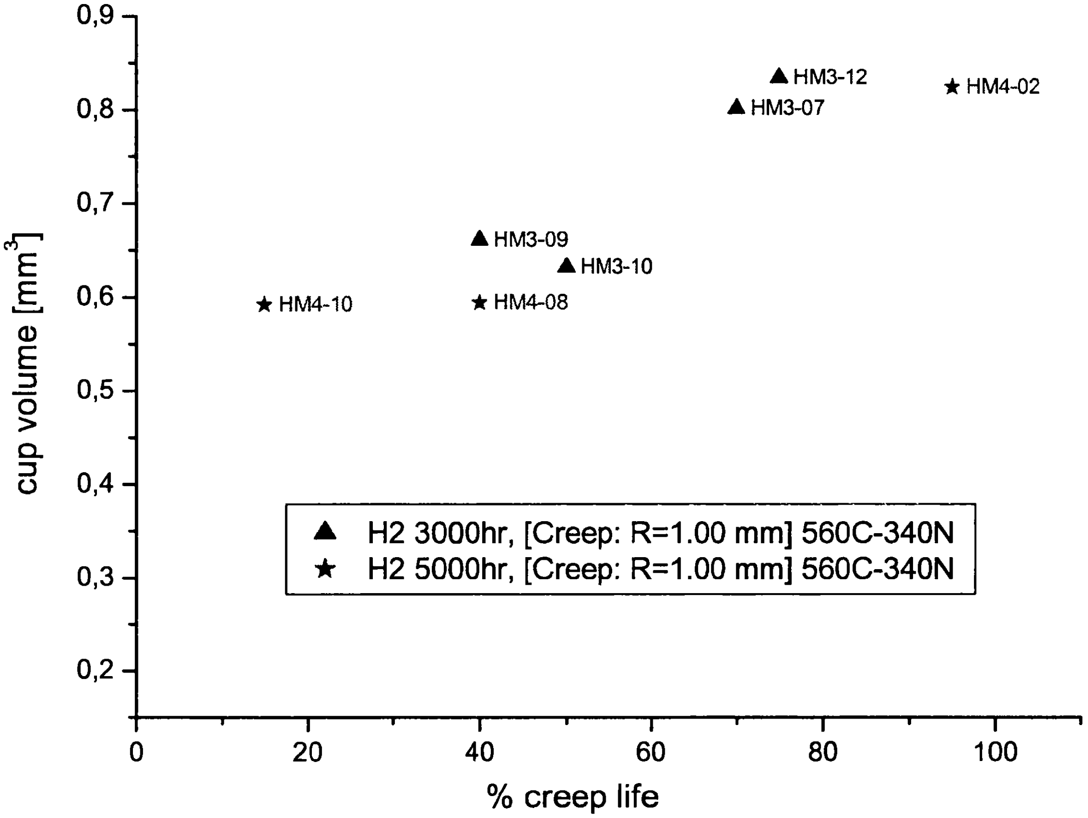

Figure 7-19: Variation of the “cup volume” for the hydrogen damaged material.

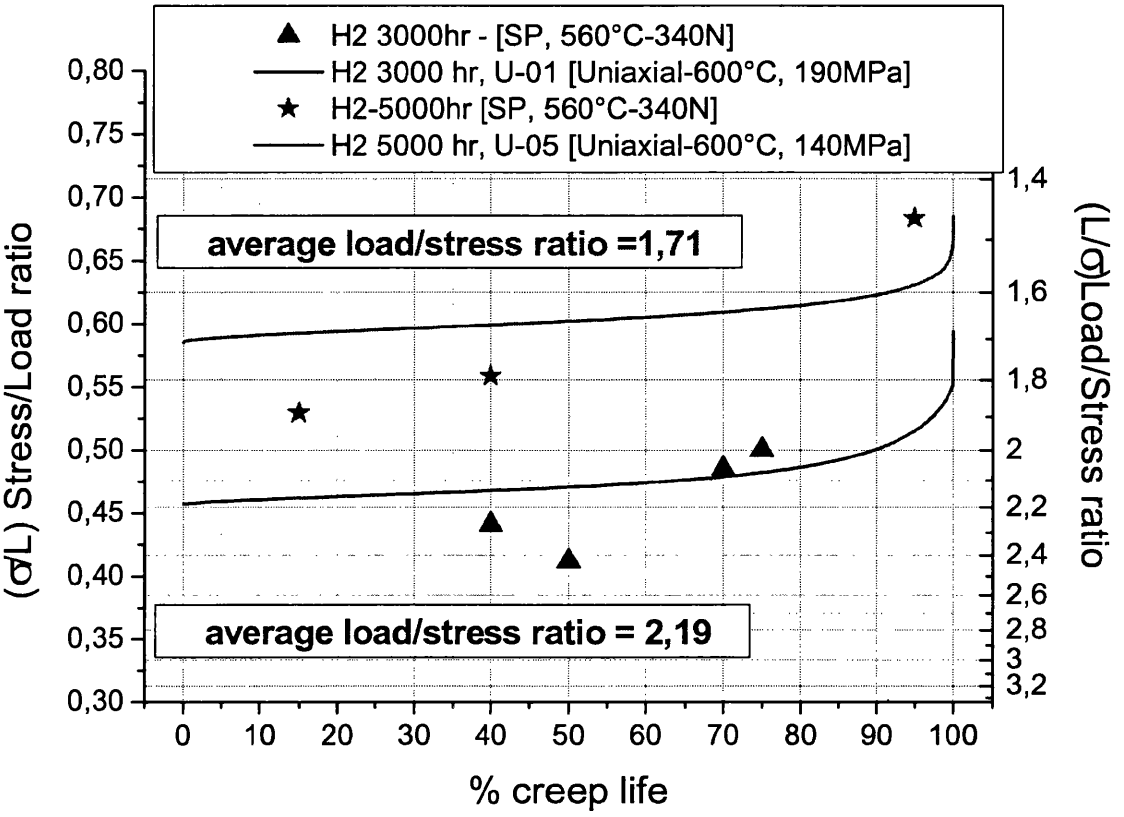

Figure 7-20: Estimation of the SP stress trend compared with the stress trend in the uniaxial creep tests for the hydrogen damaged material.

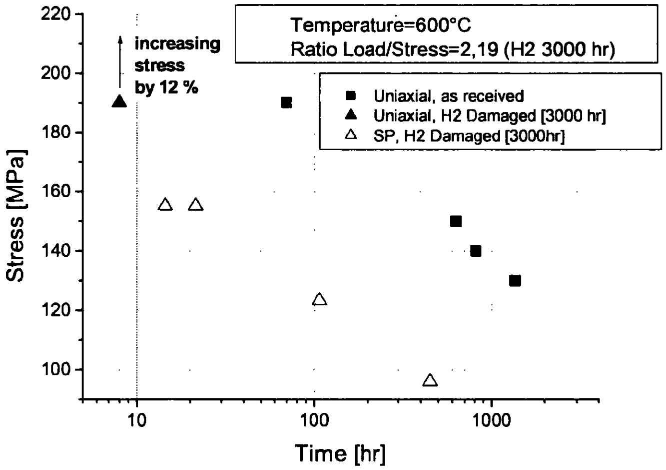

Figure 7-21: Isothermal rupture life plot for the hydrogen-aged material exposed for 3000 h. The series of complete SP test at 600°C are presented together with the corrected uniaxial rupture life data.

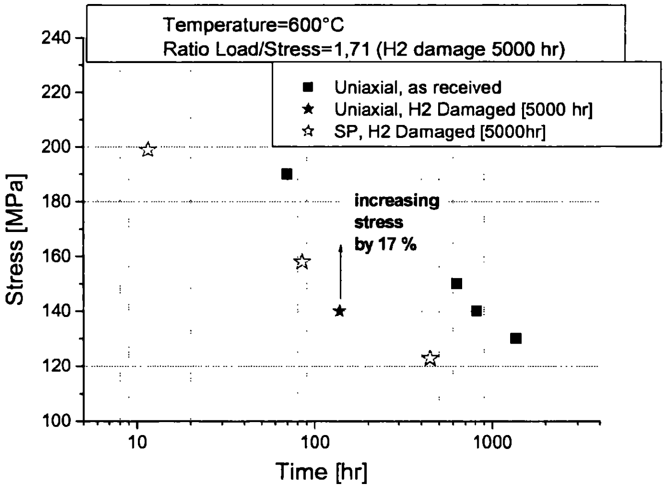

Figure 7-22: Isothermal rupture life plot for the hydrogen-aged material exposed for 5000 h. The series of complete SP test at 600°C are presented together with the corrected uniaxial rupture life data.

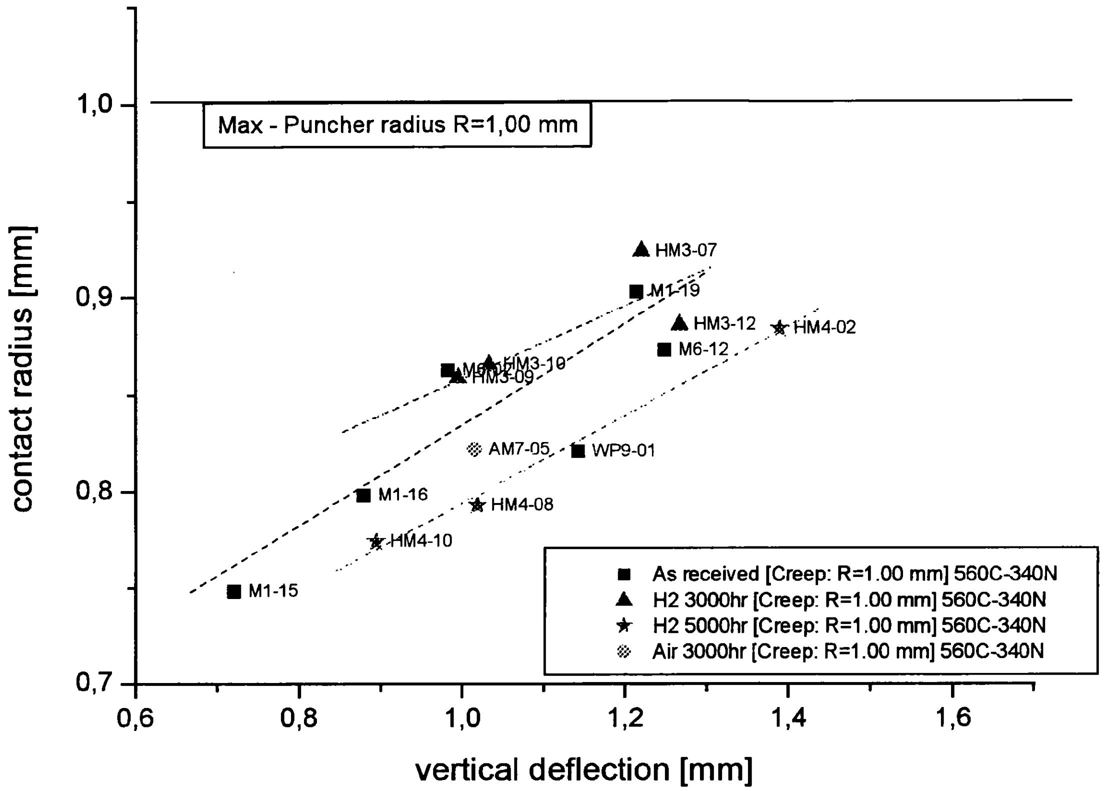

Figure 7-23: Section of the graph, vertical deflection against contact radius, representing the secondary and the tertiary creep phase. Note that for H2 damaged at 5000 h the tendency is to have a smaller contact radius than the as-received material and H2 damaged material at 3000 h. The thermal-aged material seems to behave between them.

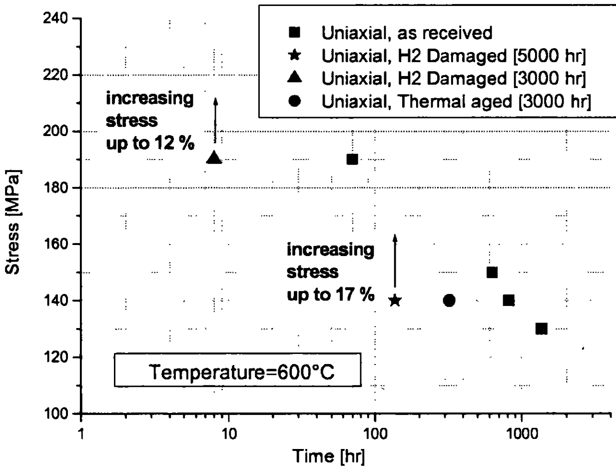

Figure 7-24: Isothermal rupture life plot for the hydrogen-aged material and the thermally-aged material.

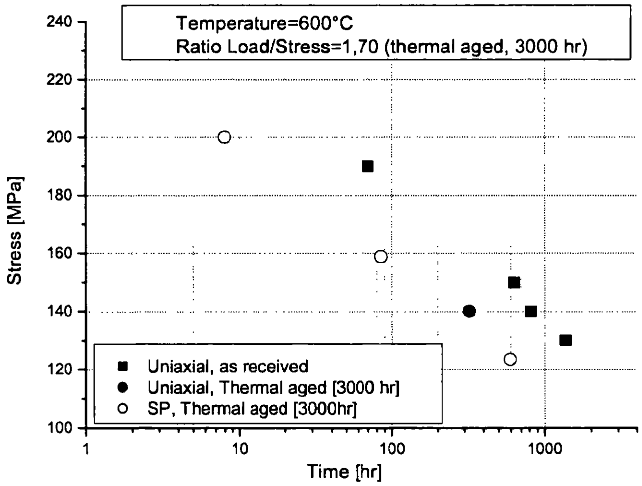

Figure 7-25: Isothermal rupture life plot for the thermally-aged material exposed for 3000 h. The series of complete SP test at 600°C are represented together with the uniaxial rupture life data.

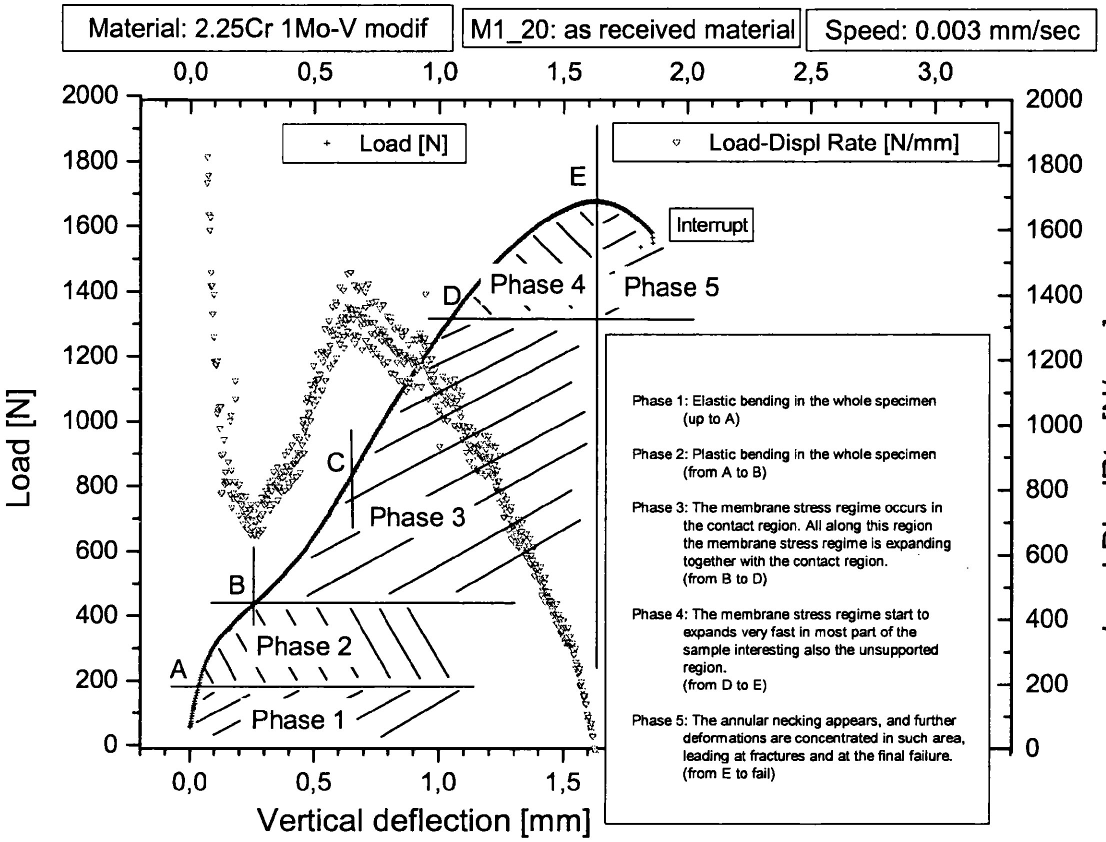

Phase 1: Elastic bending in the whole specimen (up to A)

Phase 2: Plastic bending in the whole specimen (from A to B)

Phase 3: The membrane stress regime occurs in the contact region. All along this region the membrane stress regime is expanding together with the contact region. (from B to D)

Phase 4: The membrane stress regime start to expands very fast in most part of the sample interesting also the unsupported region. (from D to E)

Phase 5: The annular necking appears, and further deformations are concentrated in such area, leading at fractures and at the final failure. (from E to fail)

Figure 7-26: Stress regimes at different stages of the SP tensile test. (interrupted test M1-20 on the as-received material)

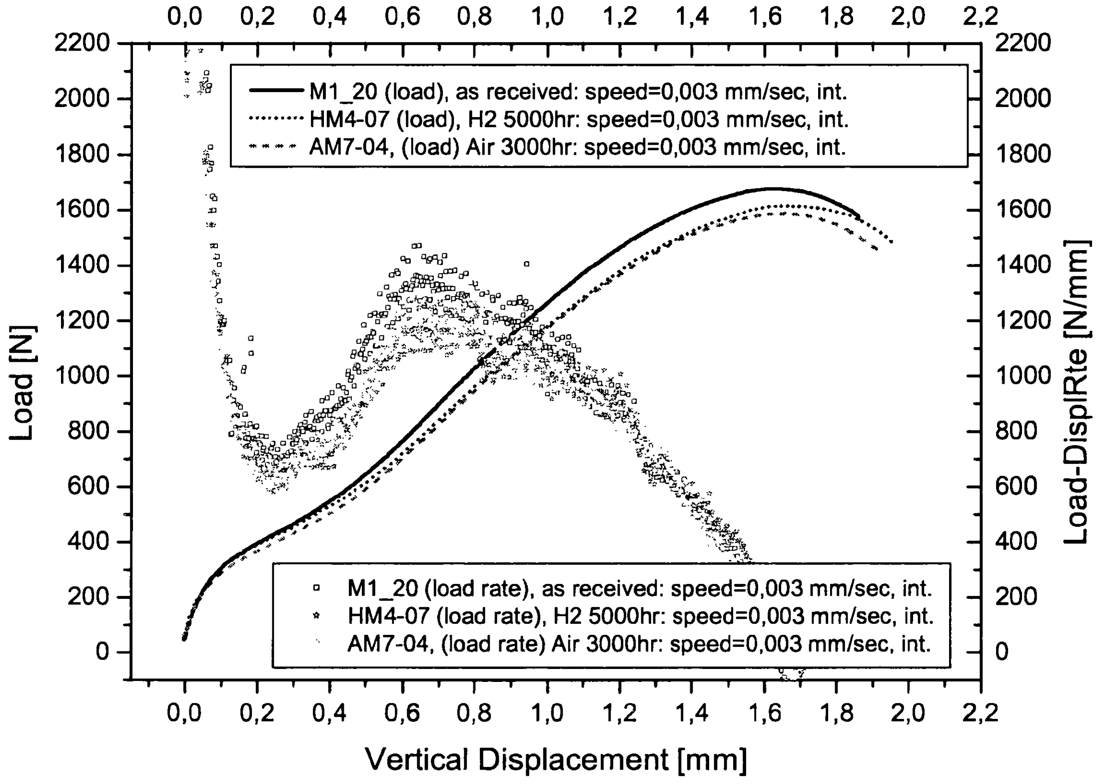

Figure 7-27: Load- vertical_displacement curves for the as-received material and the aged material.

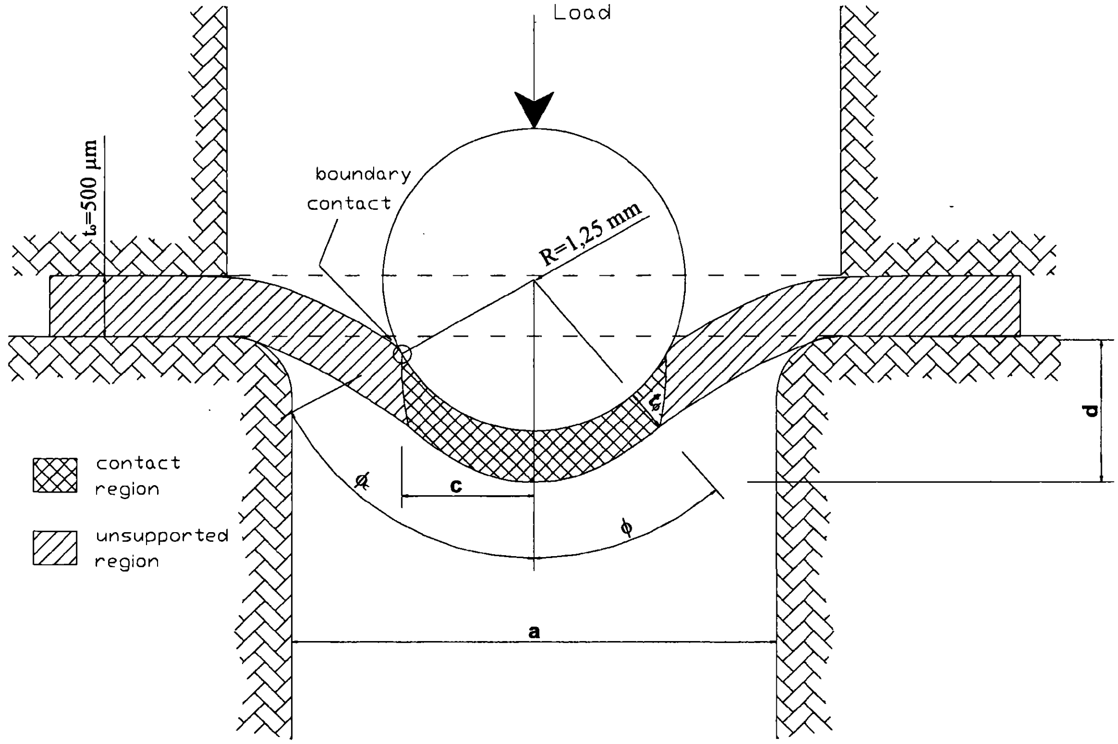

Figure 7-28: Sketch of a typical deformed SP tensile specimen (Interrupted test HM4-18)

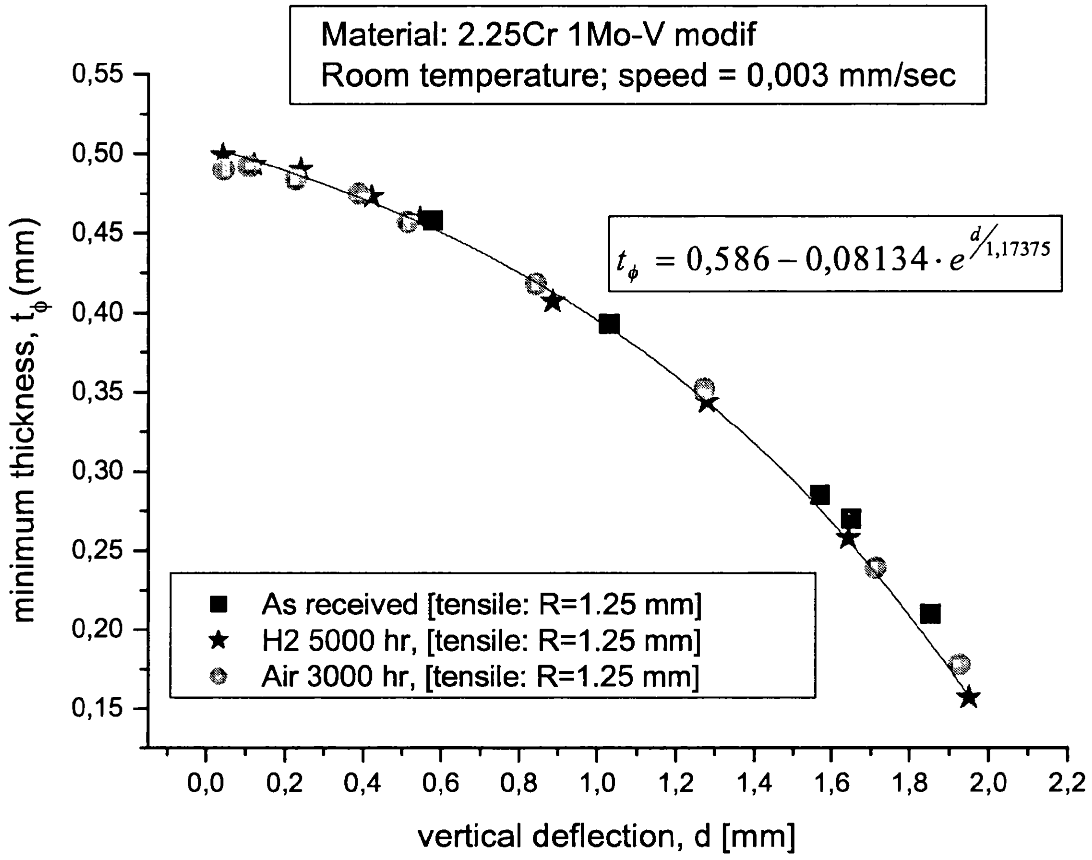

Figure 7-29: Exponential relationship between the thickness in the thinnest section and the vertical deflection in the SP tensile test.

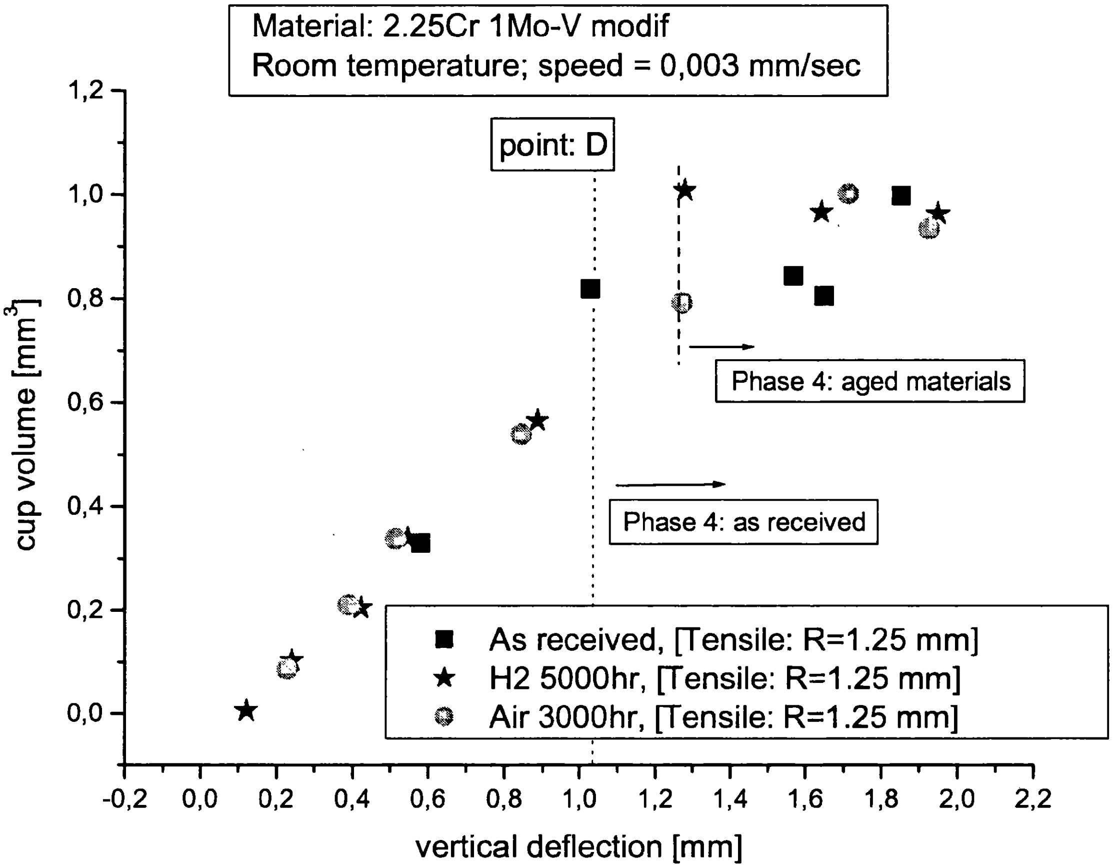

Figure 7-30: Variation of the cup volume during the SP tensile test for the as-received material and the aged material.

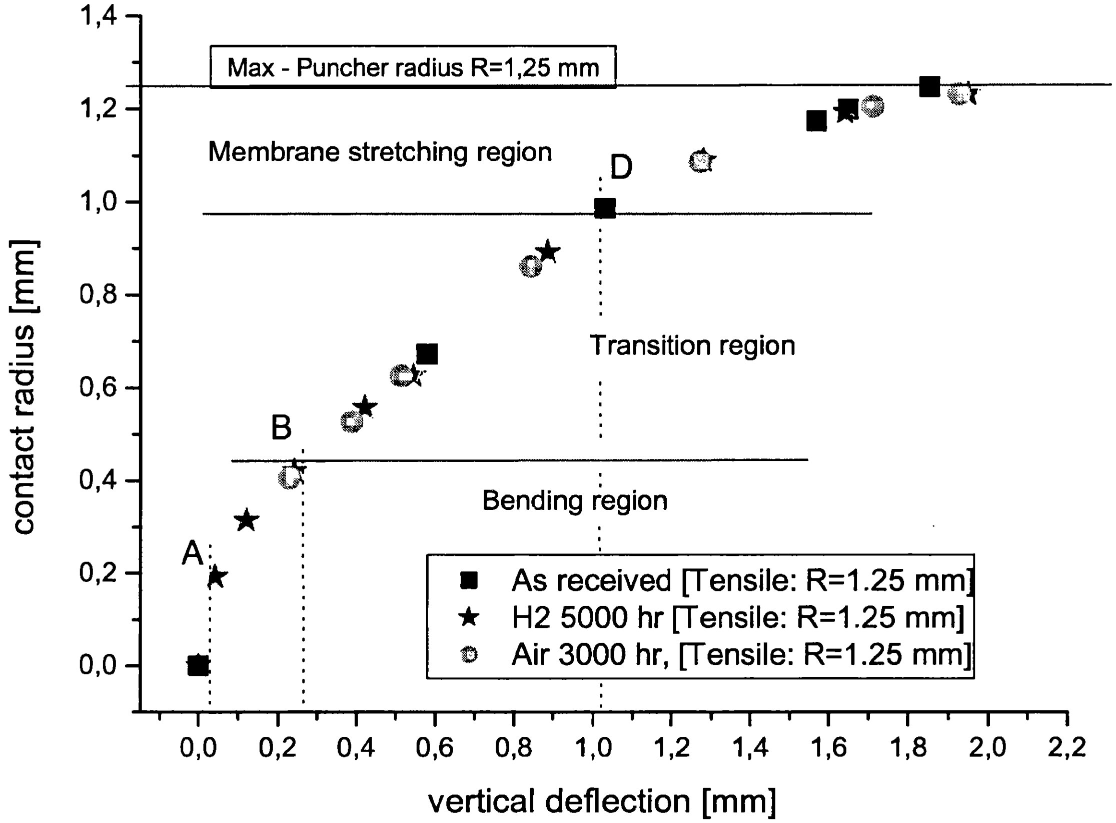

Figure 7-31: Vertical deflection against the contact radius for the SP tensile tests for both the as-received material and the aged material. The points A and D are defining the transition region between the bending regime and the membrane-stretching dominating in the whole specimen.

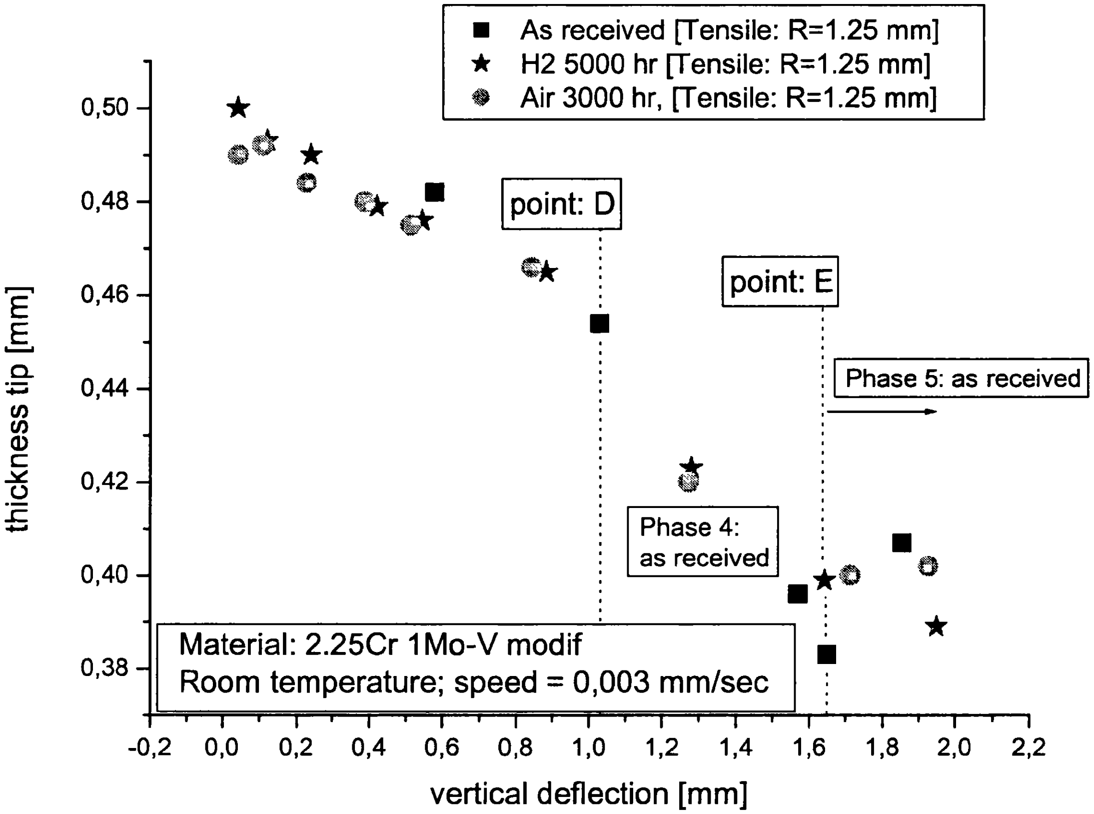

Figure 7-32: Thinning of the SP specimen at the tip of hemispherical cup. Definition of the point D and E for the as-received material during the SP tensile tests.

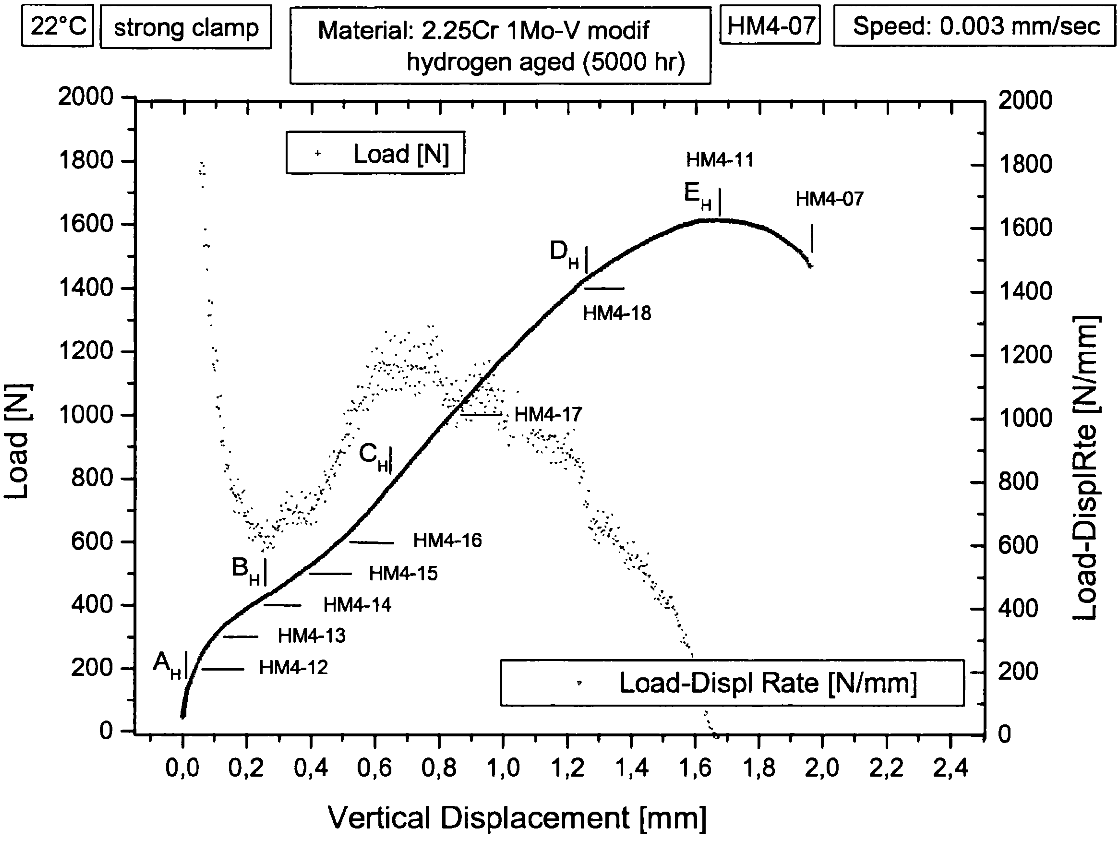

Figure 7-33: Location on the load curve of the SP tensile interrupted tests made on the hydrogen damaged material exposed for 5000 hours.

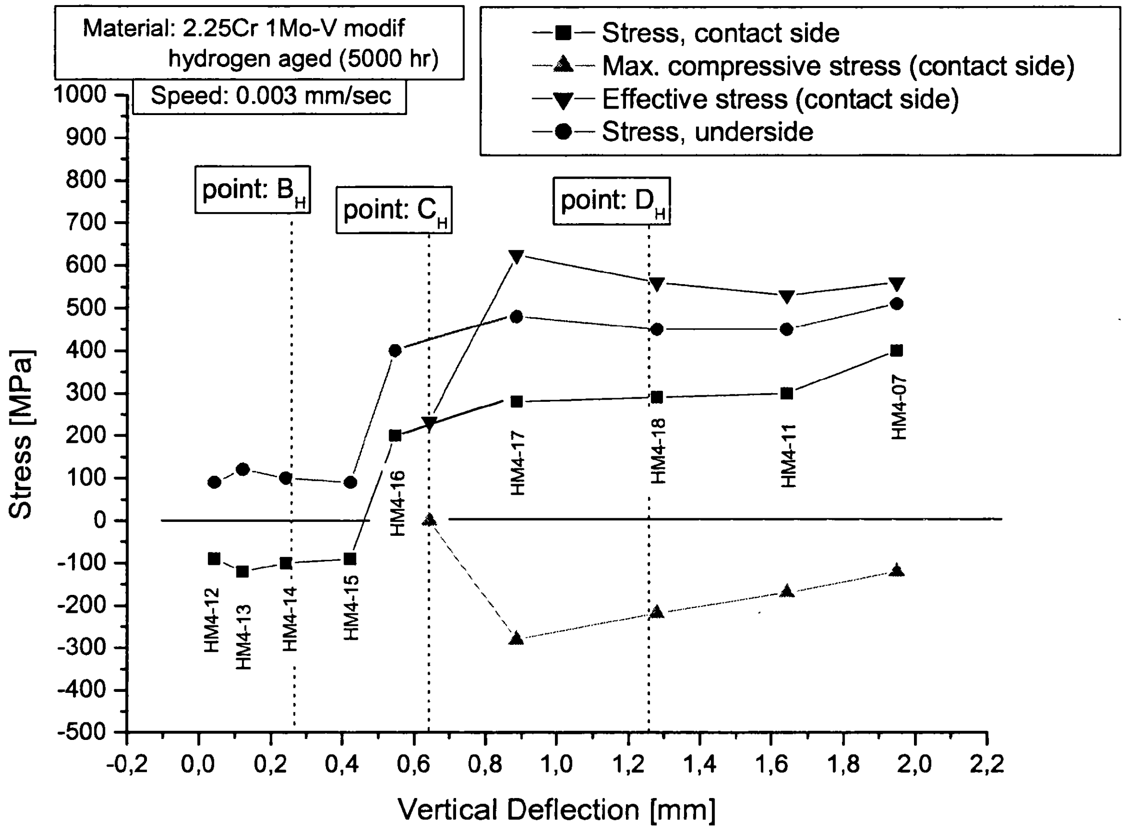

Figure 7-34: Stress trend in the SP tensile test plotted against the vertical deflection. (hydrogen damaged material exposed for 5000 hours)

8. Main Conclusions

This project was carried out in order to assess the reliability of the SP method as a mechanical test technique for evaluation of the residual life and integrity assessment of components in ageing plants The SP testing technique has been applied to the low alloy - 2¼Cr 1Mo V modified ferritic steel typical of high temperature applications in petrochemical plants. This methodology has been shown to be capable of evaluating both the creep and tensile properties of materials. In particular, special attention has been focused on the potential of the SP approach for assessing the deterioration of material due to hydrogen attack and thermal-ageing, in comparison with conventional uniaxial creep methods. From the present investigation, the following conclusions can be drawn:

<u>**The Small Punch test procedure**</u>

- <u>Round Robin Exercise (Cr Mo rotor steel)</u>
  - Testing in air has little influence on SP creep results, at least with short creep lives (100 hours). However, for longer term exposure it is suggested that a protective argon atmosphere should be employed to avoid the effects of oxidation on the creep data and to obtain clean SP interrupted samples for easy measurement of geometrical parameters.
  - The temperature measurement is a critical feature of the experimental SP creep technique, ensuring the correct location and calibration of the thermocouple for a valid measurement of the SP sample temperature.

- The present results show that there is no effect of the sample preparation procedure upon the creep response of the material, providing that the specimen is polished up to 1200 grit and the initial specimen thickness is a minimum of 550 μm.

- The 2¼Cr 1Mo, V modified steel

  - In the SP test, the clamping of the test coupon can play an important role in the way the SP specimen is deforming. To this end, a strong clamping force is suggested for both the SP creep and tensile techniques.
  - Interruption of tests is a suitable method for following the way in which the specimen is deforming during the SP test, thereby aiding the evaluation of the behaviour of the material in continuous tests.
  - The geometry of the components of the SP equipment has been found to be important in determining the deformation behaviour of the SP specimen. In this project, two pieces of equipment with different puncher radii R (1 and 1.25 mm) have been used, but with the same diameter of the receiving hole (a = 4 mm). Although they were used in two different contexts (creep test at high temperature and tensile test at room temperature), the small difference in puncher radius would not affect the application of the analytical stress and strain model proposed in this work. Nevertheless, the definition of a unique radius R is recommended.

Small Punch creep test results

- The SP creep curve clearly delineate a secondary and tertiary creep stage which can be representative of the creep behaviour of the material.
- Based on measurements taken from interrupted tests, a new analytical stress model has been developed which enables the stress evolution during a SP creep test to be successfully evaluated .
- The ratio between the load applied in a SP creep test and the stress in a conventional uniaxial creep test can then be used in order to correlate SP and uniaxial creep test data.
- The creep ductility seems to play an important role in the SP technique as the load is applied by contact.
- The material deterioration due to hydrogen-attack and thermal-ageing could be deduced from the SP creep test, mirroring the deterioration in creep properties observed in conventional creep tests.
- The effect of multiaxiality can play a role in the interpretation of SP creep results, especially considering the last part of the secondary and tertiary SP creep phase.
- As demonstrated by this work, the SP creep testing technique has potential to be an appropriate tool for integrity assessment of in-service plant components.

Small Punch tensile test results

- The simplistic model proposed offers promise as a valid tool for assessing the stress evolution during the SP tensile test.
- Nevertheless, the multiaxial state of stress and its quite complex evolution leads to difficulties in establishing the appropriate yield and ductile rupture criterion for a direct correlation with the conventional uniaxial tensile data.

9. Suggestions for further works

- SP technique

  - Instead of using a single block puncher, it is suggested that a disposable ceramic sphere is employed, especially for the SP creep technique where the high temperature can modify the puncher shape.
  - Further studies should be dedicated to understanding the influence of the clamping force on the SP results
  - It is proposed that the image acquisition system in the SP tensile equipment should be integrated with more advanced tools, such as laser interferometers for detailed strain measurement.

- Interpretation of SP results

  - A Finite Element Analysis could integrate the output of the proposed analytical stress-strain model, especially for interpretation of the more complex SP tensile results.
  - The stress analysis model should be verified for the materials by means of interrupted testing. These should cover a range of creep strengths and ductilities.
  - The particular alloy selected for the SP creep tests was quite resistant to hydrogen attack and the SP behaviour of other materials more susceptible to hydrogen damage should be investigated.
  - The results from long-term SP creep test (up to 10.000 hours) should be considered.

- Because of the small size of the specimen, the SP technique is suited to investigation of the weakest points in a component, such as weldments. To demonstrate this, a single SP creep test has been carried on weldments and the correlation with the available uniaxial creep data has been made (ANNEX: Chap. 10) as a useful reference for further work in this direction.

10. Annex: Integrity assessment of the weldments by the SP creep test.

In this case the available uniaxial test is coming from another PhD project [Manna (2004)]. The uniaxial specimen is a cylinder where half way along its length is located the weld line. Normally the weld is composed of different zones with different properties. Between the Base Metal (BM), and the Weld Metal (WM) there is the so called Heat Affected Zone (HAZ) which can be distinguished in more other sub-zones that are, starting from the base metal, the Inter-critical zone (IC), followed by the Fine Grained HAZ (FG-HAZ) and the Coarse Grained HAZ (CG-HAZ).

The results from the uniaxial cross weld tests on the material from the same batch of material employed in the current project show that the failure, in the uniaxial creep tests, occurs in the IC zone and that the failure is of TYPE IV, with failure times slightly shorter than for the BM. However, there are problems in using the conventional uniaxial testing technique for assessing creep properties of weldments. In fact, it is difficult to discern in the creep curve the information relative for the actual zone where failure is happening, from the contribution due to the others zones of weldments and of the base metal. Hopefully, the SP testing technique would be capable to give direct information on the more critical zone of the weld. Thus, the single SP interrupted creep test made on the weldments (Table 5-5, p. 95) (Chap 4 - description of the material) (340 N, 580°C), interrupted around half of its creep life (55% of creep life), can be treated as has been done for the single test on the thermal-aged material. The assumption is made that the that the behaviour of the SP specimen (at least the way how the thinnest section is shifting upon different portion of material) is not different from the others case already seen (as received material, hydrogen damaged, thermally-aged). Consequently, the stress to be considered at the critical area of this specimen, interrupted at half of its creep life, can be estimated about 15 MPa from the stress calculated at the thinnest section, which give: 223-15 ~ 205 MPa. This corresponds to a load/stress ratio of 340/205 = 1,66. Unfortunately, a part the interrupted test, there are not any more SP creep test made on the weld. However, from the interrupted tests itself can be deduced the rupture life of the hypothetical SP complete test considering its minimum deflection rate, which gives an approximate value of 80 ± 10 hours. Now, from the iso-load rupture life plot can be estimated (assuming for the weld material the same slop like for the as received material) the rupture life at 600°C applying a factor 3. Thus, the hypothetical rupture life at such a temperature can be assumed of around 25 h. Thus, this point can be now drawn in the isothermal rupture life plot (600°C) (Figure 10-1, p. 205). This is matching very well with the single uniaxial rupture data available for this material.

10.1. Figures – annex

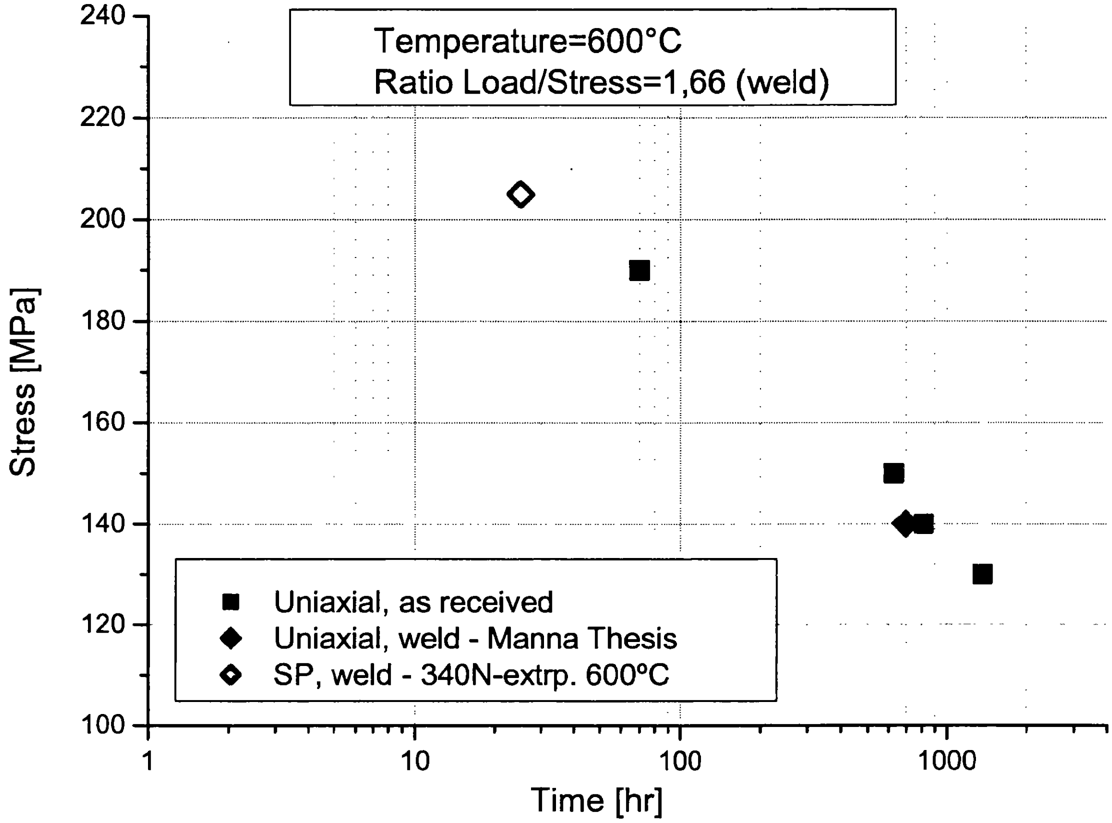

Figure 10-1: Isothermal rupture life plot for the weld.

11. References

(Change p. to pp.
! where: x-y)

- **Baik J.M., Kameda J., Buck O., (1987): "Development of Small Punch Test for Ductile-Brittle Transition Temperature Measurement of Temper Embrittled Ni-Cr Steels"** ASTM STP 888, ASTM Philadelphia PA, p. 92-111.
- **Baker A. J., (2000): "Combined Creep and Hydrogen Attack of Petrto-refinery Steel"**, PhD thesis, University of Wales Swansea, p. 136.
- **Baldev R., Jayakumar T., (1997): "NDE methodologies for characterisation of defects, stresses and microstructures in pressure vessels and pipes"**, Int. J. Pes. Ves. & Piping, Vol. 73, p. 133-146.
- **Bayoumi M.R., Bassim M.N., (1983) "Study of the relationship between fracture toughness (J_{Ic}) and bulge ductility"**, International Journal of Fracture, Vol. 23, p. 71.
- **Beyon J.W., Kwun S.I., (2003): "Magnetic non-destructive evaluation of thermally degraded 2.25 Cr-1Mo steel"**, Materials Letters, Vol. 58, p. 94-98.
- **Bicego V., Di Persio F., Rantala H. (2003): "Small Punch Creep Test Method: Results from a Round Robin Carried out within EPERC TTF5"** EPERC technical report Nr. 2, European Commission, JRC, T.N. P.03.112
- **Bocquet P. et al. (2000): "Prediction of Pressure Vessel Integrity in Creep Hydrogen Service (PREDICH)"**, Final Report, BRITE/EURAM project N° BE-1835, European Commision.
- **Bridgman P.W., (1944):** Trans. ASM, Vol. 32, p. 553.

- **Bridgman P.W., (1952): "Studies in Large Plastic Flow and Fracture"**, McGraw-Hill, New York.

- **Brookfield D.J., Li W., Rodgers B., Mottershead J.E., Hellen T.K., Jarvis J., Lohr R., Howard-Hildige R., Carlton A., Whelan M., (1999): "Material Properties for Residual Life Assessment from Small Specimens using the Punch and Bulge Test"**, Final report, EU project 13663-1998-02 F1PCA ISP GB.

- **Brozzo P., Deluca B., Rendina R., (1972): "A new method for the prediction of formability in metal sheet"**, Proceedings of the Seventh Biennial Conference of IDDRG on Sheet Metal Forming and Formability.

- **Byun T.S., Lee E.H., Hunn J.D., Farrell K., Mansur L.K., (2001): "Characterization of plastic deformation in a disk bend test"**, J. of Nuclear Materials, Vol. 294, p. 256-266.

- **Cane B.J., (1981):** Proc. ICF5, Ed. Francois, Cannes – France, p. 1285-1292.

- **Cane B.J., (1982): "Remaining creep life estimation by strain assessment on plants"**, Int. J. Press. Ves. & Piping, Vol. 10, p. 11-30.

- **Chakrabarty (1970): "A theory of stretch forming over hemispherical punch head"**, Int. J. Mechanical Science, Vol. 12, p. 315-325

- **Chen L-C., Shewmon P., (1994): "Stress assisted hydrogen attack cracking in 2.25 Cr-1Mo steels at elevated temperature"**, 2nd Int. Conf. on "Interaction of Steels with Hydrogen in Petroleum Industry Pressure Vessel Service" – 19-21 October, Vienna

- **Cheon J.S., Kim I.S., (1996): "Initial Deformation During Small Punch Testing",** Journal of Testing and Evaluation, Vol 24, N. 4, p. 255-262.

- **Cheon J.S., Kim I.S., (2000): "Evolution of thermal aging embrittlement in CF8 duplex stainless steel by small punch test",** Journal of Nuclear Materials, Vol. 278, p. 96-103.

- **Coble R.L., (1963):** J.Appl. Phys., Vol. 34 (6), p.1679 – 1682.

- **Cocke B.J., Buscemi C.D., Moore D.E., Klein L.J., Erwin W.E., (1993): "Hydrogen attack of Cr-Mo reactor steels",** Ed. Martin Prager, Material Properties Council, "Interaction of Steels with Hydrogen in Petroleum Industry Pressure Vessel Service"

- **Davidenkov N.N., Spiridonova N.I., (1946):** Proc. ASTM, Vol. 46, p. 1147)

- **Di Persio F., Stratford G., Hurst R.C. (2004) "Small Punch test for assessing H2 induced damage in steel for pressurized equipment",** Proc. of "High Temperature Plant Integrity & Life Extension" Conference, Cambridge 14-16 April 2004

- **Dobes F., Milicka K., (2001): "Small Punch Testing in Creep Conditions",** Journal of Testing and Evaluation, Vol. 29, No. 1, p. 31-35.

- **Dooley M., Lucas G.E., Sheckherd J.W., (1981):** Journal Nuclear Materials, Vol. 103-104, p. 1533-1536.

- **Dorn J.E.,Orr R.L., Sherby O.D., (1954):** Trans. ASME, 46, 1954, page 113

- **Eck S.J., Ardell A.J., (1998): "Fracture toughness of Ti-46 5Al-2 1Cr-3 0Nb-0 2W from finite element analysis of miniaturised disk-bend test results"**, Intermetallics, Vol. 6, 471-477.
- **Feltham P., Meakin J.D., (1959):** Acta Metall., (7), page 614.
- **Giannakopoulos A.E., Suresh S., (1999): "Determination of elastoplastic properties by instrumented sharp indentation"**, Scripta Materialia, Vol. 40, No. 10, p. 1191-1198.
- **Gibeling J.C., (2000): "Creep Deformation of Metals, Polymers, Ceramics, and Composites"**, Creep and Stress-Relaxation Testing, Chairman: Earthman J.C., Vol. 8 Mechanical Testing and Evaluation, ASM Handbook, Materials Park, OH, pp. 361 – 423.
- **Gotoh M., (1977):** Int. J. Mech. Sci., vol. 19, p. 505.
- **Greenwood G., (1973):** Proc 3rd Int. Conf. Strenght of Metals and Alloys, Cambrdige, 2, p. 91, London (Metals Soc.)
- **Hayhurst D.R., Trampczynski W.A., Leckie F.A., (1983):** Acta Metall., 31 (10), p.1537 – 1542.
- **Herbert (1910):** Mitt. U Forschungbarg, Ver. Deut. Ing., Vol. 89
- **Herring C., (1950):** J.Appl. Phys., Vol. 21, p.437 – 445.
- **Heung N.H., Keun-Hwan K., (2003): "A Ductile Fracture Criteria in Sheet Metal Forming Process"**, J. of Materials Processing Technology, Vol. 142, p. 231-238.
- **Hill R., (1948):** Proc. R. Soc. London A193, p. 281.

- **Hill R., (1950): "The mathematical theory of plasticity"**, Oxford University Press, London
- **Hill R., (1979): "Theoretical Plasticity of Textural Aggregate"**, Proc. Cambridge Phil. Soc., 85, 179.
- **Hoffmann M, Birringer R., (1995): "Quantitative Measurements of Young's Modulus Using the Miniaturized Disc-Bend Tests"**, Material Science and Engineering, A 202, p. 18 – 25.
- **Huangh F.H., Hamilton M.L. and Wire G.L., (1982):** Nuclear Technology, Vol. 57, p. 234-242.
- **Jia X., Dai Y., (2003): "Small punch tests on maretensitic/ferritic steels F82H, T91, and Optimax-A irradiated in SINQ Target-3"**, Journal of Nuclear Materials, Vol. 323, p. 360-367.
- **Johnson A.E., Henderson J., Khan B., (1962):** H.M.S.O. Edinburgh.
- **Komazay S., Hashida T., Shoij T., Suzuki K., (2000): "Development of Small Punch Tests for Creep Property Measurement of Tungsten-Alloyed 9 % CR Ferritic Steels"**, J. of Testing and Evaluation, Vol. 28, N. 4, p. 249 – 256.
- **Landau M.V., (1997): "Deep hydrotreating of middle distillates from crude and shale oils"**, Catalysis today, Vol. 36, p. 393-429.
- **Lin S.B., Ding J.L., (1995): "Experimental Study of the Plastic Yielding of Rolled Sheet Metals with the Cruciform Plate Specimen"**, Int. J. of Plasticity, Vol. 11, No. 5, p. 583 – 604.
- **Logan R.W., Hosford W.F., (1980):** Int. J. Mech. Sci., vol. 22, p. 419.

- **Lucas G.E., Odette R., Panchanadeeswaran R., Scheckerd J.W., (1984): "Shear Punch test for Mechanical Property Measurement in TEM Disc Sized Specimen"**, J. of Nuclear Materials, Vol. 122, p. 429-434.
- **Lundin C., Khan K., Liu P., (1994): "Study of hydrogen attack susceptibility of 2¼Cr-1Mo steel"**, 2nd Int. Conf. on "Interaction of Steels with Hydrogen in Petroleum Industry Pressure Vessel Service" – 19-21 October, Vienna
- **Maile K. et al. (1998): "COPERNICUS – SP Test Method Assessment for the Determination of the Residual Creep Life of Service Exposed Component"**, Final report, EU project ERB CIPA CT94 0103.
- **Manaham M.P., Argon A.S., Harling O.K, (1981): "The Development of a Miniaturized Disc Bend Test for the Determination of Postirradiation Mechanical Property"** Journal Nuclear Materials, 103 & 104, North Holland Publishing Company, p.1545-1550.
- **Manaham M.P., Browning A.E., Argon A.S., Harling O.K, (1986): "Miniaturized Disc Bend Test Technique Development and Application"**, ASTM STP 888, ASTM Philadelphia. PA, p. 17-49.
- **Manna G., (2004): "Factors limiting the in-service lifetime of CrMoV steels and weldments for pressure equipment"**, PhD thesis, University of Wales Swansea
- **Mao X., Takahashi H., (1987): "Development of a Further-Miniaturized Specimen of 3 mm Diameter for TEM Disc (∅ 3 mm) Small Punch Tests"** Journal of Nuclear Material, Vol. 150, North Holland, Amsterdam, p. 42-52.
- **Mc-Lean D., (1966):** Report Progress Phys, 29, page 1.

- **Monkman F.C., Grant N.J., (1956):** Proc. ASTM, (56), page 593.
- **Nabarro F.R.N., (1948):** Report on a Conference on the strength of Metals, Phys. Soc. London.
- **Okada A., Lucas G.E., Kiritani M., (1988):** Trans. Jpn. Inst. Met., Vol. 29 (2), p. 99-108.
- **Okomura H. et al., (1999): "Basic investigation for life assessment technology of modified 9Cr-1Mo steel",** Nuclear Engineering and Design, Vol. 193, p. 243-254.
- **Orowan E., (1946): "Creep in Metals",** J. West Scotland Iron and Steel Inst., Vol. 54, p. 45-53.
- **Parker J. D., Stratford G.C., Shaw N., Metcalfe H., (1998): "The Application of Miniature Disc Testing for the Assessment of Creep Damage in CrMoV Rotor Steel",** Conference Proceedings, BALTICA IV, Plant Maintenance for Managing Life & Performance, Vol. 2, p. 477 – 488.
- **Parker J. D., Stratford G.C., Shaw N., Spik G., Tate E., (1995): "Deformation and Fracture Processes in Miniature Disc Tests of CrMoV Rotor Steel",** Third International Charles Parsons Turbine Conference, Materials Engineering in Turbines and Compressors, Vol. 2, p. 419 – 428.
- **Prager M. (1992): "Hydrogen susceptibility of chrome-moly steels and weldments",** ASME Pressure Vessel and Piping Conference, New Orleans, USA.

- **Schlögl S.M., Giessen van der E. (1999) "Micromechanics of high temperature hydroegn attack"**, Proceedings of European Conference on Computational Mechanics, ed. By W.Wunderlich, Mubchen, 11 pages.

- **Sherby O.D., Burke P.M., (1967):** Prog. Mater. Sci., (13), page 325.

- **Singh R., Singh S.R., (1997): "Remaining creep life study of Cr-Mo-V main steam pipe lines"**, Int. J. Pes. Ves. & Piping, Vol. 73, p. 89-95.

- **Stelson K.A., Grossard, D.C. (1981): "An Adaptive Pressbrake Control Using an Elastic-Plastic Material"** Proceedings of the Joint Automatic Control Conference, Vol. 11, June 1981, Charlottesville, VA.

- **Tettamenti S., Crudeli R. (1998): "Small Punch Creep Test: a Promising methodology for High Temperature Plant Components Life Evaluation"** – Proc. of Baltica IV Conf: Plant Maintenance for Managing Life & Performance. Vol. 2, p. 501-509.

- **Timoshenko S. (1957): "Strength of Material"**, Mc-Graw-Hill, p. 104

- **Toshihiko K, Satoshi I., Kensuke K., (1998): "Measurement and analysis of differential work hardening in cold-rolled steel sheet under biaxial tension"**, Journal of Material Processing Technology, Vol. 80-81, p. 517-523.

- **Walle van E. et al., (2001) : "Reconstitution techniques qualification and evaluation to study ageing phenomena of nuclear pressure vessel materials (RESQUE)"**, Nuclear Engineering and Design, Vol. 209, p. 67-77.

- **Weertman J., (1957):** J.Appl. Phys., Vol. 28, p.362 – 364.

- **Yang Z., Wang Z., (2003): "Relationship Between Strain and Central Deflection in Small Punch Creep Specimens"**, Int. J. of Pressure Vessels and Piping, Vol. 80, p. 397 – 404.

12. Appendix

Procedure followed for determining stress in the SP creep test:

- Once the proper set of temperature and load has been chosen for the SP interrupted test a certain range of interruptions at differentfraction of creep life is performed.
- The geometrical features of all these SP interrupted tests are measured: minimum thickness t_ϕ and the angle ϕ pointing out at this region, the contact angle ϕ_c.
- Special attention should be dedicated at finding out the correct position of the critical area, say the portion of material where at the SP sample is failing. For this purpose the evolution of the "cup volume" along the creep test should be assessed.
- From the measurements and the model presented in this thesis, the evolution of stress in the critical area can be defined and evaluated in terms of load/stress ratio.
- The arithmetic average of the load/stress ratio is employed simply in order to find a unique value to be used for converting the load of the SP tests.
- This unique value should be used for a particular material and for the defined set of temperature and load.
- The stress rupture data can then be calculated from the load of the SP rupture tests using this average ratio.
- Combining data from different set of load and temperature could then be used for remanent life estimation.